# PERFORMANCE CHARACERISITICS OF ANNULAR LINEAR AND PERMANENT MAGNET INDUCTION PUMPS OF FINITE DIMENSIONS

By

#### Jordan D. Rein

A dissertation submitted in partial fulfillment of the requirements for the degree of

Doctor of Philosophy

(Nuclear Engineering and Engineering Physics)

at the

UNIVERSITY OF WISCONSIN-MADISON

2020

Date of final oral examination: 08/31/2020

The dissertation is approved by the following members of the Final Oral Committee:
Mark Harland Anderson, Professor, Engineering Physics
Ricardo Bonazza, Professor, Engineering Physics
Gregory Nellis, Professor, Mechanical Engineering
David Rothamer, Professor, Mechanical Engineering
Oliver Schmitz, Professor, Engineering Physics

#### EXECUTIVE SUMMARY

Liquid metals have gained renewed interest as an efficient energy carrier for applications ranging in concentrated solar, nuclear fission, and other industrial processes. Specifically, the nuclear sector is significantly interested in using elemental sodium metal as a reactor coolant. Liquid sodium has several advantages over water in nuclear applications including a high thermal conductivity and boiling point. While the advantages are significant, a common need for all sectors is the development of improved thermal hydraulic components like pumps, flowmeters, heat exchangers, impurity monitoring and control, and more. One of the most critical is pumps. Typically, mechanical pumps have filled this role for liquid metal systems. However, there are challenges in their application to chemically reactive fluids like sodium. In this regard, liquid metals have another advantage; since the fluid is electrically conductive it can be pumped by magnetic fields with the Electromagnetic Induction Pump (EMIP).

EMIPs use traveling magnetic fields to generate a Lorentz Force in the liquid metal. These pumps have several advantages over mechanical pumps. For example, EMIPs are hermetically sealed, they have no rotating parts in direct contact with sodium, their components are mounted externally and avoid direct contact with liquid metal, they can operate in any orientation, and they have a lower resistance path for natural circulation. These advantages are particularly significant in the nuclear where safety is a driving factor. Since the 1950's, several EMIP subclasses have been successfully developed using polyphase electric currents such as the Flat Linear Induction Pump (FLIP) and Annular Linear Induction Pump (ALIP). Recently, a new subclass has been developed using rotating arrays of permanent magnets called the Permanent Magnet Induction Pump (PMIP). While EMIPs have significant advantages over mechanical pumps, there are challenges applying these pumps at the large scale. One of these challenges is the low EMIP efficiency which can range from 5% to 45%. While some of these inefficiencies are inherent to the pump type, such as resistive heating in the fluid and channel walls, others are caused by finite dimensional edge effects.

Literature has shown that the two primary edge effects are the Finite Length Effect and the Finite Width Effect. The Finite Length Effect is observed in FLIPs and ALIPs and is the result of three factors. Firstly, at high  $Rm_f \cdot s_m$  the magnetic flux is carried in the fluid direction. Consequently, the flux distribution becomes non-uniform along the pump length. Secondly, the finite length of the applied currents results in the formation of standing waves in the pump's active region. This results in a pulsation of the fields especially at high  $Rm_f \cdot s_m$ . Lastly, the finite length of the ferromagnetic core results in the formation of large negatively oscillating braking forces at the pump inlet and outlet. This is a consequence of a stepchange in the magnetic air-gap reluctance and increases with increasing  $Rm_f \cdot s_m$ . These three factors of the Finite Length Effect result in reduced pump performance relative to the ideal.

The Finite Width Effect is observed in FLIPs and PMIPs and is a direct result of current continuity which requires the induced currents to form continuous loops in the pump. However, the resulting loops will have a component which produces no useful pumping force. Consequently, the PMIP performance is reduced relative to the ideal. This effect is exacerbated as the width of the pump becomes small relative to the current loops. Additionally, another factor must be considered for PMIPs. Since PMIPs use finite-width permanent magnets, the flux distribution across the channel width is non-uniform. Therefore, the non-uniform flux will result in reduced pump performance relative to the ideal.

This work attempts to investigate finite dimensional edge effects through performance characterization of small-scale EMIPs. The Finite Length Effect was investigated through performance measurement of a small commercial ALIP. Pressure-flowrate and efficiency curves for a standard configuration ALIP were measured in 200 °C and 400 °C sodium and compared to theory. These measurements provided a baseline performance which was used to compare modified ALIP configurations. Then, pressure-flowrate and efficiency curves for a modified ALIP were measured in 200 °C. These modifications included shifting the

coils and outer-core to two locations as well as two coil grading configurations. Additionally, several other ALIP parameters were measured. Firstly, the magnetic field was characterized for a standard and four modified configurations. Secondly, pump channel frictional losses were characterized as a function of flowrate. Lastly, the dry-pump input power was characterized as a function of input current. In total, this work concluded that the coil shifting and coil grading configurations had little impact on pump performance due to the relatively high pump frequency.

The Finite Width Effect was investigated through performance measurement of a small custom designed PMIP. Pressure-flowrate and efficiency curves were measured in 200 °C and 400 °C sodium and compared to theory. These experimental performance measurements were used to validate a theoretical correction factor which accounts for the finite magnet width. Additionally, several other PMIP parameters were measured. Firstly, the magnetic field was characterized across the channel width at several heights. Secondly, pump channel frictional losses were characterized in 200 °C and 400 °C sodium as a function of flowrate. Lastly, dry-pump input power was characterized as a function of magnet frequency. In total, this work produced pressure-flowrate and efficiencies curves for a PMIP, validated the finite magnetic with correction factor, and concluded that the finite channel and magnet width have a profound impact on the total PMIP performance.

#### **ACKNOWLEDGMENTS**

Financial support for this project was provided by the United States Department of Energy via the Nuclear Energy University Program (NEUP).

I would like to thank my advisor Professor Mark Anderson. Without his expertise and support, this work would not have been possible. Paul Brooks was invaluable to this project and for my development from an undergraduate hourly worker to a PhD candidate. It is impossible to express my gratitude for his patience under the constant barrage of questions, emails, phone calls, and out-of-position welding which made this project possible. Bryan Coddington also contributed significantly to my development through his mentorship. His technical mastery of welding were crucial in completing this work. Seth Jones was critical in this project with his superb skills as a machinist. Additionally, I would like to thank Dr. Mike Hvasta and Professor William Nollet blazing the trail of sodium work at the THL as well as their guidance and wisdom throughout the duration of my time at UW-Madison. Thank you also to Professor Bonazza, Nellis, Rothamer, and Schmitz for their participation on my thesis committee and advisement.

I am grateful for the support of many friends and colleagues through the duration of this work. I would like to thank James for his constant support, friendship, and willingness to share an office for three years; Emily for her willingness to listen and support me; Kate for her camaraderie and help with the many classes we shared; Karl for his friendship, endless wisdom, and terrible jokes; Shaun for his expertise in engineering and Midwestern attitude; and Matt for his technical assistance, support, and friendship.

Finally, I would like to thank my parents, Don and Linda, for providing me the environment, tools, and support needed to finish this work.

## **TABLE OF CONTENTS**

1. IN	TRODUCTION	1
1.1	MOTIVATION	7
1.2	OBJECTIVES	8
1.3	APPROACH	9
1.4	SUMMARY	10
2. TH	IEORETICAL BACKGROUND	13
2.1	ELECTROMAGNETIC INDUCTION PUMPING	13
2.1	.1 Principle of Operation	13
2.1	.2 Analytical Solution of an Ideal EMIP	13
2.2	THE ANNULAR LINEAR INDUCTION PUMP	25
2.2	2.1 Fundamental Components	25
2.2	2.2 Analytical Solution of a Finite Length Pump	25
2.2	2.3 Effects of the Finite Length	28
2.2	2.4 Summary	33
2.3	THE PERMANENT MAGNET INDUCTION PUMP	35
2.3	3.1 Fundamental Components	35
2.3	3.2 Analytical Solution of a Finite Width Pump	35
2.3	3.3 Effects of the Finite Width	44
2.3	3.4 Summary	48
	LIP PERFORMANCE CHARACTERISTICS AND THE IMPACT OF THE I	
3.1	ALIP SPECIFICATIONS	49
3.2	EXPERIMENTAL SETUP	52
3.2	2.1 Facility Overview	52
3.2	2.2 Magnetic Field Measurement	52
3.2	2.3 Flowrate Measurement	55
3.2	2.4 Pressure Measurement	61
3.2	2.5 Power Measurement	62
3.3	EXPERIMENTAL MEASUREMENTS	64
3.3	3.1 Axial Magnetic Field Distribution	64
3.3	3.2 Frictional Pressure Losses	69
3.3	3.3 Resistive Heating Losses	73
3.3	3.4 Standard Configuration Pressure-Flowrate and Efficiency Performance	74
3.3	3.5 Coil Shifting Pressure-Flowrate and Efficiency Performance	76
3.3	3.6 Coil Grading Pressure-Flowrate and Efficiency Performance	80
3.4	EFFECT OF THE FINITE LENGTH	84

3.4.1 Unmodified Pump Results	85
3.4.2 Coil Shifting Results	90
3.4.3 Coil Grading Results	92
3.5 CONCLUSIONS AND FUTURE WORK	95
4. PMIP PERFORMANCE CHARACTERTISTCS AND THE IMPACT OF THE FINI	
EDGE EFFECT	
4.1 PMIP SPECIFICATIONS	
4.2 EXPERIMENTAL SETUP	99
4.2.1 Facility Overview	99
4.2.2 Flowrate Measurement	99
4.2.3 Pressure Measurement	103
4.2.4 Power Measurement	104
4.3 EXPERIMENTAL MEASUREMENTS	105
4.3.1 Radial Magnetic Field Distribution	105
4.3.2 Frictional Pressure Losses	107
4.3.3 Resistive Heating Losses	109
4.3.4 Pressure-Flowrate	111
4.3.5 Efficiency	112
4.4 EFFECT OF THE FINITE WIDTH	113
4.5 CONCLUSIONS AND FUTURE WORK	119
5. SUMMARY OF CONCLUSIONS AND RECCOMENDED FUTURE WORK	121
5.1 SUMMARY OF ALIP CONCLUSIONS AND FUTUE WORK	121
5.2 SUMMARY OF PMIP CONCLUSIONS AND FUTURE WORK	123
5.3 SIGNIFICANCE AND CONCLUDING REMARKS	124
6. REFERENCES	128

## LIST OF FIGURES

Figure 1-1: Diagram of the failed shaft seal-bearing system of the SRE centrifugal pumps [6] [8]	4
Figure 1-2: SRE fuel element damage resulting from the failed pump shaft seal-bearing system. On the top is a photo of an undamaged fuel element. On the bottom left is a portion near the bottom of the fuel assembly while on the bottom right is a portion near the middle of the fuel assembly [8]	4
Figure 1-4: Photo of a General Electric Flat Linear Induction Pump (FLIP) similar to the model used in the USS Seawolf's sodium cooled reactor [12]	5
Figure 2-1: Simplified geometry for an idea EMIP.	7
Figure 2-2: Normalized pressure output of an ideal EMIP as a function of Rmf · sm. Note that as Rmf · sm passes unity, the developed pressure decreases which is a common observation in EMIPs [32] [34] [35]	2
Figure 2-3: Ideal EMIP efficiency plotted with the analytically calculated ALIP efficiency as a function of mean-slip.	4
Figure 2-4: On the left is a cross-section of the pump. A cut-away of a practical ALIP [9]2	5
Figure 2-5: Simplified geometry for a finite length, infinite width, EMIP [32]2	6
Figure 2-6: Numerical model of the force density along the length of an ALIP. In this model, large negative force pulsations developed at the entrance and exit of the pump, with the exit braking force have a larger magnitude than the entrance braking force [20]	9
Figure 2-7: Numerical model of the time averaged force density along the length of an ALIP. This model also predicts large negative braking forces at the inlet and exit of the pump [35]	9
Figure 2-8: Numerical model of pressure pulsations in a finite length ALIP. These pressure pulsations were found to occur at twice the supply frequency of the pump [38]	0
Figure 2-9: Numerical and experimental comparison of DSF pulsation magnitude as a function of slip [20]	0
Figure 2-10: Experimental measurements of DSF pulsations in a finite length ALIP [22]3	1
Figure 2-11: Experimental measurement of DSF pulsation magnitude as a function of slip and supply frequency [22]	1
Figure 2-12: The reduction in DSF pulsation magnitude as a function of coil grading at three pump frequencies [22].	3
Figure 2-13: The reduction of electrical input power and resulting increase of efficiency as a function of coil grading [22]	3
Figure 2-14: Disc-Type (left) and Drum-Type (right) PMIP configurations where alternating polarity magnets are denoted as blue or red. The Disc-Type configuration can also have an additional magnetarray on bottom with the flow channel located in the middle	5
Figure 2-15: Simplified geometry in the solution of the Induction Equation for a PMIP. Note that the flow channel and both upper and lower channel walls are assumed to be electrically insulated from each other. Also note that no channel sidewalls exist.	6
Figure 2-16: Normalized attenuation coefficient Kat, 1 at $Rmf \cdot sm = 0$ as a function of normalized pump half-width b. As b approaches infinity, Kat, 1 approaches unity and the pressure output approaches the ideal EMIP pressure output.	9

Figure 2-17: Near unity values of the normalized attenuation coefficient Kat, 1 at $Rmf \cdot sm = 0$ as a function of the pump half-width b. For laboratory-scale, or medium-scale PMIPs, these pump half-widths are impractical
Figure 2-18: Normalized attenuation coefficient Kat, 2 at Rmf $\cdot$ sm = 0 as a function of normalized shape-factor $\Gamma$ for a fixed pump half-width b. As $\Gamma$ approaches zero, Kat, 2 will approach Kat, 1 evaluated at the given half-width b
Figure 2-19: Ideal EMIP efficiency plotted with the analytically calculated PMIP efficiency as a function of mean-slip. Note that when evaluating Kat, 2 a magnetic field shape-factor value of $\Gamma=\pi 2$ was used
Figure 2-20: Qualitative distribution of currents in a finite width duct with no electrically conducting walls
Figure 2-21: Qualitative distribution of currents in a finite width duct with electrically conducting walls.
Figure 2-22: Qualitative current distribution in a rectangular under the influence of a stationary and uniform magnetic field [44]. On the left is the case where the side walls have a finite conductivity. On the right is the case where the side walls have zero conductivity
Figure 2-23: Geometry used in a FLIP numerical model. While the results do not directly represent a PMIP, the channel geometry is similar and the results do provide insight into the finite width effects of a PMIP [45]
Figure 2-24: Geometry used in a FLIP numerical model. While the results do not directly represent a PMIP, the channel geometry is similar and the results do provide insight into the finite width effects of a PMIP [45]
Figure 2-25: Experimental setup of a Drum-Type PMIP used to pump GaInSn. Four configurations were used to study the impact of outer ferrous yokes and copper side bars [46]
Figure 2-26: Experimental pressure output of the Drum-Type PMIP with, 1 no ferromagnetic yoke or copper side bars, 2 with a ferromagnetic yoke and no copper side bars, 3 no ferromagnetic yoke and with copper side bars, and 4 with a ferromagnetic yoke and copper side bars [46]
Figure 3-1: Custom designed and built CMI-Novacast model LA125 ALIP used in experimental testing.
Figure 3-2: Qualitative sketch of coil shifting configurations of the experimental ALIP50
Figure 3-3: Sketch of the tapped coils installed in the first three and last three coil locations. Each of the six coils have taps at the 1 <sup>st</sup> , 20 <sup>th</sup> , 31 <sup>st</sup> , or 80 <sup>th</sup> turn
Figure 3-4: Cut away of the experimental ALIP showing each of the 12 polyphase coils in the pump. Note that the first three coils and last three coils are tapped
Figure 3-5: Schematic of the ALIP Test Facility used in the characterization of the finite length effect on an Annular Linear Induction Pump
Figure 3-6: Air-cored pick-up coil used to measure the radial magnetic field distribution in the ALIP channel
Figure 3-7: Calibration curve for the pick-up coil in Figure 3-6 used to measure the radial magnetic field component in the ALIP channel.
Figure 3-8: Pick-up coil calibration residuals. For simplicity, the measurement error was taken as 5% the measured value. Note that the calibration can be improved with more data points which would allow for a more sophisticated error analysis.

Figure 3-9: Photo of the ALIP-EMFM used for primary flowrate measurements
Figure 3-10: Normalized signal difference between the reference vortex shedding flowmeter and ALIP-EMFM over a period of 20 hours. Note that the initial wetting occurred over the first two hours
Figure 3-11: Calibration curve of the EMFM to the Vortex Shedding flowmeter.
Figure 3-12: Standard Uncertainty calculated following the Guide to the Expression of Uncertainty in Measurement standard compared to the calculated calibration residuals. As a conservative estimate, the accuracy of the ALIP-EMFM is broken into two ranges; in the range of $1\text{m}3\text{hr} \leq Q < 2.5\text{m}3\text{hr}$ the accuracy is reported as 1.5% the measured value while in the range of $2.5\text{m}3\text{hr} \leq Q < 9.5\text{m}3\text{hr}$ the accuracy is reported at 0.75% the measured value.
Figure 3-13: Location of differential pressure measurement for the channel frictional losses ploss, chan and developed pressure $\Delta p$ . Note that any height-induced pressures were recorded at several zero-flowrate conditions and subsequently offset from the final pressure measurements. Due to space constraints, ploss, chan was measured at a different location than $\Delta p$ .
Figure 3-14: Wiring diagram of the ALIP to the Power Meter. Note that the source is a 480 $V_{rms}$ , delta configuration source with a 'wild-leg' and no neutral was used when wiring the power meter
Figure 3-15: Configuration-100 axial distribution of the radial magnetic field component at $100~V_{rms}$ and $6~A_{rms}$ in a dry pump. The axial position 'z' is reference from the beginning of the inner stator at $z=0~mm$ . Note that the end of the stator is denoted by the solid black vertical line at $z=300~mm$ . Observe that the applied magnetic field is non-unifom and will produce peaks depending on the relative position of the pick-up coil and pump coils.
Figure 3-16: Comparison of Configuration-100 and Configuration-200 axial distribution of the radial magnetic field component at $100V_{rms}$ and $6A_{rms}$ in a dry pump. The axial position 'z' is reference from the beginning of the inner stator at $z=0$ mm. Note that the end of the stator is denoted by the solid black vertical line at $z=300$ mm. Also note that the dashed vertical lines denote the start and end of the outer stator.
Figure 3-17: Comparison of Configuration-100 and Configuration-300 axial distribution of the radial magnetic field component at $100~V_{rms}$ and $6~A_{rms}$ in a dry pump. The axial position 'z' is reference from the beginning of the inner stator at $z=0~mm$ . Note that the end of the stator is denoted by the solid black vertical line at $z=300~mm$ . Also note that the dashed vertical lines denote the start and end of the outer stator
Figure 3-18: Comparison of Configuration-100 and Configuration-101 axial distribution of the radial magnetic field component at $100~V_{rms}$ and $6~A_{rms}$ in a dry pump. The axial position 'z' is reference from the beginning of the inner stator at $z=0~mm$ . Note that the end of the stator is denoted by the solid black vertical line at $z=300~mm$ . Also note that the dashed vertical lines denote the start and end of the outer stator.
Figure 3-19: Comparison of Configuration-100 and Configuration-102 axial distribution of the radial magnetic field component at $100  V_{rms}$ and $6  A_{rms}$ in a dry pump. The axial position 'z' is reference from the beginning of the inner stator at $z=0$ mm. Note that the end of the stator is denoted by the solid black vertical line at $z=300$ mm. Also note that the dashed vertical lines denote the start and end of the outer stator.
Figure 3-20: Experimental ploss, chan data measured in water at 20 °C and 2 bar gauge pressure. Also plotted are the empirically calculated pressure losses in an annular channel using an effective ALIP channel length of 1.215 m. Note that the physical ALIP channel length is 0.44 m.
Figure 3-21: Residuals between the experimental ploss, chan data and the empirical correlation

Figure 3-22: Empirical friction factor fD evaluated using 200 °C and 400 °C sodium.	72
Figure 3-23: Empirically calculated ploss, chan in 200 °C and 400 °C sodium using an effective channel length of 1.415 m.	72
Figure 3-24: ALIP channel wall temperature as a function of current for a dry pump. Note that the temperature is a result of inductive heating and parasitic losses; no heaters or coolers were used to control the temperature.	73
Figure 3-25: Experimentally measured ALIP input power for a dry pump compared to the analytically calculated resistive heating losses in the channel walls. Note that the analytic theory neglects core losses, coil resistive heating losses, as well as others. These factors would therefore tend to increase the analytically calculated term.	74
Figure 3-26: ALIP pressure-flowrate data at sodium temperatures of 200 °C and 400 °C and applied voltages of $50V_{rms}$ , $75V_{rms}$ , $100V_{rms}$ , and $150V_{rms}$ . The pump pressures were measured in an envelope with the lower flowrate bound restricted by the EMFM calibration and the upper flowrate bound restricted by the system loss curves.	75
Figure 3-27: ALIP pressure-slip data at sodium temperature of 200 $^{\circ}$ C and 400 $^{\circ}$ C and applied voltages of 50 $V_{rms}$ , 75 $V_{rms}$ , 100 $V_{rms}$ , and 150 $V_{rms}$ . The pump pressures were measured in an envelope with the lower slip bound restricted by the system loss curves and the upper slip bound restricted by the EMFM calibration.	75
Figure 3-28: ALIP efficiency-slip data at sodium temperatures of 200 $^{\circ}$ C and 400 $^{\circ}$ C and RMS voltages of 50 $V_{rms}$ , 75 $V_{rms}$ , 100 $V_{rms}$ , and 150 $V_{rms}$ .	76
Figure 3-29: Qualitative sketch of coil shifting configurations of the experimental ALIP.	77
Figure 3-30: Comparison of Configuration-100 and Configuration-200 ALIP pressure-flowrate data at 200 $^{\circ}$ C. Note that these curves were obtained with fixed system losses and variable pump voltages between 20 $V_{rms}$ and 150 $V_{rms}$ .	78
Figure 3-31: Comparison of Configuration-100 and Configuration-200 ALIP efficiency-flowrate data at 200 $^{\circ}$ C. Note that these curves were obtained with fixed system losses and variable pump voltages between 20 $V_{rms}$ and 150 $V_{rms}$ .	78
Figure 3-32: Comparison of Configuration-100 and Configuration-300 ALIP pressure-flowrate data at 200 $^{\circ}$ C. Note that these curves were obtained with fixed system losses and variable pump voltages between 20 $V_{rms}$ and 150 $V_{rms}$ .	79
Figure 3-33: Comparison of Configuration-100 and Configuration-300 ALIP efficiency-flowrate data at 200 $^{\circ}$ C. Note that these curves were obtained with fixed system losses and variable pump voltages between 20 $V_{rms}$ and 150 $V_{rms}$ .	80
Figure 3-34: Comparison of Configuration-100 and Configuration-101 ALIP pressure-flowrate data at 200 $^{\circ}$ C. Note that these curves were obtained with fixed system losses and variable pump voltages between 20 $V_{rms}$ and 150 $V_{rms}$ .	81
Figure 3-35: Comparison of Configuration-100 and Configuration-101 ALIP efficiency-flowrate data at 200 $^{\circ}$ C. Note that these curves were obtained with fixed system losses and variable pump voltages between 20 $V_{rms}$ and 150 $V_{rms}$ .	82
Figure 3-36: Comparison of Configuration-100 and Configuration-102 ALIP pressure-flowrate data at 200 °C. Note that these curves were obtained with fixed system losses and variable pump voltages between 20 V <sub></sub> and 150 V <sub></sub>	83

Figure 3-37: Comparison of Configuration-100 and Configuration-102 ALIP efficiency-flowrate data at 200 $^{\circ}$ C. Note that these curves were obtained with fixed system losses and variable pump voltages between 20 $V_{rms}$ and 150 $V_{rms}$ .
Figure 3-38: Plot of maximum output pressure as a function of Rmf $\cdot$ sm at 200 °C at 50 $V_{rms}$ , 100 $V_{rms}$ , and 150 $V_{rms}$ . Note that changing the voltage changes the input current which therefore changes the magnitude field magnitude. Analytic theory shows that this will change the slope which is why three distinct curves appear versus a single curve.
Figure 3-39: Plot of maximum output pressure as a function of Rmf $\cdot$ sm at 400 °C and 50 $V_{rms}$ , 100 $V_{rms}$ , and 150 $V_{rms}$ under a fixed frequency of 120 Hz. Note that changing the voltage changes the input current which therefore changes the magnitude field magnitude. Analytic theory shows that this will change the slope which is why three distinct curves appear versus a single curve
Figure 3-40: Plot of pump efficiency as a function of Rmf $\cdot$ sm at 200 °C and 400 °C under pump voltages of 50 $V_{rms}$ and 150 $V_{rms}$ and a fixed frequency of 120 Hz.
Figure 3-41: Comparison of Configuration-100, Configuration-200, and Configuration-300 differential pressure output as a function of flowrate over the applied voltages of $20~V_{rms}$ and $150~V_{rms}$ and under a frequency of $120~Hz$ .
Figure 3-42: Comparisons of Configuration-100, Configuration-200, and Configuration-300 efficiency as a function of flowrate over the applied voltages of 20 $V_{rms}$ and 150 $V_{rms}$ and under a frequency of 120 Hz.
Figure 3-43: Comparison of Configuration-100, Configuration-101, and Configuration-102 differential pressure output as a function of flowrate over the applied voltages of $20~V_{rms}$ and $150~V_{rms}$ and under a frequency of $120~Hz$
Figure 3-44: Comparison of Configurations-100, Configuration-101, and Configuration-102 efficiency as a function of flowrate over the applied voltages of $20~V_{rms}$ and $150~V_{rms}$ and under a frequency of $120~Hz$ .
Figure 4-1: An example of the 12-Pole Double-Array Disc-Type PMIP studied in this work
Figure 4-2: UW-Madison sodium test facility used for experimental PMIP measurements99
Figure 4-3: Photo of the PMIP-EMFM used for primary flowrate measurements
Figure 4-4: Calibration curve of the PMIP-EMFM to the Vortex Shedding flowmeter
Figure 4-5: Standard Uncertainty calculated following the Guide to the Expression of Uncertainty in Measurement standard compared to the calculated calibration residuals. As a conservative estimate, the flowmeter error is taken as 2% the measured flowrate over the range $0.9m3hr \le Q < 2m3hr$ and $0.75\%$ the measured flowrate over the range $2m3hr \le Q \le 7m3hr$
Figure 4-6: Location of differential pressure measurement for the channel frictional losses $\Delta$ ploss, chan and developed pressure $\Delta$ p and system loss ploss, sys testing. Note that any height-induced pressures were recorded at several zero-flowrate conditions and subsequently offset from the final pressure measurements. Due to space constraints, $\Delta$ ploss, chan was measured at a different location than $\Delta$ p and $\Delta$ ploss, sys.
Figure 4-7: Sketch of the experimental PMIP with the installed torque sensor
Figure 4-8: Experimental measurements of the applied magnetic field peak amplitude Be, yx as a function of pump width at several heights yi. Note that the x-coordinate is centered on the pump channel with negative values directed towards the magnet array's axis of rotation. The dashed vertical lines represent the pump width. Also plotted is Equation 4-3 using the values presented in Table 4-6

Figure 4-9: PMIP channel pressure loss measurements as a function of mass flowrate at 200 °C and 400 °C. A single curve was fitted using the model in Equation 4-4 with the resulting coefficients and standard errors presented in Table 4-7
Figure 4-10: Frictional pressure losses in the PMIP test system as a function of mass flowrate at 200 °C and 400 °C
Figure 4-11: PMIP wall temperature as a function of magnetic frequency for the dry pump resistive heating loss measurements. Note the temperature was a result from inductive heating and parasitic losses; no heaters or coolers were used to control the temperature
Figure 4-12: Experimentally measured PMIP input power compared to the analytically calculated resistive heating losses in the channel walls. Note that the analytic theory neglects the channel sidewalls, frictional losses in the bearings, windage losses from the rotating magnet arrays, pullies, and belt, as well as other losses. These factors would therefore tend to increase the analytically calculated term
Figure 4-13: PMIP pressure-flowrate data at sodium temperatures of 200 °C and 400 °C and magnet frequencies of 30 Hz, 60 Hz, 75 Hz and 90 Hz. The pump pressures were measured in an envelope with the lower flowrate bound restricted by the PMIP-EMFM calibration and the upper flowrate bound restricted by the system loss curves.
Figure 4-14: PMIP pressure-slip data at sodium temperature of 200 °C and 400 °C and magnet frequencies of 30 Hz, 60 Hz, 75 Hz and 90 Hz. The pump pressures were measured in an envelope with the lower slip bound restricted by the system loss curves and the upper slip bound restricted by the EMFM calibration
Figure 4-15: PMIP efficiency-slip data at sodium temperatures of 200 °C and 400 °C under magnetic field frequencies of 30 Hz, 60 Hz, 75 Hz, and 90 Hz. Note that the data plotted as mean-slips less than 0.7 are the system loss curves.
Figure 4-16: Plot of the maximum output pressure as a function of Rmf·sm at 200 °C under constant fluid flowrates of 1 m³/hr and 3.2 m³/hr
Figure 4-17: Plot of the maximum output pressure as a function of Rmf·sm at 400 °C under constant fluid flowrates of 1 m³/hr and 3.2 m³/hr
Figure 4-18: Plot of pump efficiency as a function of Rmf·sm at 200 °C under constant frequency conditions. Note that the theoretical efficiencies are calculated using only using the Kat, 1
Figure 4-19: Plot of pump efficiency as a function of Rmf·sm at 400 °C under constant frequency conditions. Note that the theoretical efficiencies are calculated using only using the Kat, 1

## LIST OF TABLES

Table 1-1: Nominal operating conditions of the Enrico Fermi-I Sodium Cooled Reactor and the Shippingport Pressurized Water Reactor. Note that the sodium fluid properties were evaluated using Fink [2]	2
Table 3-1: Rated conditions for CMI-Novacast's LA125 ALIP.	49
Table 3-2: Some relevant geometric properties for CMI-Novacast's LA125 ALIP	50
Table 3-3: Summary of the setup of each configuration studied in this work.	51
Table 3-4: Relevant dimensions of the air-cored pick-up coil in Figure 3-6.	53
Table 3-5: Pick-up coil correlation coefficients, their standard errors, and correlation coefficient	55
Table 3-6: Additional specifications of the ALIP- EMFM.	56
Table 3-7: Reported accuracy of the Vortex Shedding Flowmeter. Flowrates were calculated in a 2.66 cm diameter conduit with sodium properties evaluated using Fink [2]at 200 °C	58
Table 3-8: ALIP-EMFM coefficients, their associated standard errors, and correlation coefficient	59
Table 3-9: Estimated uncertaintities of the primary ALIP-EMFM measurements	60
Table 3-10: Tap locations for each coil on the coil grading configuration tests.	68
Table 3-11: Tap locations for the coil grading configurations	80
Table 4-1: Relevant PMIP configuration data.	98
Table 4-2: Relevant PMIP magnet data	99
Table 4-3: Additional specifications of the PMIP-EMFM used to measure volumetric flowrates in this work.	00
Table 4-4: PMIP-EMFM correlation coefficients, their associated standard errors, and the correlation coefficient.	01
Table 4-5: Estimated uncertaintities of the primary EMFM measurements	02
Table 4-6: Coefficients for the PMIP's applied magnetic field profile across the channel width1	07
Table 4-7: PMIP channel and system pressure loss coefficients, their standard errors, and the correlation coefficient.	09

#### NOMENCLATURE

Acronym	
AIM	 Asynchronous Induction Motor
ALIP	 Annular Linear Induction Pump
AWG	 American Wire Gauge
DSF	 Double Supply Frequency

EM ... Electromagnetic

EMFM ... Electromagnetic Flowmeter
EMIP ... Electromagnetic Induction Pump

FFT ... Fast Fourier Transform
FLIP ... Flat Linear Induction Pump
MHD ... Magnetohydrodynamics
MMP ... Moving Magnet Pump

PMIP ... Permanent Magnet Induction Pump

RMS ... Root-Mean-Square S.E. Standard Error SmCo ... Samarium-Cobalt

#### **Symbols**

A	 Magnetic	vector	notential	in	T-m
1 <b>1</b>	 magnetic	100101	potential	111	1 111

A ... Non-dimensional magnetic vector potential

À ... Complex magnitude of magnetic vector potential in T-m

A<sub>0</sub> ... ALIP-EMFM calibration intercept in m<sup>3</sup>/hr

 $A_1$  ... ALIP-EMFM calibration slope  $A_{eff}$  ... Effective pick-up coil area in  $m^2$ 

a ... Effective channel height  $a = 2 \cdot h_w + h_{ch}$  in m

B ... Total EMIP magnetic field vector in T

**B**<sub>e</sub> ... Externally applied magnetic field vector in T

**B**<sub>i</sub> ... Induced magnetic field vector in T

B ... Complex magnitude of the total EMIP magnetic field in T

B<sub>0</sub> ... Peak magnetic field amplitude in T

B<sub>pk</sub> ... Amplitude of magnetic field detected by pick-up coil in T

 $\begin{array}{cccc} B_r & & \dots & & \text{Residual magnetism in T} \\ 2 \cdot b & & \dots & & \text{Channel width in m} \end{array}$ 

C ...  $p_{EM}$  coefficient  $C = \frac{1}{2}\sigma_f L_e$  in 1/ohm

 $\begin{array}{cccc} C_0 & & \dots & \text{Pick-up coil calibration intercept coefficient in } mV\text{-s/m}^2 \\ C_1 & & \dots & \text{Pick-up coil calibration slope coefficient in } mV\text{-s/kG-m}^2 \end{array}$ 

 $c_p$  ... Fluid specific heat capacity in J/g- $^{\circ}C$ 

 $D \hspace{1cm} \text{rm}_f \cdot s_m \hspace{0.1cm} \text{coefficient} \hspace{0.1cm} D = \frac{\mu_f \sigma_f}{k_0} \frac{h_{ch}}{h_{gap}} \hspace{0.1cm} \text{in s/m}$ 

 $\begin{array}{cccc} D_0 & & \dots & & PMIP \ pressure \ loss \ calibration \ intercept \ in \ bar \\ D_1 & & \dots & PMIP \ pressure \ loss \ calibration \ slope \ in \ bar-s^2/kg^2 \end{array}$ 

D<sub>o</sub> ... Outer diameter of EMFM channel in m

 $\begin{array}{cccc} D_H & & \dots & & Hydraulic diameter in m \\ dV & & \dots & Differential volume in m^3 \end{array}$ 

d<sub>i</sub> ... Inner diameter of EMFM channel in m

Total EMIP electric field in V/m

 $\mathbf{F}_{\mathbf{V}}$  ... Volumetric Lorentz Force density in N/m<sup>3</sup>

f<sub>B</sub> ... Magnetic field frequency in Hz

 $\begin{array}{lll} f_D & & \dots & & Darcy \ Friction \ Factor \\ f_{PMIP} & & \dots & PMIP \ disc \ frequency \ in \ Hz \\ h_{ch} & & \dots & Channel \ height \ in \ m \end{array}$ 

 $h_g \hspace{1.5cm} ... \hspace{1.5cm} Non\text{-magnetic gap height in m} \\$ 

 $\begin{array}{cccc} h_w & & \dots & & Wall \ thickness \ in \ m \\ \iota & & \dots & & Imaginary \ unit \ \sqrt{-1} \\ J & & \dots & & Current \ density \ in \ A/m^2 \end{array}$ 

 $\mathbf{J}_{f,c}$  ... Induced current density vector in the fluid or channel-walls in A/m<sup>3</sup>

 $\begin{array}{cccc} \textbf{j} & \dots & \text{Total EMIP current density in A/m}^3 \\ \textbf{J}_0 & \dots & \text{Effective current sheet magnitude in A/m}^2 \\ \end{array}$ 

K ... Pressure loss coefficient

 $K_1$  ... EMFM wall-shunting correction factor  $K_2$  ... EMFM end-shunting correction factor  $K_3$  ... EMFM magnetic-temperature factor  $K_{at,(1,2)}$  ... PMIP finite width attenuation coefficients

k ... Wave number

k<sub>0</sub> ... Fundamental wave number

 $\begin{array}{cccc} L & & \dots & & \text{Pump length in m} \\ L_{FM} & & \dots & & \text{Length of EMFM in m} \end{array}$ 

 $\begin{array}{cccc} n & & \dots & & \text{Number of pick-up coil turns} \\ n_{mag} & & \dots & & \text{Number of magnet pairs} \end{array}$ 

p ... Integer p = m/2 where m is an odd integer in finite length EMIP analysis

PO ... PMIP-EMFM calibration intercept in m<sup>3</sup>/hr

P1 ... PMIP-EMFM calibration slope

P<sub>nom</sub> ... Nominal reactor operating pressure in MPa

p<sub>loss</sub> ... Frictional pressure losses in Pa

 $p_{EM}$  ... Theoretical maximum pressure output in Pa  $p_{EM,exp}$  ... Experimental maximum pressure output in Pa

p<sub>EM,max</sub> ... Theoretical maximum pressure output neglect finite dimension effects in Pa

 $\begin{array}{cccc} Q & & \dots & & Volumetric \ flowrate \ in \ m^3/s \\ q & & \dots & Charge \ density \ in \ C/m^3 \\ R_{avg} & & \dots & Average \ channel \ radius \ in \ m \end{array}$ 

Rm<sub>f</sub> ... Magnetic Reynolds number evaluated in the fluid

... Correlation coefficient

s<sub>m</sub> ... Mean-slip

T ... Magnet thickness in m (direction of magnetization)

T<sub>boil</sub> ... Fluid boiling temperature at nominal reactor operating conditions in °C

T<sub>mag</sub> ... Magnet temperature in °C

T<sub>nbp</sub> ... Fluid boiling temperature at nominal atmospheric conditions in °C

T<sub>nom</sub> ... Nominal reactor operating temperature in °C

t ... Time in s

U<sub>0</sub> ... Mass averaged velocity in m/s

U<sub>B</sub> ... Magnet velocity evaluated at R<sub>avg</sub> in m/s

Fluid velocity vector in m/s  $V_{coil}$ Induced pick-up coil voltage in mV Resistive heating losses in the channel-walls in W  $W_{R,c}$ Resistive heating losses in the fluid in W  $W_{R,f}$ . . . Power input in W  $W_{in}$ Power losses in W  $W_{loss}$ Useful output power in W Wout . . . Unit vector along the channel width â . . . X Coordinate along the channel width in m ŷ Unit vector along the channel height Coordinate along the channel height in m y Ź. Unit vector along the pump length . . . Coordinate along the pump length in m Z Measured pressure differential in Pa Δр  $\Delta V_{\text{EMFM}}$ Measured EMFM voltage in V  $\nabla$ Gradient operator Momentum boundary layer thickness in m  $\delta_{\rm m}$ Magnetic skin thickness in m  $\delta_{\rm s}$ Thermal boundary layer thickness in m  $\delta_{\rm t}$ Permittivity of free space F/m  $\epsilon_0$ Experimentally calculated efficiency using the experimentally measured η  $\Delta p$  and input power  $W_{in}$ Ideal efficiency using  $p_{\text{EM}}$  and neglecting  $W_{\text{R.c.}}$  $\eta_{EM}$ Theoretical efficiency using  $p_{EM}$  and including  $W_{R,c}$  $\eta_{EM,ideal}$ . . . Calculated efficiency using experimentally defined p<sub>EM.exp</sub> and measured  $\eta_{EM,exp}$ . . . input power Win Magnetic field shape factor in 1/m Γ Eigenvalue λ Magnetic permeability in N/A<sup>2</sup> μ . . . Magnetic permeability of the fluid in N/A<sup>2</sup>  $\mu_f$ Fluid viscosity in Pa-s  $\mu_{\text{m}}$ Magnetic permeability of the channel wall in N/A<sup>2</sup>  $\mu_{\mathbf{w}}$ . . . Magnetic permeability of free-space in N/A<sup>2</sup>  $\mu_0$ Fluid density in kg/m<sup>3</sup> ρ EMFM channel electrical resistivity in ohm-m  $\rho_c$ Fluid electrical resistivity in ohm-m  $\rho_f$ Electrical conductivity in 1/ohm-m σ Electrical conductivity of the fluid in 1/ohm-m  $\sigma_{\rm f}$ Electrical conductivity of the channel in 1/ohm-m  $\sigma_{c}$ Torque in N-m τ Magnet pole-pitch evaluated at R<sub>avg</sub> in m  $\tau_{\mathrm{B}}$ . . . Angular frequency of the magnetic field in rad/s  $\omega_{B}$ Real component operator  $\Re$ Complex conjugate operator

Averaging operator

RMS operator

. . .

. . .

#### 1. INTRODUCTION

Liquid metals have gained renewed interest as an efficient energy carrier for applications ranging in concentrated solar, nuclear fission, and other industrial processes. Specifically, the nuclear sector is significantly interested in using elemental sodium metal as a reactor coolant. Development of liquid sodium began with its first nuclear application in the experimental submarine USS Seawolf (SSN-575). Commissioned in 1958, the Seawolf was a variant to the historic USS Nautilus (SSN-571), the very first nuclear powered submarine. These two submarines studied the performance of the Liquid Metal Fast Reactor (LMFR) and the Pressurized Water Reactor (PWR) plants for marine use, respectively. In the same time frame, land-based experimental research and commercial reactors were developing sodium as a reactor coolant. One of the first was the Sodium Reactor Experiment (SRE). Built between 1954 and 1957, the SRE developed and tested basic concept of sodium cooled reactors for commercial use. In the half-century since the SRE, several more experimental sodium cooled reactors were developed such as the Experimental Breeder Reactor-II (1964-1969), Enrico Fermi-I (1963-1972), the Integral Fast Reactor (1984-1994), and many more. In recent times, the United States Department of Energy (DOE) classified sodium metal as a candidate coolant for next generation reactor designs. Private vendors such as GE-Hitachi and TerraPower developed innovative reactor designs using sodium such as the PRISM and TWR, respectively. Lastly, sodium was selected as the coolant for the DOE's proposed Versatile Test Reactor. In total, for well over half a century elemental sodium has seen significant interest and development within the nuclear sector.

As a reactor coolant, the unique properties of sodium present several advantages. For example, Table 1-1 compares the nominal operating conditions of 1960's era water and sodium prototype commercial nuclear power plants [1].

Property	Fermi-I	Shippingport	Units	
P <sub>nom</sub>	0.10	15	MPa	
$T_{nom}$	400	270	${}^{\circ}C$	
ρ	858	780	$kg/m^3$ $kg/m^3$	
$\mu_{ m m}$	$2.8 \times 10^{-3}$	$1.0 \times 10-3$	$kg/m^3$	
$\mathbf{k}_{t}$	70	0.60	W/m-°C	
$c_p$	1.3	4.9	J/g-°C	
$T_{\mathrm{boil}}$	882	345	${}^{\circ}C$	

100

 ${}^{\circ}C$ 

850

 $T_{nbp} \\$ 

Table 1-1: Nominal operating conditions of the Enrico Fermi-I Sodium Cooled Reactor and the Shippingport Pressurized Water Reactor. Note that the sodium fluid properties were evaluated using Fink [2].

At nominal operating conditions, Table 1-1 shows that the density and viscosity of sodium and water are similar. Assuming only fluid properties change, the sodium-to-water boundary layer thickness ratio can be calculated using Equation 1-1 [3]. At nominal operating conditions, this ratio is about 1.5 which suggests that the momentum transfer behavior of sodium and water will be similar.

$$\frac{\delta_{\text{m,Na}}}{\delta_{\text{m,H}_2\text{O}}} = \sqrt{\frac{\mu_{\text{m,Na}}}{\mu_{\text{m,H}_2\text{O}}} \frac{\rho_{\text{H}_2\text{O}}}{\rho_{\text{Na}}}}$$
Equation 1-1

While the momentum transfer rates may be similar, the heat transfer rates are not. Table 1-1 shows that sodium's thermal conductivity is two orders of magnitude larger than water's. Assuming only fluid properties change, the sodium-to-water boundary layer thickness ratio can be calculated using Equation 1-2 [3]. At nominal operating conditions, this ratio is about 20 which suggests that sodium's heat transfer properties will be far superior to water's.

$$\frac{\delta_{t,Na}}{\delta_{t,H_{2}O}} = \sqrt{\frac{k_{t,Na}}{k_{t,H_{2}O}} \frac{\rho_{H_{2}O}}{\rho_{Na}} \frac{c_{p,H_{2}O}}{c_{p,Na}}}$$
Equation 1-2

Lastly, sodium's normal boiling point is higher than water's. Table 1-1 shows that sodium's normal boiling point is well over 800 °C while water's is 100 °C. Therefore, the nominal operating pressure of Fermi-I could be kept low while Shippingport's needed to be 15 MPa to prevent boiling. Therefore, sodium systems

can avoid pressurization and associated equipment while operating at higher temperatures with larger margins.

While in nuclear applications liquid metals have significant advantages as an energy carrier, a common need for all sectors is development of improved thermal hydraulic components like pumps, flowmeters, heat exchangers, impurity monitoring and control, and more. One of the most critical components is fluid mass transportation driven by pumps. Typically, mechanical pumps like Centrifugal pumps have filled this role for liquid metal systems [4]. However, there are challenges in their application to chemically reactive fluids like sodium. Firstly, sodium's reactivity impacts the shaft-seal design. Dynamic seals in direct contact with sodium are observed to fail due to excessive wear caused by reactions with the seal materials [5]. Therefore, shaft-seals are generally kept in gas spaces away from contacting the metal. This eliminates material compatibility considerations but constrains the pump to a vertical orientation [6]. Secondly, sodium's reactivity impacts bearing designs. Sodium has poor lubricating properties and can react with many common bearing lubricants [6]. Therefore, like pump seals, bearings are kept in the gas space away from directly contacting the metal [6]. Again, this eliminates the material compatibility issues but constrains the pump orientation. Lastly, Centrifugal pumps inhibit natural circulation due to the complex flow-path through the impeller and vanes [7]. Therefore, passive cooling methods desired in many new nuclear reactor designs may become more complex.

These challenges are important in nuclear where a driving factor is safety. For example, in 1959 the SRE experienced an undetected failure in one of the plant's centrifugal pumps [6] [8]. Figure 1-1 shows a sketch of the SRE mechanical pump seals and bearings. The seal-bearings system used two graphite, rubbing face seals, which were lubricated by an organic oil called Tetralin. While great care was taken in accommodating two chambers to collect a lubricant leak, a mistake in the chamber design allowed gas pressure to build in these chambers. The pressure build-up in these chambers prevented bearing lubrication, causing damage to the seal-bearing system. Consequently, Tetralin unknowingly leaking into the main reactor loop,

decomposed at the high temperatures, and created an insoluble organic-based compound. This compound coated the inside of several fuel channels which formed a flow restriction and caused severe damage to several fuel elements. Figure 1-2 shows an image of a damaged fuel element, demonstrating to consequences of pump-seal failure in reactive liquid metal systems [8].

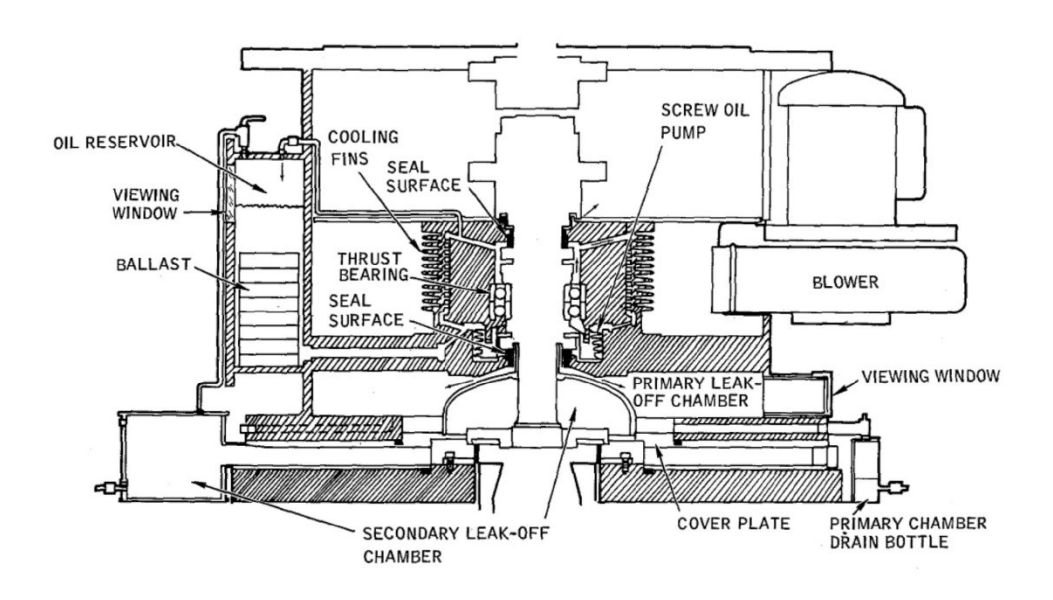


Figure 1-1: Diagram of the failed shaft seal-bearing system of the SRE centrifugal pumps [6] [8].

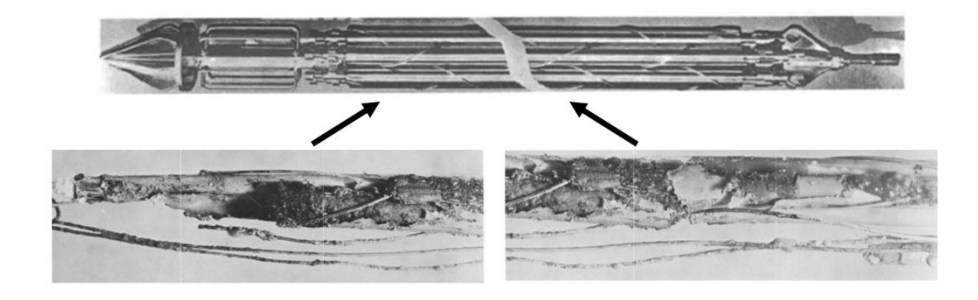


Figure 1-2: SRE fuel element damage resulting from the failed pump shaft seal-bearing system. On the top is a photo of an undamaged fuel element. On the bottom left is a portion near the bottom of the fuel assembly while on the bottom right is a portion near the middle of the fuel assembly [8].

An alternative to mechanical pumps for electrically conductive fluids is the Electromagnetic Induction Pump (EMIP). In contrast to Centrifugal pumps which use mechanical motion, EMIPs use traveling magnetic fields to produce pressure head. EMIPs have several advantages over mechanical pumps [4] [9] [10]. Firstly, EMIPs are hermetically sealed and therefore avoid complex seal designs, eliminating a

potential failure mode. Secondly, EMIPs have no rotating parts in direct contact with sodium. Therefore, these pumps avoid complex bearing designs and can use standard lubricants if needed. Thirdly, EMIPs components are mounted externally and avoid direct contact with the metal. Therefore, these pumps simplify material compatibility and repair procedures. Fourthly, EMIPs can operate in any orientation. These pumps do not have a free-surface limitation like many Centrifugal pump designs which may simplify plant design. Lastly, EMIPs have no impellers or vanes which may impeded the formation of natural circulation. Therefore, these pumps may simplify passive cooling systems and enhance plant safety.

These advantages were realized during the short sea trials of the USS Seawolf. Instead of complex mechanical pumps, the Seawolf used first-of-their-kind Flat Linear Induction Pump (FLIPs). Figure 1-3 shows an example of the General Electric designed pump. In comparison to the Nautilus mechanical pumps, the Seawolf FLIPs were found to be highly reliable despite being a relatively new development [11]. Additionally, the hermetically sealed conduit had the advantage of preventing sea water from contacting the metal in the case of a catastrophic failure. Lastly, the submarine was quieter than the Nautilus, likely due to fewer moving parts of the FLIP relatively to the Centrifugal pumps.

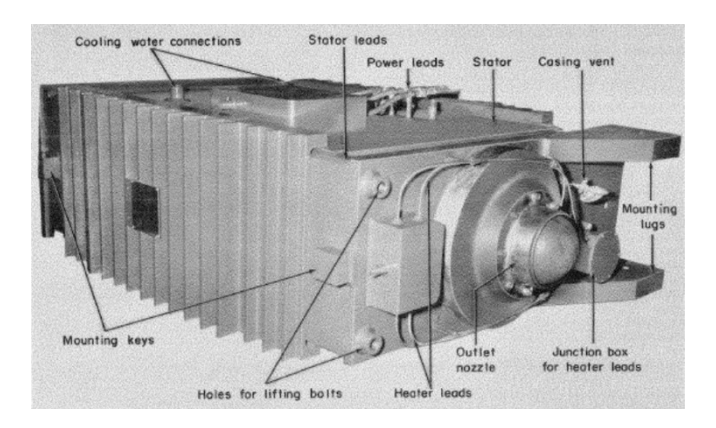


Figure 1-3: Photo of a General Electric Flat Linear Induction Pump (FLIP) similar to the model used in the USS Seawolf's sodium cooled reactor [12].

Since the initial development of the Seawolf's FLIPs in the 1950's, several subclasses of EMIPs using polyphase electric currents have been successfully developed. A common EMIP subclass is the Annular

Linear Induction Pump (ALIP). ALIPs have several advantages over the other EMIPs such as the FLIP. For example, an ALIP uses a circular flow conduit while a FLIP uses a square channel. Therefore, while a FLIP requires a complex reducer to transition from circular piping to a square channel, an ALIP uses a simple concentric reducer. Additionally, circular flow conduits have improved pressure performance over square channels. Lastly, ALIP's avoid the finite width effect and therefore have improved performance over FLIPs.

Recently, a new subclass of EMIPs have been developed called the Permanent Magnet Induction Pump (PMIP) also known as a Moving Magnet Pump (MMP) [13] [14] [15] [16]. In contrast to FLIPs and ALIPs which use polyphase electric currents, PMIPs use physically rotating arrays of permanent magnets. Like the other subclasses of EMIPs, PMIPs have clear advantages over mechanical pumps. However, the PMIP subclass has advantages over the FLIP and ALIP subclasses as well. For example, PMIP's are simple to design with little knowledge of three-phase electric power. Additionally, PMIPs are easy to construct using 'off the shelf' components.

To summarize, elemental sodium has seen significant interest as an efficiency energy carrier for concentrated solar, nuclear fission, and other industrial processes. In the nuclear sector, sodium is an ideal candidate for its excellent heat transfer and momentum properties and has seen development for over half a century. Since the first application in the USS Seawolf, several new and innovative commercial plants have been designed such as GE-Hitachi's PRISM and TerraPower's TWR. In nuclear applications, mass transport is driven by mechanical pumps. However, there are challengers in their application to chemically reactive fluids like sodium. These challenges pose significant safety concerns with bearing-seal failures and natural circulation cooling. As an alternative, liquid metals can be pumped using traveling magnetic fields with the EMIP. Compared to conventional mechanical pumps, EMIPs simplify design by avoiding direct contact of pump components with liquid metal and by eliminating high speed impellers, seals, and bearings. They also simplify plant design and safety by using unobstructed, low pressure drop, hermetically sealed flow conduits made of compatible materials. Some of these advantages were realized in the USS Seawolf

such as the high reliability, simplicity, and safety. However, since the development of the Seawolf's FLIPs, new EMIP designs like the ALIP and PMIP have realized even more advantages in their application to nuclear fission. Consequently, EMIPs in liquid metal systems have demonstrated significant value and importance in the future of the nuclear fission industry.

#### 1.1 MOTIVATION

While both EMIP subclasses have significant advantages over mechanical pumps, there are challenges applying these pumps to large scales. One challenge is the low efficiency of EMIPs. For example, ALIP's are observed to have efficiencies ranging from 5% to 45% [9] [11]. One component of the inefficiency is inherent to EMIPs. For example, energy is dissipated as resistive heating in the pump walls at low slip and in the fluid at high slip. However, another component of the inefficiency is from finite dimensional effects called edge effects. Literature has shown that the two primary edge effects are the Finite Length Effect and the Finite Width Effect.

The Finite Length Effect is observed in FLIPs and ALIPs and is the result of three factors. Firstly, at high  $Rm_f \cdot s_m$  the magnetic flux is carried in the fluid direction [17]. Consequently, the flux distribution becomes non-uniform along the pump length. Secondly, the finite length of the applied currents results in the formation of standing waves in the pump's active region [18] [19] [20]. This results in a pulsation of the fields especially at high  $Rm_f \cdot s_m$ . Lastly, the finite length of the ferromagnetic core results in the formation of large negatively oscillating braking forces at the pump inlet and outlet [19] [21]. This is a consequence of a step-change in the magnetic air-gap reluctance and increases with increasing  $Rm_f \cdot s_m$ . These three factors of the Finite Length Effect result in reduced pump performance relative to the ideal.

Several works have studied the Finite Length Effect and methods for its suppression [20] [22] [23] [24]. One method is to reduce the magnitude of the magnetic field by reducing the number of turns in the coils

at the inlet and outlet [20] [22]. However, only a single pair of papers have experimentally tested this method. Additionally, little work exists which investigates other methods of shaping the applied magnetic field. Therefore, several knowledge gaps exist in the suppression of the Finite Length Effect through adjustment of the inlet and outlet magnetic fields.

The Finite Width Effect is observed in FLIPs and PMIPs and is a direct result of current continuity [25] [26] [27]. In PMIPs, the induced current loops will have a component which produces no useful pumping force. Consequently, the PMIP performance is reduced relative to the ideal. This effect is exacerbated as the width of the pump becomes small relative to the current loops. Additionally, another finite width factor must be considered for PMIPs. Since PMIPs use finite width permanent magnets, the flux distribution across the channel width is non-uniform [15] [28]. Therefore, the non-uniform flux will result in reduced pump performance relative to the ideal. While some literature has analytically solved a finite channel and magnet width coefficient [15], little experimental work has been done to validate this coefficient. Additionally, very few works characterized the pressure-flowrate and efficiency performance of new PMIP designs. Therefore, several knowledge gaps exist in the understanding of the Finite Width Effect and total performance of a PMIP.

#### 1.2 OBJECTIVES

The objectives of this work are split into two parts. The first objective is studying the performance characteristics of a finite length Annular Linear Induction Pump. Additionally, this work also investigates two proposed methods of Finite Length Effect suppression. Thus, the primary ALIP objectives are listed as follows:

1) Characterized the pressure-flowrate and efficiency performance of a standard finite length ALIP and compare results to analytic theory.

- Measure the pressure-flowrate and efficiency performance of a 'Coil Shifted' ALIP. Evaluate 'Coil Shifting' method through comparison of baseline performance measurements.
- 3) Measure pressure-flowrate and efficiency performance of a 'Coil Graded' ALIP. Evaluate 'Coil Grading' method through comparison of baseline performance measurements.

The second objective of this work is studying the performance characteristics of a finite width Permanent Magnet Induction Pump. The primary PMIP objectives are listed as follows:

- 1) Characterize the pressure-flowrate and efficiency performance of a 12-Pole Double-Array Disc-Type PMIP in 200 °C and 400 °C sodium under frequencies of 30 Hz, 60 Hz, 75 Hz, and 90 Hz.
- 2) Verify the analytic PMIP finite width correction factors through comparison of experimental data evaluated under the same conditions.

In total, these objectives address significant knowledge gaps in the understanding of the performance characteristics and the impact the finite dimensions effects on ALIPs and PMIPs.

#### 1.3 APPROACH

Typically, a pump's performance is characterized through a pressure-flowrate ( $\Delta p$ -Q) performance and an efficiency-flowrate ( $\eta$ -Q) performance.  $\Delta p$ -Q performance is a basic metric used to characterize pumps and is simply defined as the measured differential pressure across the pump as a function of flowrate.  $\eta$ -Q performance is another basic matric used to characterize pumps. Equation 1-3 defines efficiency as the ratio of useful pressure-flowrate power output to the total power input.

$$\eta = \frac{\Delta p \cdot Q}{W_{in}}$$
Equation 1-3

Evaluating the impact of finite dimensional effects on ALIPs and PMIPs is approached by measuring these primary performance metrics. In the ALIP work, the  $\Delta p$ -Q and  $\eta$ -Q performance parameters are used to evaluate the effectiveness of the coil grading and coil shifting methods when compared to baseline measurements. Therefore, this approach assumes that the experimental ALIP exhibits the finite length effect. Consequently, if either the coil grading or coil shifting methods are observed to improve the baseline  $\Delta p$ -Q or  $\eta$ -Q performance, then the method is said to suppress the impact of the finite length effect. In the PMIP work, the  $\Delta p$ -Q and  $\eta$ -Q performance parameters are used to verify the theoretical predications of these parameters which account for the finite width channel and magnet.

#### 1.4 SUMMARY

Liquid metals have seen renewed interest as an energy carrier due to their superior heat transfer properties. In the nuclear sector, sodium is an excellent reactor coolant due to its superior heat transfer and momentum properties. Since sodium's first application in the USS Seawolf over half a century ago, several new and innovative commercial plants have been designed such as GE-Hitachi's PRISM and TerraPower's TWR. While liquid metals have significant advantages as an energy carrier in nuclear applications, a common need for all sectors is development of improved thermal hydraulic components like pumps. Typically, centrifugal pumps have filled the role for fluid mass transport. However, there are significant challenges in their applications to chemically reactive metals like sodium. As an alternative, liquid metals can be pumped using traveling magnetic fields with the EMIP. Compared to conventional mechanical pumps, EMIPs simplify design by avoiding direct contact of pump components with liquid metal and by eliminating high speed impellers, seals, and bearings. They also simplify plant design and safety by using unobstructed, low pressure drop, hermetically sealed flow conduits made of compatible materials. Consequently, EMIPs

applied in liquid metal systems have demonstrated significant value and importance in the future of the nuclear fission industry.

While EMIPs have significant advantages, their pressure performance and efficiencies are typically low. Some of these inefficiencies are inherent to EMIPs such as resistive heating in the channel walls and fluid. However, inefficiencies also arise from finite dimensional edge effects. These edge effects take the form of the Finite Length Effect in ALIPs and the Finite Width Effect in PMIPs. The Finite Length Effect has three factors which reduce the pressure performance and efficiency of ALIPs. Firstly, at large  $Rm_f \cdot s_m$  the magnetic flux in the fluid direction. Secondly, the finite length of the applied currents produces standing waves in the active region of the pump. Lastly, the finite length of the ferromagnetic core produces braking forces at the inlet and outlet of the pump. The Finite Width Effect has two factors which reduce the pressure performance and efficiency of PMIPs. Firstly, the finite width of the channel caused the induced currents to loop in the active region of the pump. Secondly, the non-uniform magnetic field from permanent magnets reduces the PMIP pressure output. Both the Finite Length and Finite Width Effect significantly impact the pressure performance and efficiency of ALIPs and PMIPs.

Several previous works have investigated both the Finite Length and Finite Width Effect in ALIPs and PMIPs respectively. This work aims to address some knowledge gaps in both the understanding of the performance characteristics and the impact of edge effects in ALIPs and PMIPs. Under ALIPs, only a single pair of papers investigate the impact of coil grading on the performance parameters of an ALIP. Additionally, little work exists on investigating other methods of shaping ALIP magnetic fields near the pump inlet and outlet such as coil shifting. Under PMIPs, little work exists which characterize key performance parameters of a 12-Pole Double-Array Disc-Type PMIP. Additionally, theoretical correction factors accounting for the finite dimensions of the channel and magnets need validation.

Understanding the behaviors of ALIPs and PMIPs as well as the impact of their finite dimensions is approached through measurement of key performance metrics. These include pressure-flowrate and efficiency-flowrate performance. In the ALIP work, these metrics are used to evaluate the effectives of coil shifting and coil grading when compared to the baseline performance. In the PMIP work, these metrics are used to provide engineers with useful pump curves and to validate the theoretically calculated performance parameters accounting for the finite width channel and magnets.

#### 2. THEORETICAL BACKGROUND

#### 2.1 ELECTROMAGNETIC INDUCTION PUMPING

#### 2.1.1 Principle of Operation

Electromagnetic Induction Pumps (EMIPs) are a type of pump used for electrically conducting fluids. In principle, Equation 2-1 describes the Lorentz Force produced by an EM pump [9]. Note that  $\mathbf{j}$  is the current density,  $\mathbf{B}$  is the magnetic field, and  $\mathbf{F}_{V}$  is the volume force density, also known as the pressure gradient.

$$\mathbf{F}_{V} = \mathbf{j} \times \mathbf{B}$$
  
Equation 2-1

By assuming the magnetic field and current density only has a single, constant component in the y-direction and x-direction respectively, Equation 2-1 can be simplified greatly. Thus, for a channel of height h<sub>ch</sub>, width 2·b, and length L, the ideal developed EM pressure is given in Equation 2-2.

$$p_{EM} = \frac{j_x B_y}{2 \cdot b \cdot h_{ch}} L$$
Equation 2-2

Of course, frictional pressure losses will exist. These losses are proportional to the square of the mean fluid velocity and take the form of Equation 2-3 where K is a loss coefficient and  $U_0$  is the characteristic velocity [29]. Now, Equation 2-4 estimates the developed pressure available for pumping.

$$p_{loss} = \frac{1}{2} \rho U_0^2 K$$
Equation 2-3

$$\begin{array}{c} \Delta p = p_{EM} - p_{loss} \\ \textit{Equation 2-4} \end{array}$$

#### 2.1.2 Analytical Solution of an Ideal EMIP

While useful conceptually, Equation 2-2 is impractical for EMIPs since the current density is rarely known a priori. Therefore, EMIP problems are solved using the Magnetohydrodynamic (MHD) Equations. These

equations are formed by the set of Maxwell Equations for the electromagnetic field and the Navier-Stokes Equations for the fluid field. Equation 2-5 to Equation 2-10 describe the Maxwell Equations neglecting displacement currents. Equation 2-11 and Equation 2-12 describe the Navier-Stokes Equations assuming an incompressible fluid.

$$\nabla \times \mathbf{E} = -\frac{\partial \mathbf{B}}{\partial t}$$
Equation 2-5
$$\nabla \cdot \mathbf{E} = \frac{q}{\epsilon_0}$$
Equation 2-6
$$\nabla \times \mathbf{B} = \mu \mathbf{j}$$
Equation 2-7
$$\nabla \cdot \mathbf{B} = 0$$
Equation 2-8
$$\mathbf{J} = \sigma(\mathbf{E} + \mathbf{u} \times \mathbf{B})$$
Equation 2-9
$$\nabla \cdot \mathbf{J} = 0$$
Equation 2-10
$$\rho \left(\frac{\partial \mathbf{u}}{\partial t} + (\mathbf{u} \cdot \nabla)\mathbf{u}\right) + \nabla p - \mu_m \nabla^2 \mathbf{u} = \mathbf{F}$$
Equation 2-11
$$\nabla \cdot \mathbf{u} = 0$$
Equation 2-12

Equation 2-5 through Equation 2-12 can be used to derive the Induction Equation [30] [31] [32]. The results of this derivation are shown in three useful forms. Firstly, Equation 2-13 is the Induction Equation in terms of the total magnetic field.

$$\nabla^2 \mathbf{B} = \mu \sigma \left( \frac{\partial \mathbf{B}}{\partial t} - \nabla \times (\mathbf{u} \times \mathbf{B}) \right)$$
Equation 2-13

Equation 2-13 can be expanded if the total magnetic field can be assumed to be a superposition of the applied external field  $\mathbf{B}_{e}$  and the induced fluid field  $\mathbf{B}_{i}$  as shown in Equation 2-14 [32]. Thus, Equation 2-13 can be written as Equation 2-15.

$$\begin{split} \mathbf{B} &= \mathbf{B}_{e} + \mathbf{B}_{i} \\ &\textit{Equation 2-14} \end{split}$$
 
$$\nabla^{2}\mathbf{B}_{i} - \mu\sigma \left(\frac{\partial \mathbf{B}_{i}}{\partial t} - (\mathbf{B}_{i} \cdot \nabla)\mathbf{u} + (\mathbf{u} \cdot \nabla)\mathbf{B}_{i}\right) = -\mu\sigma \left(\frac{\partial \mathbf{B}_{e}}{\partial t} - (\mathbf{B}_{e} \cdot \nabla)\mathbf{u} + (\mathbf{u} \cdot \nabla)\mathbf{B}_{e}\right) \\ &\textit{Equation 2-15} \end{split}$$

When solving 2D MHD problems, it is often useful to write Equation 2-15 in terms of a vector potential **A** defined in Equation 2-16 and Equation 2-17.

$$\nabla \times \mathbf{A} = \mathbf{B}$$
  
Equation 2-16

$$\nabla \cdot \mathbf{A} = 0$$
  
Equation 2-17

Thus, substituting Equation 2-16 into Equation 2-13 results in another form of the Induction Equation in Equation 2-18 which is the vector potential form [31].

$$\frac{\partial \mathbf{A}}{\partial t} = \frac{1}{\mu \sigma} \nabla^2 \mathbf{A} + \mathbf{u} \times \nabla \times \mathbf{A}$$
Equation 2-18

Closer inspection of Equation 2-18 provides valuable qualitative insight into the behavior of magnetic induction. Consider the nondimensionalized version of Equation 2-18 shown in Equation 2-19 where  $\widetilde{\mathbf{A}}$  and  $\widetilde{\mathbf{u}}$  are the nondimensional forms of  $\mathbf{A}$  and  $\mathbf{u}$  [30]. Note that the time rate of change of  $\widetilde{\mathbf{A}}$  is caused by diffusive effects given by the Laplacian term and advective effects given by the velocity term. The relative scaling of these two effects is governed by the Magnetic Reynolds Number  $\mathrm{Rm}_{\mathrm{f}}$ .

$$\frac{\partial \widetilde{\mathbf{A}}}{\partial t} = \frac{1}{\mathrm{Rm_f}} \nabla^2 \widetilde{\mathbf{A}} + \widetilde{\mathbf{u}} \times \nabla \times \widetilde{\mathbf{A}}$$
Equation 2-19

The Magnetic Reynolds Number for the fluid is defined Equation 2-20. This nondimensional parameter describes the relative effects of magnetic induction to magnetic diffusion. When Rm<sub>f</sub> is small, diffusion dominates and the solution is like a solid body solution. However when Rm<sub>f</sub> is large, convection dominates and a considerable entrance length may be required for the magnetic field to fully diffuse into the fluid.

$$Rm_{f} = \frac{\mu_{f}\sigma_{f}U_{B}}{k_{0}}$$
Equation 2-20

Note that  $k_0$  is the fundamental wave number, defined in Equation 2-21 where  $\tau_B$  is the pole pitch, or half-wavelength, of the magnetic wave.

$$k_0 = \frac{\pi}{\tau_B}$$
Equation 2-21

Also note that  $U_B$  is the velocity of the magnetic wave. This velocity, called the synchronous velocity, is defined in Equation 2-22 where  $f_B$  is the frequency.

$$U_B = 2\tau_B f_B$$
  
Equation 2-22

Now, the set of differential equations used to solve MHD induction problems are given in Equation 2-23 and Equation 2-24.

$$\frac{\partial \mathbf{A}}{\partial \mathbf{t}} = \frac{1}{\mu \sigma} \nabla^2 \mathbf{A} + \mathbf{u} \times \nabla \times \mathbf{A}$$
Equation 2-23

$$\rho \left( \frac{\partial \mathbf{u}}{\partial t} + (\mathbf{u} \cdot \nabla) \mathbf{u} \right) + \nabla p - \mu \nabla^2 \mathbf{u} = \mathbf{j} \times (\nabla \times \mathbf{A})$$
Equation 2-24

In practice, a general analytic solution to Equation 2-23 and Equation 2-24 is impossible. However, in specific special cases where the velocity profile is known, the differential equations can be decoupled and solved independently [10] [30]. One specific case for which an analytical solution can be obtained is the case where the fluid velocity is constant with time and uniform as in Equation 2-25.

$$\mathbf{u} = \mathbf{U}_0 \hat{\mathbf{z}}$$
Equation 2-25

This assumption is used to simplify the EMIP geometry. Figure 2-1 shows that the pump is assumed to be infinitely long in the z-direction and infinitely wide in the x-direction with a finite fluid thickness of in the y-direction. Note that the geometry in Figure 2-1 is Cartesian while the geometry in an ALIP is cylindrical. While an analytical solution exists in cylindrical coordinates [33], the added complexity of the axisymmetric solution does not provide additional insight into the physical phenomenon. This approximation is justified by assuming the ratio of channel height  $h_{ch}$  to mean channel radius  $R_{avg}$  is much smaller than unity [10] [30].

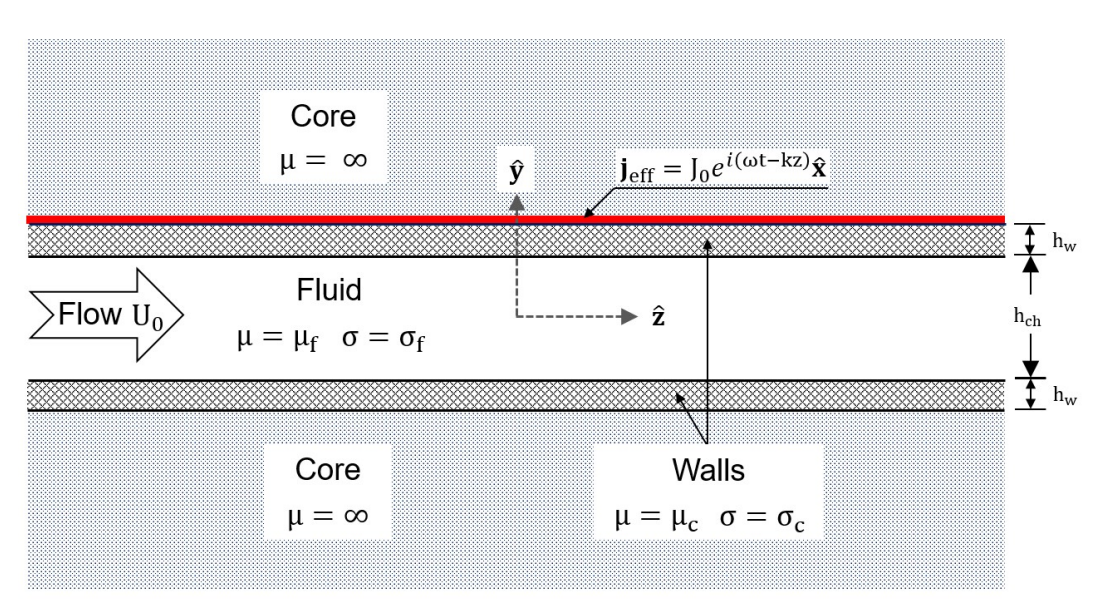


Figure 2-1: Simplified geometry for an idea EMIP.

The external magnetic field  $\mathbf{B}_e$  is produced by an infinitely thin current sheet with the form in Equation 2-26. Note that the pre-exponential factor  $J_0$  is the magnitude of the effective current sheet,  $\omega_B$  is the angular

frequency of the magnetic field, and  $k_0$  is the fundamental wave number. Additionally, that the value a is defined as  $a = 2 \cdot h_w + h_{ch}$ .

$$\begin{aligned} \boldsymbol{j}_{e}\left(\frac{a}{2},z,t\right) &= J_{0}e^{i\left(\omega_{B}t-k_{0}z\right)} \\ & \textit{Equation 2-26} \end{aligned}$$

A consequence of assuming a constant velocity is that the Induction Equation can be solved separately from the Fluid Equations. Furthermore, this implies that the vector potential **A** must have the same time dependence as the applied currents in Equation 2-26 [30]. Thus, Equation 2-27 gives the solution form for **A** where A the complex amplitude is. For simplicity, **A** is assumed to have a single component in the x-direction.

$$\begin{aligned} \textbf{A}(y,z,t) &= \dot{A}(y)e^{i(\omega_Bt-k_0z)}\hat{\textbf{x}} \\ &\textit{Equation 2-27} \end{aligned}$$

The simplified differential equation for the vector potential is shown in Equation 2-28 where  $\lambda^2$  is given by Equation 2-29 and  $s_m$  is given by Equation 2-30.

$$\frac{\partial^2 \dot{A}}{\partial y^2} - \lambda^2 \dot{A}(y) = 0$$
Equation 2-28

$$\lambda^2 = k_0^2 (1 + i \operatorname{Rm}_f \cdot s_m)$$
Equation 2-29

Note that Equation 2-30 is defined as the normalized difference between the synchronous velocity  $U_B$  and the mean fluid velocity  $U_0$ . This value is called the mean slip. Observe that as the mean slip approaches zero, the fluid is moving with the same velocity as the magnetic field and there is no relative motion. This implies that no EMF will be induced and likewise no currents will be induced.

$$s_{m} = 1 - \frac{U_{0}}{U_{B}}$$
Equation 2-30

Boundary conditions for Equation 2-28 are provided in Equation 2-31 and Equation 2-32.

$$\frac{\partial \dot{A}}{\partial y}\bigg|_{y=0} = 0$$
Equation 2-31

$$\left. \frac{\partial \dot{A}}{\partial y} \right|_{y=a/_{2}} = \mu_{f} J_{0}$$
 Equation 2-32

Equation 2-28 can be solved for the complex vector potential  $\bf A$ . Then,  $\bf A$  can be converted to the magnetic field  $\bf B$  which is averaged over the channel width assuming the effective channel width a is much smaller than the magnetic skin thickness  $\delta_s$  [32]. Equation 2-33 presents the height averaged complex amplitude of the magnetic field.

$$\langle \dot{B_y} \rangle |_y = \frac{\mu_f J_0}{a k_0} \frac{1}{1 + (Rm_f \cdot s_m)^2} (Rm_f \cdot s_m + i)$$
Equation 2-33

Equation 2-34 gives the height averaged complex amplitude of the current density in the fluid.

$$\langle j_x \rangle |_y = \frac{J_0}{a} \frac{Rm_f \cdot s_m}{1 + (Rm_f \cdot s_m)^2} (Rm_f \cdot s_m + i)$$
Equation 2-34

Equation 2-35 calculates the resulting force volume density, also known as the pressure gradient, where \* is the complex conjugate operator.

$$\nabla p_{EM} = \Re\{\mathbf{j}_{f} \times \mathbf{B}^*\}$$
Equation 2-35

Often it is desired to know the time averaged electromagnetic force. This can be calculated by taking the root-mean-square (RMS) value of  $\mathbf{j}_f$  and  $\mathbf{B}$ . Equation 2-36 gives the RMS value of the height averaged EM pressure gradient.

$$\overline{\nabla p_{EM}} = \frac{1}{2} \Re \{ \langle j_x \rangle |_y \langle \dot{B_y} \rangle |_y^* \}$$
Equation 2-36

Equation 2-37 presents the RMS value of the average EM pressure gradient where Equation 2-38 describes  $B_{y,0}$ . Note that  $B_{y,0}$  is defined as the height averaged amplitude of the total magnetic field.

$$\overline{\nabla p_{EM}} = \frac{1}{2} \sigma_f B_{y,0}^2 (U_B - U_0)$$
Equation 2-37

$$B_{y,0} = \frac{\mu_f J_0}{k_0 a \sqrt{1 + (Rm_f \cdot s_m)^2}}$$
Equation 2-38

The amplitude of the external field is found by setting  $Rm_f \cdot s_m$  equal to zero. Note that this is the case where there is no relative motion and therefore no induced currents. Thus, Equation 2-39 gives the form of  $B_{y,e}$ .

$$B_{y,e} = \frac{\mu_f J_0}{k_0}$$
Equation 2-39

The calculated pressure gradient can then be substituted into the Navier-Stokes Equations in Equation 2-11 to find the total pressure gradient in the pump [10] [30] [32]. As discussed earlier, in the case of the constant velocity assumption the pressure gradient can be simply split into two components shown in Equation 2-40. The quantity  $p_{EM}$  represents the pressure developed by the EM body force while the quantity  $p_{loss}$  represents the frictional losses.

$$\Delta p = p_{EM} - p_{loss}$$
Equation 2-40

Then, Equation 2-41 can be used to calculate the RMS value of the height averaged EM developed pressure.

$$p_{EM} = \int_{0}^{L} \overline{\nabla p_{EM}} dz$$
Equation 2-41

In this case, the time averaged electromagnetic body force is constant everywhere. Thus, Equation 2-41 becomes trivial and Equation 2-42 gives the electromagnetic induced pressure. This is the maximum possible pressure that can be developed by an EMIP. This form shows that the pressure is linearly proportional to the length of the pump, relative velocity, and fluid conductivity. However, the pressure is proportional to the square of the height averaged magnetic field.

$$p_{EM} = \frac{1}{2} \sigma_f B_{y,0}^2 (U_B - U_0) L$$
Equation 2-42

The average EM pressure gradient in Equation 2-42 can now be written as a function of  $Rm_f \cdot s_m$  as in Equation 2-43.

$$p_{EM} = p_{EM,max} \cdot \frac{Rm_f \cdot s_m}{1 + (Rm_f \cdot s_m)^2}$$
Equation 2-43

$$p_{EM,max} = \frac{1}{2} \frac{k_0}{\mu_f} B_{y,e}^2 L$$
Equation 2-44

Figure 2-2 presents a normalized plot of Equation 2-43 as a function of  $Rm_f \cdot s_m$ . As discussed earlier, when  $Rm_f$  is small, diffusion dominates advection. In this regime of Figure 2-2, the pressure output for an ideal EMIP increases linearly. However, as  $Rm_f$  increases, advection dominates diffusion and the pressure output for an ideal EMIP deceases. This is a common observation for EMIPs [32] [34] [35].

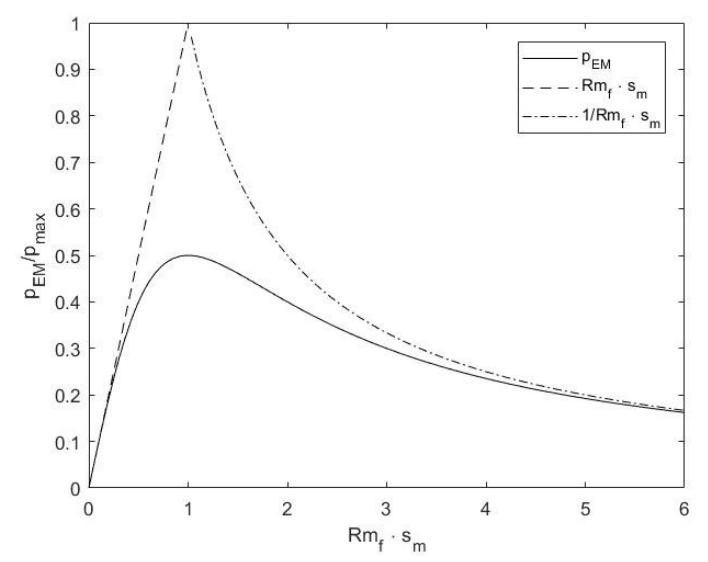


Figure 2-2: Normalized pressure output of an ideal EMIP as a function of  $Rm_f \cdot s_m$ . Note that as  $Rm_f \cdot s_m$  passes unity, the developed pressure decreases which is a common observation in EMIPs [32] [34] [35].

Equation 2-45 calculates the efficiency of an induction pump which is defined as the ratio of electromagnetic power to electrical power.

$$\eta_{EM} = \frac{W_{EM}}{W_{in}}$$
Equation 2-45

Equation 2-46 shows that the electromagnetic power delivered to the fluid is simply the volume integral of the product between the developed EM pressure gradient and the fluid velocity.

$$W_{EM} = \iiint \langle \nabla p_{EM} \rangle \cdot \mathbf{u} dV$$
Equation 2-46

The total electrical power can be found by an energy balance on the pump system. As shown in Equation 2-47, the total electrical energy is the sum of the developed EM pressure gradient, frictional pressure losses, and other losses.

$$W_{in} = p_{EM}Q + p_{loss}Q + W_{R,f} + W_{R,c} + W_{loss}$$
Equation 2-47

 $W_{R,f}$  and  $W_{R,c}$  in Equation 2-47 are resistive heating losses in the fluid and channel walls, respectively. These losses are defined in Equation 2-48 where  $J_{(f,c)}$  is the induced current density in either the fluid or walls and \* denotes the complex conjugate operator [36].

$$W_{R,(f,c)} = \iiint \frac{\mathbf{J}_{(f,c)} \cdot \mathbf{J}_{(f,c)}^*}{2\sigma_{(f,c)}} dV$$
Equation 2-48

Equation 2-48 can be evaluated analytically using the induced current density terms  $J_{(f,c)}$  found in the Induction Equation solution. Thus, Equation 2-49 and Equation 2-50 presented the resistive heating losses in the fluid and walls, respectively [14].

$$W_{R,f} = \frac{1}{2}\sigma_{f}L(h_{ch} \cdot 2 \cdot b)(U_{B} - U_{0})^{2}B_{0}^{2}$$
Equation 2-49

$$W_{R,c} = \frac{1}{2}\sigma_c L(2 \cdot h_w \cdot 2 \cdot b) U_B^2 B_0^2$$
Equation 2-50

In an ideal ALIP the efficiency is defined in Equation 2-51 where frictional pressure losses, resistive heating losses, and other losses are neglected. Under these assumptions, Equation 2-52 shows that the efficiency is linear with the mean-slip [36].

$$\eta_{EM,ideal} = \frac{p_{EM}Q}{p_{EM}Q + W_{R,f}}$$
 Equation 2-51

$$\eta_{EM,ideal} = 1 - s_m$$
 Equation 2-52

However, for real ALIPs much of the energy is dissipated as resistive heating in the pump walls during low slips. Therefore, as at s<sub>m</sub> approaches zero the efficiency is expected to decrease. This reality is reflected in Equation 2-53 which describes this new theoretical efficiency.

$$\eta_{EM} = \frac{p_{EM}Q}{p_{EM}Q + W_{R,f} + W_{R,c}}$$
Equation 2-53

By considering resistive heating losses in the pump walls, an ALIP's efficiency will decrease significantly at low slips. Figure 2-3 plots the ideal efficiency with the theoretical ALIP efficiency as a function of meanslip. For a small scale ALIP, the maximum theoretical efficiency is about 40% at a mean slip of 30%.

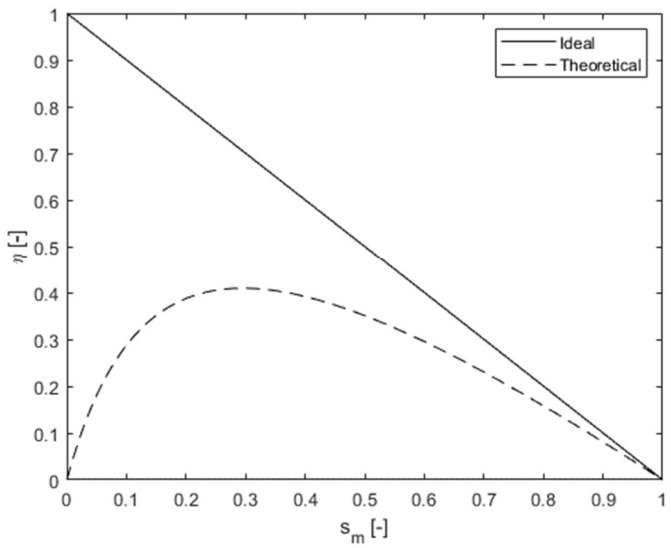


Figure 2-3: Ideal EMIP efficiency plotted with the analytically calculated ALIP efficiency as a function of mean-slip.

#### 2.2 THE ANNULAR LINEAR INDUCTION PUMP

# 2.2.1 Fundamental Components

In principle, an ALIP can be derived from an Asynchronous Induction Motor (AIM) [37]. Like an AIM, an ALIP uses polyphase electric coils which establish a magnetic wave that travels down the length of the pump. Figure 2-4 shows a cross-section of an ALIP channel [9]. Here, the magnetic field is oriented radially across the channel width. Induced currents flow azimuthally in the channel and react with the total magnetic field to produce a Lorentz Force directed in the axial direction. In general, the coils are pancake shaped, slipped over the pump channel, and set in stacks of comb-shaped puchings called the outer ferromagnetic core [9]. The outer and inner cores provide a similar function as the stator in an AIM by providing a low magnetic resistance, or reluctance, path for the magnetic flux lines.

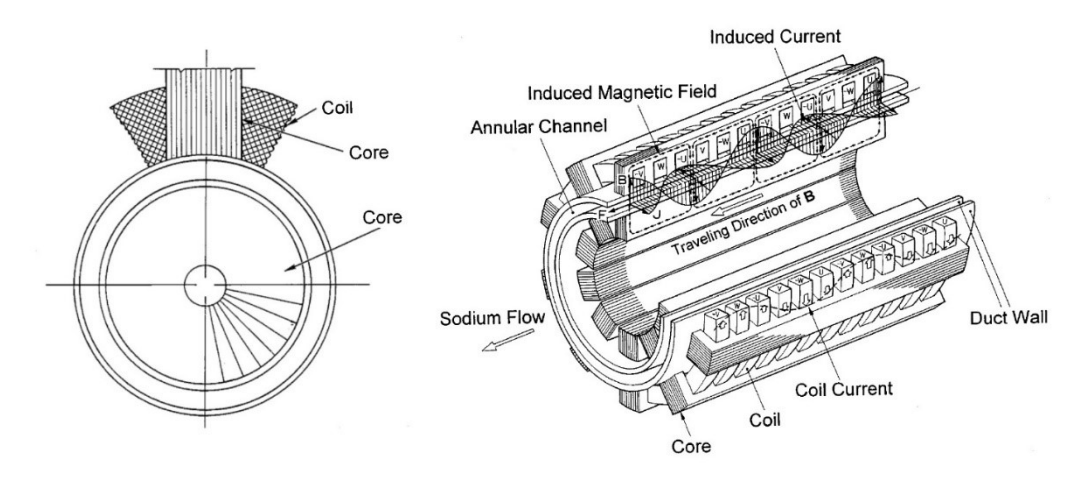


Figure 2-4: On the left is a cross-section of the pump. A cut-away of a practical ALIP [9].

## 2.2.2 Analytical Solution of a Finite Length Pump

Analysis of the non-dimensionalized Induction Equation showed that the time rate of change of  $\widetilde{\mathbf{A}}$  was due to diffusion and advection. For small Rm<sub>f</sub>, diffusion dominates and the solution will be like that of a stationary conductor [30]. However, for large Rm<sub>f</sub>, advection dominates causing a considerable distance for  $\widetilde{\mathbf{A}}$  to fully diffuse into the fluid [30]. This suggests that important physical behavior may be missed by neglecting the finite length of the pump. The finite length of the applied currents was considered in the

analytic solution developed by Valdmanis [18]. Figure 2-5 shows the new geometry and material assumptions. As before, the pump is assumed to be infinitely wide. Note that the effective current sheet is now a finite length L and is constrained to  $L = 2 \tau_B p$  where p is the number of pole pairs.

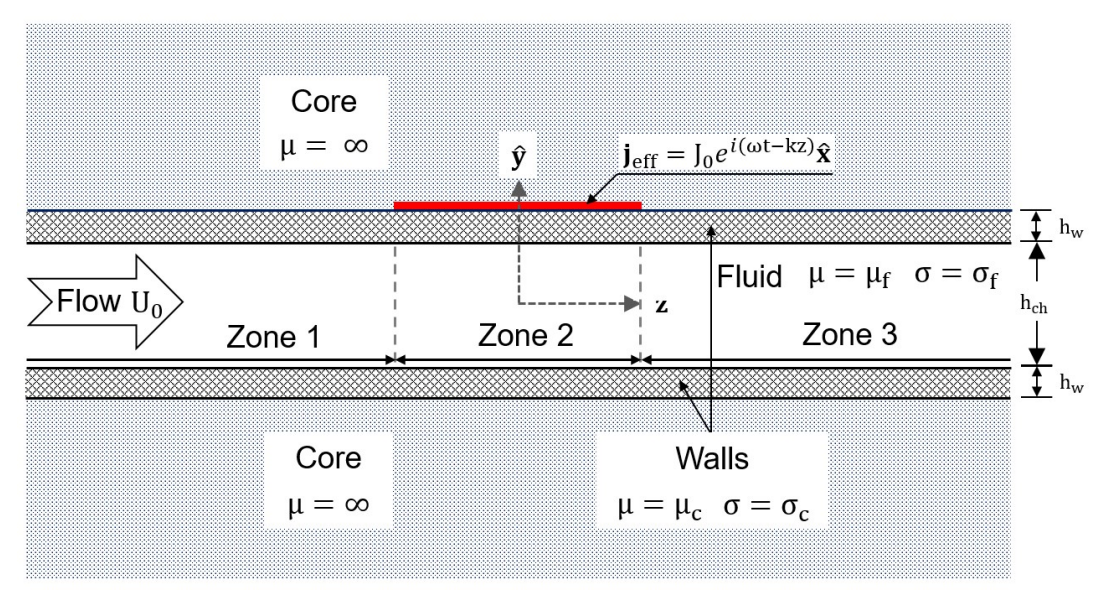


Figure 2-5: Simplified geometry for a finite length, infinite width, EMIP [32].

A full solution to the problem will not be presented. Rather, the results will be summarized and compared to the ideal solution. Full details of the solution can be found in Valdmanis's and Kirillov's work [18] [19]. Zone One and Zone Three are defined as the entrance and exit of the pump respectively, while Zone Two is defined as the inductor zone. The external magnetic field amplitude solutions for Zone One through Zone Three are given in Equation 2-54 and Equation 2-55.

$$\begin{split} \dot{B}_{y,e}^{(1,3)} &= \frac{\mu_f J_0}{k} sin(\pi p) cos(\omega_B t) \\ &= \frac{Equation \ 2\text{-}54}{k} \\ \dot{B}_{y,e}^{(1,3)} &= \frac{\mu_f J_0}{k} (sin(\omega_B t - kz) - cos(\pi p) sin(\omega_B t)) \\ &= \frac{Equation \ 2\text{-}55}{k} \end{split}$$

Note that Equation 2-54 and Equation 2-55 are in the same form as the external magnetic field in Equation 2-56 that was derived earlier. However, now the external field pulsates. Note that if the number of pole

pairs is odd, which corresponds to p = m/2 where m is an odd integer, then the pulsation disappears from Zone Two and appears in Zone One and Zone Three. If the number of pole pairs is even, which corresponds to p = n where n is any integer, then the pulsating component appears in the Zone Two and disappears in the Zone One and Zone Three. In practical ALIPs, the number of pole pairs will always be even. Therefore, this theory predicts a pulsating field in Zone Two, the active region of the pump.

$$\dot{B}_{y,e}^{(1,3)} = \frac{\mu_f J_0}{k}$$
Equation 2-56

Kirillov noted that the pulsating fields occur for ferromagnetic cores of infinite length. However, Kirillov also noted that the same behavior could be achieved for a ferromagnetic core which was sufficient long. His results showed that if Equation 2-57 was satisfied then the behavior of the pump was like that of infinitely longer ferromagnetic core. As this ratio decreases, the pulsating braking forces appear at the pump inlet and outlet. Note in Equation 2-57 that Y is the ferromagnetic core length beyond the active pump region.

$$\frac{Y}{\tau_B} \ge 0.32$$
Equation 2-57

While this model is simplistic, it shows that the finite length effect is purely electromagnetic and arises from the finite length of the applied currents. Note that this problem was solved under the constant velocity assumption which decoupled the Induction Equation from the Navier-Stokes Equations. Therefore, no fluid effects were considered in this solution. However, a finite length region was considered which produced a pulsating magnetic field that was independent of the flow. This phenomena did not appear in the infinite length solution. Thus, the finite length effect appears to be purely electromagnetic arising from the finite length of the applied currents and under certain conditions the finite length of the ferromagnetic core.

# 2.2.3 Effects of the Finite Length

While the analytical solution in the previous section provided useful insight into the finite length effect, the solution lacked details of a real ALIP. For example, the previous analysis neglected the finite width of the coils and the stator cores. Also neglected in the previous analysis were fluid dynamic effects such as a velocity profile, acceleration, and turbulence which couple the Induction Equation with the Navier-Stokes Equations. Therefore, this section will review analytical, numerical, and experimental work on the finite length effect that encompass more detail than the simple analytical solution.

Numerical models have the advantage of considering more detail than the analytical solutions reviewed earlier. In addition to capturing finite length effects, these models can also couple the Induction Equation with the Navier-Stokes Equations [20] [24] [35] [38]. Furthermore, some models have also tried to capture the finite width polyphase coils [38]. Thus, numerical models may provide more insights into the behavior of finite length effects than analytical solutions.

Numerical models considering a finite length ferromagnetic core predict a severe braking forces at the inlet outlet of the pump [20] [24] [35]. Figure 2-6 shows a numerical solution of the EM force density as a function of the length of the pump [20]. At the entrance and exit of the pump, large, negative, and oscillating braking forces appear. These forces are consistent with what was observed in the analytic theory discussed earlier and appear to be a direct result of the finite length ferromagnetic core.

A similar model was constructed by Roman [35]. Figure 2-7 shows that in addition to braking forces there is a suppression of the EM force density near the entrance of the pump which increases with the fluid velocity. This is consistent with the Induction Equation scaling arguments and the analytical finite length effect theory.

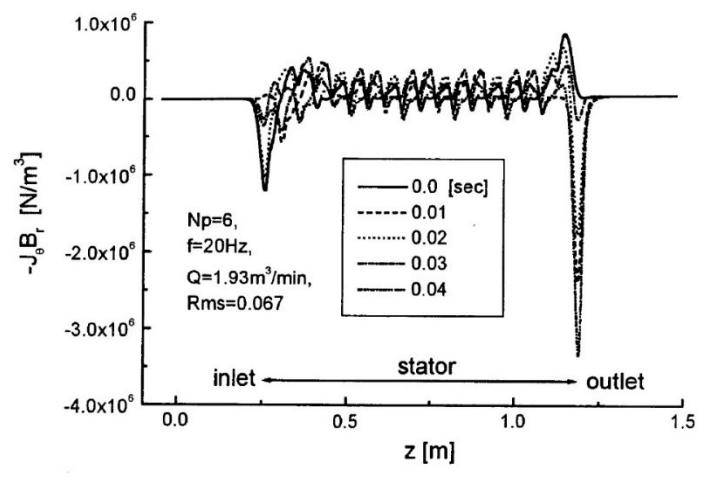


Figure 2-6: Numerical model of the force density along the length of an ALIP. In this model, large negative force pulsations developed at the entrance and exit of the pump, with the exit braking force have a larger magnitude than the entrance braking force [20].

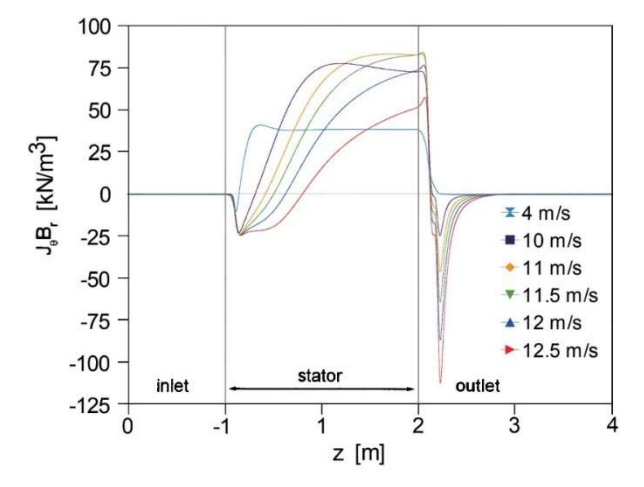


Figure 2-7: Numerical model of the time averaged force density along the length of an ALIP. This model also predicts large negative braking forces at the inlet and exit of the pump [35].

In addition to predicting large braking forces and magnetic field suppression, numerical models have also predicted the presence of pressure pulsations at low magnetic field frequencies [20] [38]. Figure 2-8 plots the deviation of pressure from the mean output as a function of time for a pumping operating at 50 Hz [38]. Also plotted is the pressure frequency spectrum. A distinct peak is observed at 100 Hz. It was found that as the supply frequency changed, the peak in pressure pulsation was always twice that of supply frequency. Thus, these pulsations were called Double Supply Frequency (DSF) pressure pulsations.

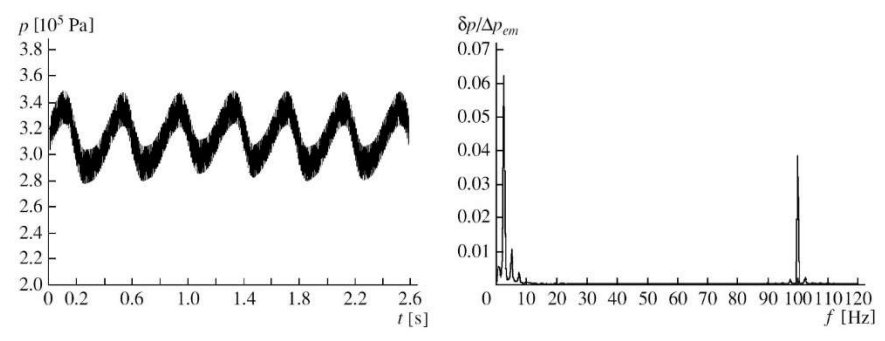


Figure 2-8: Numerical model of pressure pulsations in a finite length ALIP. These pressure pulsations were found to occur at twice the supply frequency of the pump [38].

Numerical models have predicted that DSF pressure pulsation magnitude is a function of slip [20]. Figure 2-9 shows the pulsation magnitude versus slip for a pump operating at 20 Hz [20]. At low values of slip, the magnitude of the DSF pulsations is observed to reach near 40% of the mean pressure output.

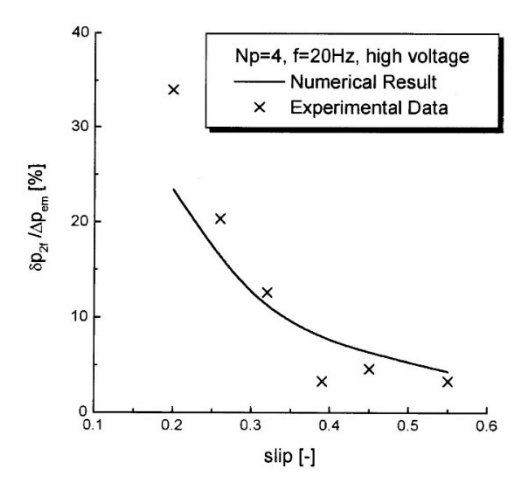


Figure 2-9: Numerical and experimental comparison of DSF pulsation magnitude as a function of slip [20].

Experimental measurements have confirmed the existence of DSF pulsations predicted by the numerical models [22]. Figure 2-10 shows a graph of the experimentally measured pressure pulsation and its frequency spectrum. For a pump operating at 20 Hz and the conditions specified in Figure 2-10, a pressure deviation of 4% was observed with a frequency of 40 Hz.

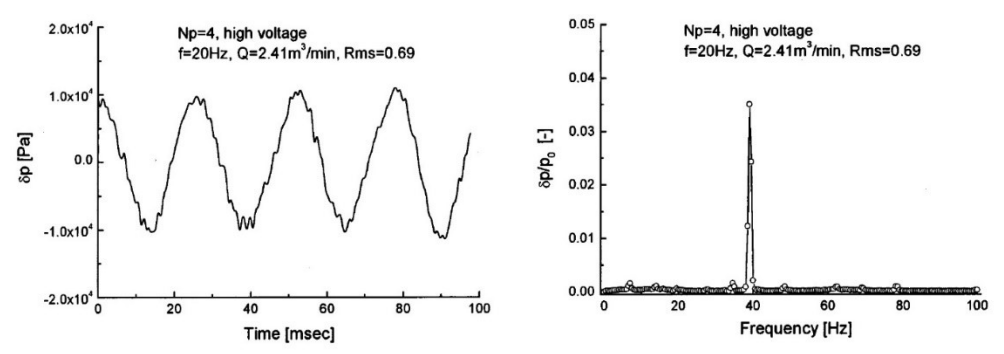


Figure 2-10: Experimental measurements of DSF pulsations in a finite length ALIP [22].

Araseki then investigated the magnitude of the DSF pulsation as a function of slip and supply frequency. The experimental results in Figure 2-11 confirm the dependence of pulsation magnitude on slip [22]. Additionally, for a fixed value of slip, the magnitude of the DSF pulsation increases as the supply frequency decreases. In some cases, the magnitude of the pulsation can reach up to 50% of the mean developed pressure.

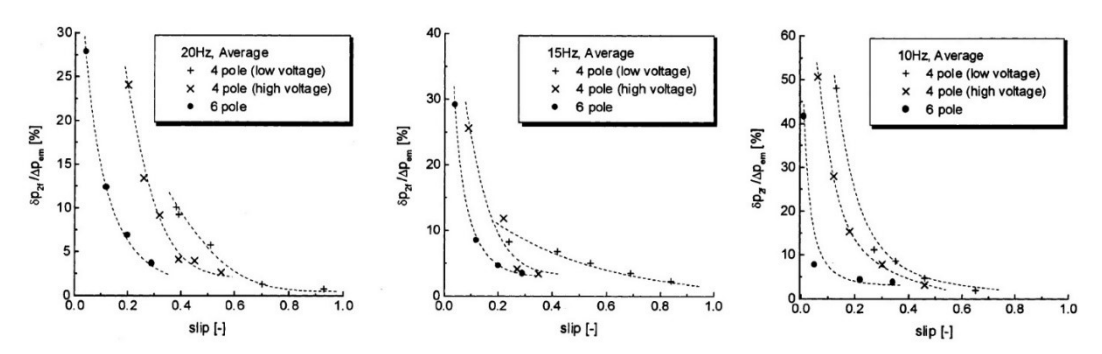


Figure 2-11: Experimental measurement of DSF pulsation magnitude as a function of slip and supply frequency [22].

This experimental study would seem to suggest that reducing the DSF pulsation magnitude could be simply achieved by running the pump at high supply frequencies. However, two criterions may be violated with this method. Firstly, stable operation is ensured by Equation 2-58 which requires  $Rm_f \cdot s_m$  be less than unity. However, note that increasing the supply frequency will directly increase  $Rm_f \cdot s_m$ .

$$Rm_f \cdot s_m = \frac{\mu_f \sigma_f \omega_B}{k_0^2} s_m \le 1$$
Equation 2-58

Secondly, full magnetic diffusion is ensured by Equation 2-59 which requires the channel width to magnetic skin thickness ratio be many orders less than unity. However, increasing the supply frequency will push this ratio towards unity. Thus, two fundamental criterions may be violated by increasing the supply frequency and the pump may be pushed out of its optimal operating regime [22].

$$\frac{a}{\delta_s} = a \sqrt{\frac{\mu_f \sigma_f \omega_B}{2}} s_m \ll 1$$
Equation 2-59

However, DSF pulsations can be avoided by tapering the magnetic field at the ends of the pump [10] [39] [22]. This tapering, called coil grading, is accomplished by decreasing the number of turns in the polyphase coils at the entrance and exit of the pump. Three coil grading configurations were experimentally studied by Araseki. In this particular ALIP, the pole pitch corresponded to 6 coils and the pump had a total of 36 coils. Therefore, 1/3 to 2/3 of the total pump length could be graded.

Experimental results show that tapering the magnetic field reduces the DSF pulsation magnitude. Figure 2-12 shows that in the low slip regime of 0.1, linear grading over one-pole length at both stator ends reduced the amplitude of the pressure pulsation to about 1/2 of the non-grading configuration [22]. This was found to have a positive impact on the efficiency of the pump. Figure 2-13 shows that while coil grading did not impact the pressure-flowrate performance, it did lower the electrical input power [22]. In this configuration, the efficiency of the pump was increased by as much as 10%. Compared to normal efficiencies of ALIPs which can range from 5% to 45%, a 10% increase in efficiency is significant.

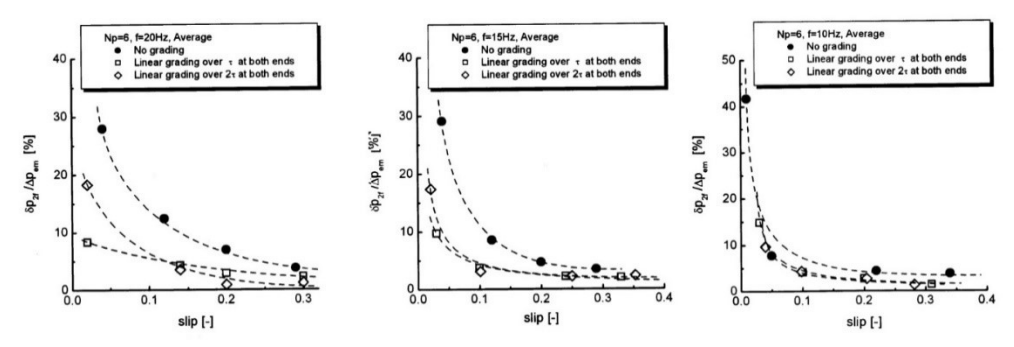


Figure 2-12: The reduction in DSF pulsation magnitude as a function of coil grading at three pump frequencies [22].

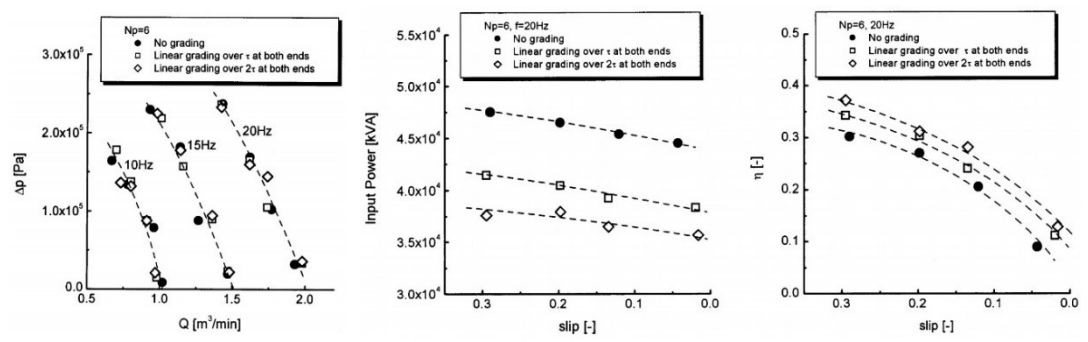


Figure 2-13: The reduction of electrical input power and resulting increase of efficiency as a function of coil grading [22].

## 2.2.4 Summary

In total, this literature review presented the fundamental ALIP theory which can be used to estimate the output pressure and efficiency performance for an infinite length pump. Additionally, the literature review identified that the primary ALIP edge effect is the Finite Length Effect. Literature showed that three factors characterize the Finite Length Effect. Firstly, at high  $Rm_f \cdot s_m$  the magnetic flux becomes carried in the fluid direction. Consequently, the flux distribution becomes non-uniform along the pump length. Secondly, the finite length of the applied currents results in the formation of standing waves in the pump's active region. This results in a pulsation of the fields especially at high  $Rm_f \cdot s_m$ . Lastly, the finite length of the ferromagnetic core results in the formation of large negatively oscillating braking forces at the pump inlet and outlet. This is a consequence of a step-change in the magnetic air-gap reluctance and increases with increasing  $Rm_f \cdot s_m$ . These three factors of the Finite Length Effect result in reduced pump performance relative to the ideal. Tapering of the inlet and outlet magnetic field by Coil Grading was identified as a

successful method of improving pump efficiency. However, only a single pair of papers have investigated this method and there exists a lack of work investigating other methods of magnetic field tapering.

#### 2.3 THE PERMANENT MAGNET INDUCTION PUMP

#### 2.3.1 Fundamental Components

Permanent Magnet Induction Pumps (PMIPs), also known as Moving Magnet Pumps (MMP) are a subclass of EMIPs used to pump electrically conducting fluids [9] [40]. In contrast to FLIPs and ALIPs which use polyphase electric coils to generate a magnetic field, a PMIP uses a physically rotating array of alternating polarity permanent magnets [9]. Figure 2-14 shows two array arrangements that have been successfully developed and tested. One arrangement fixes the magnets to a rotating drum [13] [14]. The other arrangement fixes the magnets to a circular disc [14] [15] [16]. Both arrays are rotated near a square flow channel to which the magnetic field is oriented orthogonally. Additionally, the Drum-Type PMIP may use a ferromagnetic yoke on the outer channel wall while the Disc-Type may use an additional magnet-array below the channel [28] [41].

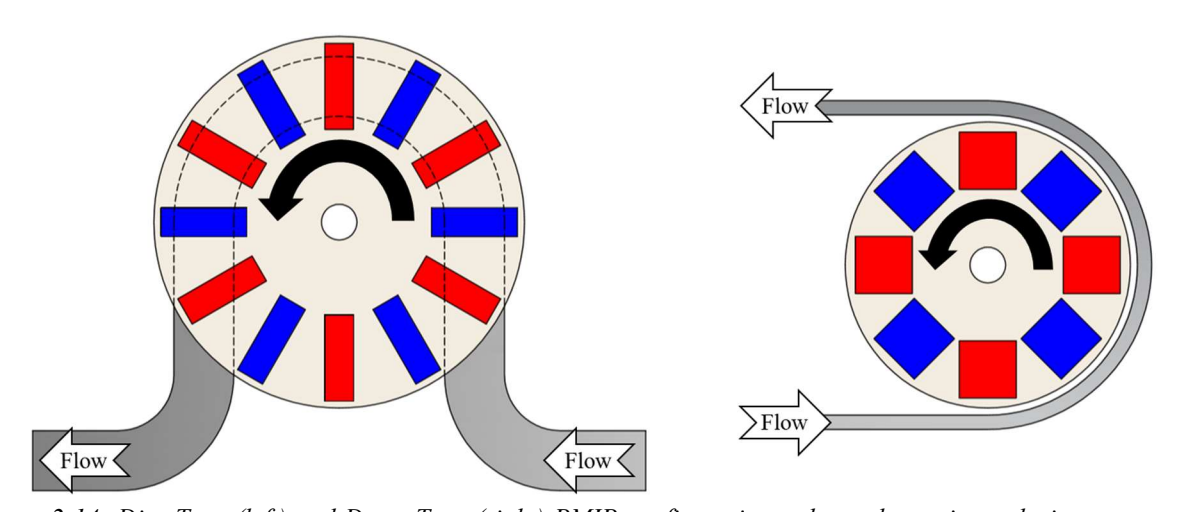


Figure 2-14: Disc-Type (left) and Drum-Type (right) PMIP configurations where alternating polarity magnets are denoted as blue or red. The Disc-Type configuration can also have an additional magnet-array on bottom with the flow channel located in the middle.

# 2.3.2 Analytical Solution of a Finite Width Pump

Theoretical calculations of a PMIP's pressure output and efficiency have been solved using the Induction Equation [10] [25] [36] [42] and will be reviewed in this section. Many simplifying assumptions are used to make an analytical solution tractable. One group of assumptions simplifies the geometry by ignoring

finite length edge effects and radial effects [10] [15] [16] [25]. Therefore, the Induction Equation can be solved in Cartesian coordinates using the cross-section shown in Figure 2-15. Note that the flow channel has a height of  $h_{ch}$  while the top and bottom channel walls have a height of  $h_{w}$ . Height's  $h_{ch}$  and  $h_{w}$  are assumed to be small enough such that quantities in the  $\hat{y}$  direction can be averaged [10] [25] [36]. Both flow channel and channel walls have a width of  $2 \cdot b$  and both are assumed to be electrically insulated from each other [42]. Note that the finite conductivity channel sidewalls are ignored in this analysis.

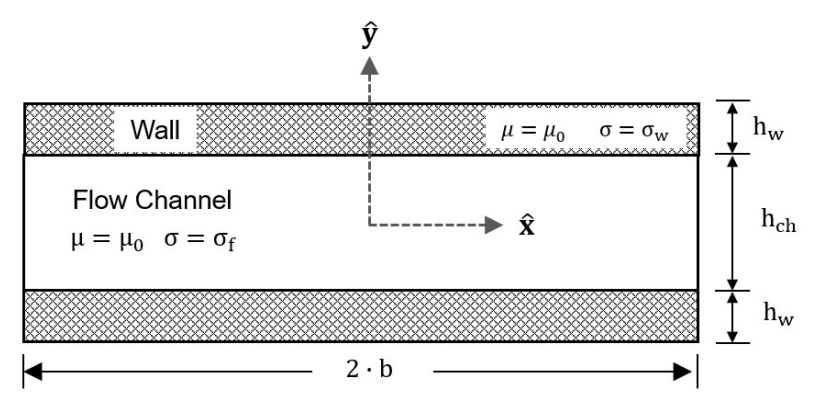


Figure 2-15: Simplified geometry in the solution of the Induction Equation for a PMIP. Note that the flow channel and both upper and lower channel walls are assumed to be electrically insulated from each other. Also note that no channel sidewalls exist.

Another group of assumptions simplifies the magnetic field to a purely sinusoidal, single component field with the form of Equation 2-60 [9] [15] [25]. Additionally, the wave is assumed to be composed of a single, fundamental component, with a constant wave speed  $\omega_B t - k_0 z$  [25]. Note that for these calculations, the amplitude may vary in the x-direction, but are assumed to be symmetric about the y-axis [42]. This field is assumed to be a known and is applied across the pump cross-section in Figure 2-15 [15].

$$\mathbf{B}_{e} = B_{e,y}(\mathbf{x}) \cdot e^{i(\omega_{B}t - k_{0}z)} \hat{\mathbf{y}}$$
Equation 2-60

Lastly, the fluid is assumed to flow as a solid-body allowing the EM Equations to be decoupled from the Fluid Equations [10] [25] [42]. Therefore, the fluid velocity has a single, constant component in the z-direction as shown in Equation 2-61.

$$\mathbf{u} = \mathbf{U}_0 \mathbf{\hat{z}}$$
*Equation 2-61*

As discussed earlier, a pump's performance is typically characterized by its output pressure as a function of flowrate. The output pressure is the pressure difference measured between a point near the pump's inlet and outlet. As shown in Equation 2-62, this measurement can be written as a maximum developed pressure  $p_{max}$  that is reduced by frictional losses  $p_{loss}$ .

$$\Delta p = p_{\text{max}} - p_{\text{loss}}$$
Equation 2-62

An EMIP's maximum output pressure can be estimated theoretically by solving the Induction Equation. Literature has shown that an EMIP without finite width or length edge effects develops a maximum pressure that follows the form of Equation 2-63 [9] [25] where  $\sigma_f$  is the fluid electrical conductivity,  $L_e$  is the effective pump length,  $U_B$  is the magnetic field speed defined in Equation 2-64,  $U_0$  is the mass averaged fluid speed  $U_0$ , and  $U_0$  is the height averaged magnetic field amplitude  $U_0$ . Note in Equation 2-64 that  $U_0$  is the average channel radius,  $U_0$  is the number of magnetic pole-pairs, and  $U_0$  is the frequency of the magnet array.

$$p_{\text{EM,max}} = \frac{1}{2}\sigma_{\text{f}}L_{\text{e}}(U_{\text{B}} - U_{\text{0}})B_{\text{0}}^{2}$$
Equation 2-63

$$U_{B} = \frac{\pi R_{avg}}{n_{mag}} f_{PMIP}$$
Equation 2-64

In deriving Equation 2-63, the pump was assumed to be infinitely wide. While this may be appropriate for an axisymmetric EMIP such as an ALIP, this is inappropriate for the PMIP geometry shown in Figure 2-15. Previous works have addressed this by solving the Induction Equation for a pump with a finite width  $2 \cdot b$  [15] [25] [42]. With this consideration, the new output pressure is now given in Equation 2-65.

$$p_{EM} = \frac{1}{2}\sigma_{f}L_{e}(U_{B} - U_{0}) B_{0}^{2} K_{at,(1,2)} = p_{EM,max} \cdot K_{at,(1,2)}$$
Equation 2-65

Note that Equation 2-65 is identical Equation 2-63 except for a new factor  $K_{at,(1,2)}$ . This coefficient describes the reduction, or attenuation, of the maximum EMIP output pressure caused by the finite width  $2 \cdot b$ . Two forms of the attenuation coefficient will be discussed. The first form was derived assuming a constant and uniform magnetic field amplitude  $B_0$  across the pump width shown in Equation 2-66.

$$B_{e,y}(x) = B_0$$
  
Equation 2-66

Solving the Induction Equation with this magnetic field form results in  $K_{at,1}$  shown in Equation 2-67 [25]. Note that  $k_0 = \pi/\tau_B$  is the fundamental wave number where  $\tau_B$  is the magnet pole-pitch. Also note that  $\lambda$  is an eigenvalue defined in Equation 2-68 where 1 is the imaginary unit. This eigenvalue appears in the solution of the Induction Equation. Inside this eigenvalue is the non-dimensional parameter  $Rm_f \cdot s_m$  defined in Equation 2-69 where  $\mu_f$  is the magnetic permeability of the fluid.  $Rm_f \cdot s_m$  is the effective magnetic Reynolds number that the fluid sees in the pump.

$$\begin{split} K_{at,1} &= \Re \left\{ \left(\frac{k_0}{\lambda}\right)^2 \cdot \left(1 - \frac{\tanh(\lambda b)}{\lambda b}\right) \right\} \\ &\quad \textit{Equation 2-67} \end{split}$$
 
$$\lambda^2 &= k_0^2 (1 + \iota \operatorname{Rm}_f \cdot s_m)$$
 
$$\quad \textit{Equation 2-68}$$
 
$$\operatorname{Rm}_f \cdot s_m &= \frac{\mu_f \sigma_f}{k_0} (U_B - U_0)$$
 
$$\quad \textit{Equation 2-69}$$

As noted earlier,  $K_{at,1}$  describes the reduction in output pressure due to the finite width  $2 \cdot b$  under a uniform magnetic field amplitude. Figure 2-16 plots  $K_{at,1}$  at  $Rm_f \cdot s_m = 0$  as a function of normalized pump half-

width b. Note that as the pump width becomes large,  $K_{at,1}$  approaches unity. Therefore, as b approaches infinity, Equation 2-65 approaches the ideal EMIP output defined in Equation 2-63.

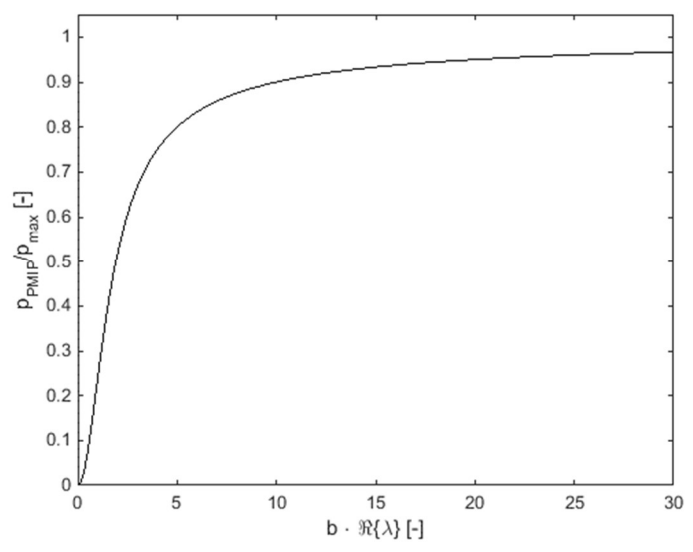


Figure 2-16: Normalized attenuation coefficient  $K_{at,1}$  at  $Rm_f \cdot s_m = 0$  as a function of normalized pump half-width b. As b approaches infinity,  $K_{at,1}$  approaches unity and the pressure output approaches the ideal EMIP pressure output.

In practice, the developed pressure is maximized only for large pump widths  $2 \cdot b$ . Values of  $K_{at,1}$  at  $Rm_f \cdot s_m = 0$  near unity are plotted in Figure 2-17. For large attenuation coefficient values, these pump widths are impractical for real PMIPs.

While the attenuation coefficient  $K_{at,1}$  reflects the finite pump width, it assumes a uniform magnetic field amplitude across the pump flow channel. However, previous work has shown that the magnetic field across the pump width will vary due to the finite dimensions of permanent magnet. This variation was found to follow the form of Equation 2-70 where  $\Gamma$  is an empirically derived shape-factor [15] [16].

$$B_{e,y}(x) = B_0 \cos(\Gamma \cdot x)$$
Equation 2-70

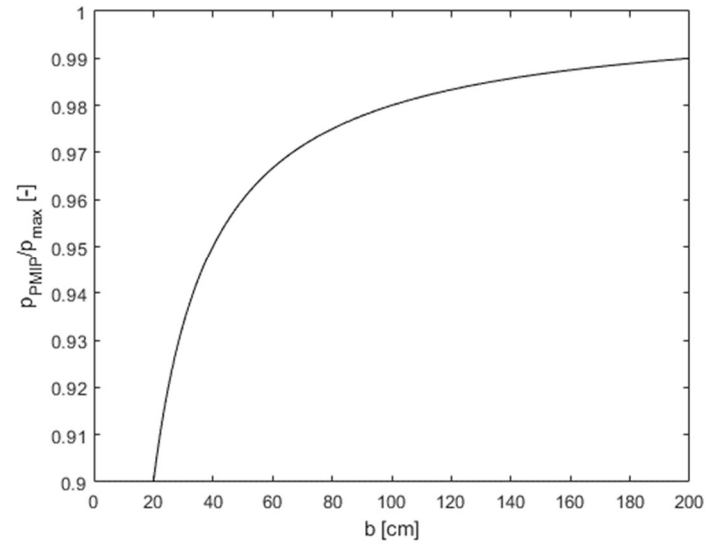


Figure 2-17: Near unity values of the normalized attenuation coefficient  $K_{at,1}$  at  $Rm_f \cdot s_m = 0$  as a function of the pump half-width b. For laboratory-scale, or medium-scale PMIPs, these pump half-widths are impractical.

Solving the Induction Equation with this magnetic field form results in  $K_{at,2}$  shown in Equation 2-71 [15] [42]. This new attenuation coefficient now accounts for both the finite width  $2 \cdot b$  and the non-uniform magnetic field amplitude described by the shape-factor  $\Gamma$ .

$$K_{at,2} = \Re \left\{ \frac{k_0^2}{\lambda^2 + \Gamma^2} \left( \frac{1}{2} + \frac{\sin(2\Gamma b)}{4\Gamma b} - \frac{\cos(\Gamma b)[\lambda \tanh(\lambda b)\cos(\Gamma b) + \Gamma \sin(\Gamma b)]}{b(\lambda^2 + \Gamma^2)} \right) \right\}$$
Equation 2-71

Note that the shape factor  $\Gamma$  describes the uniformity of the applied magnetic field across the duct width. Thus, a uniform magnetic field can be recovered as  $\Gamma$  approaches 0. Likewise, the attenuation coefficient  $K_{at,2}$  collapses to  $K_{at,1}$  as  $\Gamma$  approaches 0. Given a fixed pump width  $2 \cdot b$ , the shape-factor  $\Gamma$  will determine the additional reduction of ideal EMIP output pressure. Figure 2-18 shows that as the magnetic field amplitude approaches zero at  $\pm b$ , the output pressure can be reduced by half its value for a fixed half-width b. Therefore, the maximum PMIP output pressure can be significantly reduced by narrow flow channels with correspondingly narrow magnets.

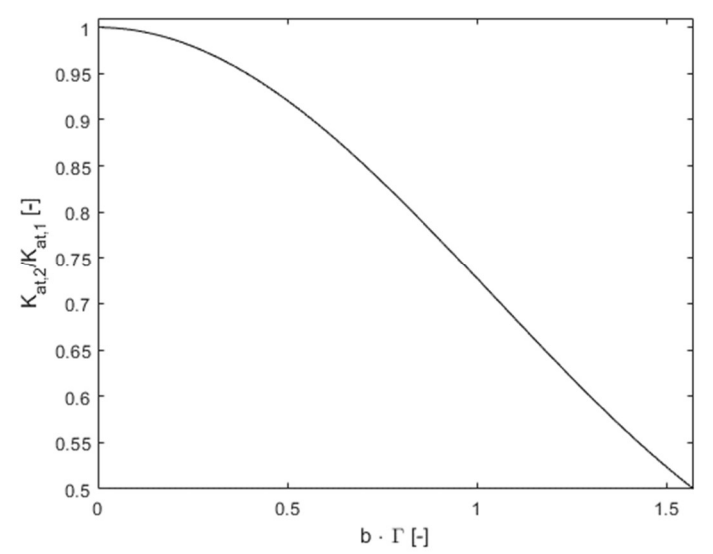


Figure 2-18: Normalized attenuation coefficient  $K_{at,2}$  at  $Rm_f \cdot s_m = 0$  as a function of normalized shape-factor  $\Gamma$  for a fixed pump half-width b. As  $\Gamma$  approaches zero,  $K_{at,2}$  will approach  $K_{at,1}$  evaluated at the given half-width b.

In addition to output pressure and flowrate, a pump's performance is also characterized by its efficiency. Typically, the useful power output is the pressure-flowrate power. Therefore, the efficiency can be defined as Equation 2-72 where p is the developed pump pressure, Q is the volumetric flowrate, and W<sub>in</sub> is the total pump input power.

$$\eta = \frac{p \cdot Q}{W_{in}}$$
Equation 2-72

The electrical input power can be broken down into several terms as described by Equation 2-73 [43]. The term  $p_{loss}Q$  is the power losses due to frictional losses in the pump and  $W_{loss}$  is the energy losses associated with driving the pump.

$$W_{in} = p_{EM}Q + p_{loss}Q + W_{R,f} + W_{R,c} + W_{loss}$$
  
Equation 2-73

The terms  $W_{R,f}$  and  $W_{R,c}$  are resistive heating losses in the fluid and pump conduit walls, respectively. These losses are described by Equation 2-74 where  $J_{f,c}$  is the induced current density and \* denotes the complex conjugate operator [36].

$$W_{R,(f,c)} = \iiint \frac{1}{2} \frac{\mathbf{J}_{f,c} \cdot \mathbf{J}_{f,c}^*}{\sigma_{f,c}} dV$$
Equation 2-74

Equation 2-74 can be evaluated analytically since the induced current density terms  $J_{f,c}$  were found in the solution of the Induction Equation. Using the same PMIP configuration discussed earlier, literature has shown that the resistive heating losses and in the fluid and walls take form the forms of Equation 2-75 and Equation 2-76 [14]. Note that that velocity of the wall is zero and therefore  $U_0 = 0$  when evaluating  $K_{at,(1,2)}$ .

$$W_{R,f} = \frac{1}{2} \sigma_f L_e (h_{ch} \cdot 2 \cdot b) (U_B - U_0)^2 B_0^2 K_{at,(1,2)}$$
Equation 2-75
$$W_{R,c} = \frac{1}{2} \sigma_c L_e (2 \cdot h_w 2 \cdot b) U_B^2 B_0^2 K_{at,(1,2)}$$

For an ideal EMIP, the efficiency is calculated by neglecting frictional pressure losses, resistive heating losses in the pump walls, and other losses as shown in Equation 2-77. Under these conditions, the efficiency is linear with the mean-slip as described by Equation 2-78 [36]. Note that the mean-slip is defined in Equation 2-79 as the normalized difference between the magnetic velocity and the mass-averaged fluid velocity.

$$\eta_{EM,ideal} = \frac{p_{EM}Q}{p_{EM}Q + W_{R,f}}$$
 Equation 2-77

$$\eta_{ideal} = 1 - s_m$$
Equation 2-78

$$s_{\rm m} = \frac{U_{\rm B} - U_{\rm 0}}{U_{\rm B}}$$
Equation 2-79

However, for real EMIPs operating at low slips, much of the energy is dissipated as resistive heating in the pump walls. Therefore, at low slips it is expected that the efficiency will decrease. This reality is reflected in the new theoretical efficiency definition in Equation 2-80.

$$\eta_{EM} = \frac{p_{EM}Q}{p_{EM}Q + W_{R,f} + W_{R,c}}$$
 Equation 2-80

By considering resistive heating losses in the pump walls, a PMIP's efficiency will decrease significantly at low slips. Figure 2-19 plots the ideal EMIP efficiency with the theoretical PMIP efficiency as a function of mean-slip. Note  $\Gamma = \pi/2$  was used when evaluating  $K_{at,2}$ . For the experimental PMIP, the maximum theoretical efficiency ranges between 20% and 25% in a mean-slip range of 0.25 to 0.35.

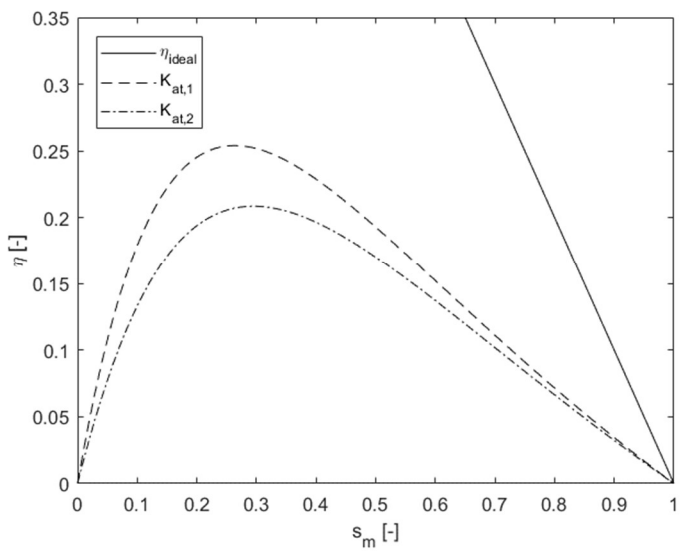


Figure 2-19: Ideal EMIP efficiency plotted with the analytically calculated PMIP efficiency as a function of meanslip. Note that when evaluating  $K_{at,2}$  a magnetic field shape-factor value of  $\Gamma = \pi/2$  was used.

#### 2.3.3 Effects of the Finite Width

The finite width effect is a result of current continuity [27] [26]. Qualitatively, this is shown in Figure 2-20. Since current must be conserved, the induced currents form continuous loops in the fluid. However, since the channel is not axisymmetric, the current loops form in the x-z plane. Note that for a pumping direction in the positive z-direction, only the x-component of the induced current loop produces a useful force. Conversely, the z-component produces a force which is directed inwards and is of no use for pumping. In the ideal case where the duct is infinitely wide, the current loops effectively only have an x-component since they reconnect at infinity.

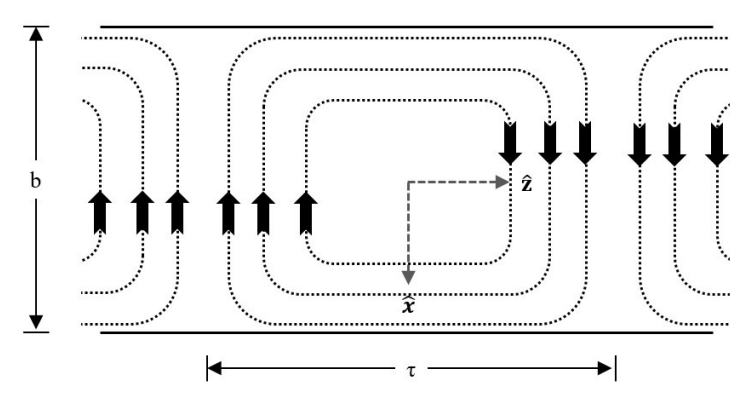


Figure 2-20: Qualitative distribution of currents in a finite width duct with no electrically conducting walls.

In the previous section, the analytical solution neglected the conduit walls. Therefore, Figure 2-20 shows that the induced current is solely contained in the fluid. However, this is not generally true. Figure 2-21 shows that some induced current may flow into the conduit walls. Thus, the conduit walls may be useful in maximizing the induced current's x-component and satisfying current continuity.

In literature, this effect has been studied for MHD flows confined to a square channel under the influence of a uniform and stationary magnetic field. Figure 2-22 presents the qualitative results of the analytical solution [44]. In the case where the A-A walls have infinite conductivity, the currents tend to pass into the walls. In the other extreme, where the A-A walls have zero conductivity, the currents will bypass the walls

and connect in the fluid. Therefore, the wall conductivity has an important role in determining the current distribution in a square channel pump.

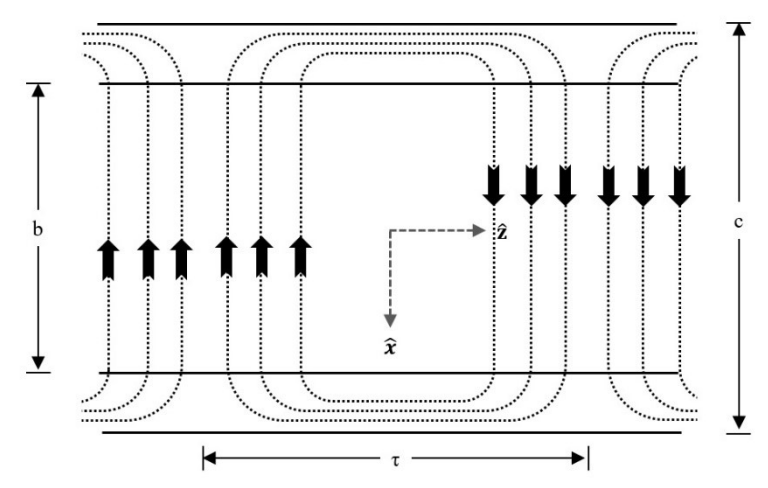


Figure 2-21: Qualitative distribution of currents in a finite width duct with electrically conducting walls.

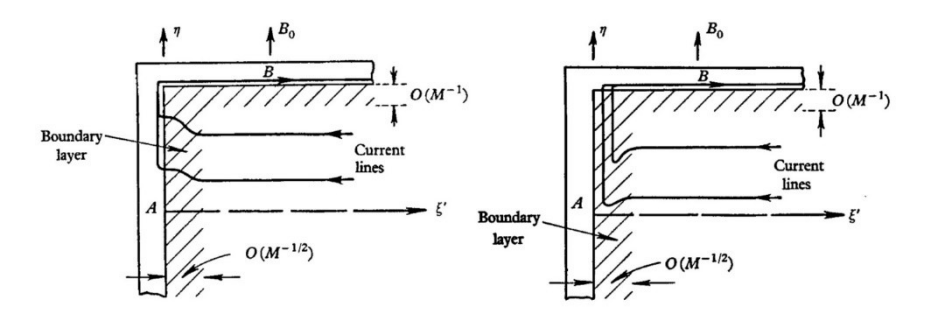


Figure 2-22: Qualitative current distribution in a rectangular under the influence of a stationary and uniform magnetic field [44]. On the left is the case where the side walls have a finite conductivity. On the right is the case where the side walls have zero conductivity.

However, as noted in the EMIP energy balance from, the conduit currents in Equation 2-81 will cause resistive heating. Thus, the increase in performance due to more uniform currents may be negated due to the increase resistive losses, decreasing the pump efficiency. No analytic work could be found which investigates this optimization.

$$W_{R,c} = \iiint \frac{J_c \cdot J_c^*}{2\sigma_c} dV$$
Equation 2-81

Figure 2-23 shows that wall effects have been modeled in FLIPs numerically. Note that while FLIPs use polyphase coils instead of permanent magnets, the pump conductivity is like a PMIP. Therefore, the results will provide some insight into the finite width effects of a PMIP. In this study, a parameter called  $\varepsilon$ , defined as the ratio of channel wall to fluid conductivity  $\sigma_c/\sigma_f$  was swept over a range of values assuming uniform and non-uniform velocity profiles.

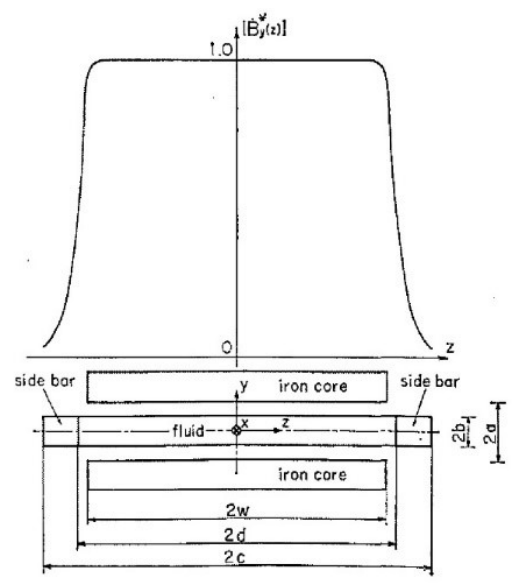


Figure 2-23: Geometry used in a FLIP numerical model. While the results do not directly represent a PMIP, the channel geometry is similar and the results do provide insight into the finite width effects of a PMIP [45].

Figure 2-24 shows the effect of the conductivity ratio  $\varepsilon$  on pump performance [45]. For increasing  $\varepsilon$ , the performance of the pump is predicted to increase. Furthermore, one can see that the efficiency of the pump is predicted to increase with increasing wall conductivity ratio. This suggests that the side walls may be promoting the currents to reconnect in the walls as was shown in the analytical investigations. However, a subtly should be noted. Observe that the magnetic flux in the sidewalls is small in magnitude. Thus, the induced currents in the walls and their associated resistive heating will also be small.

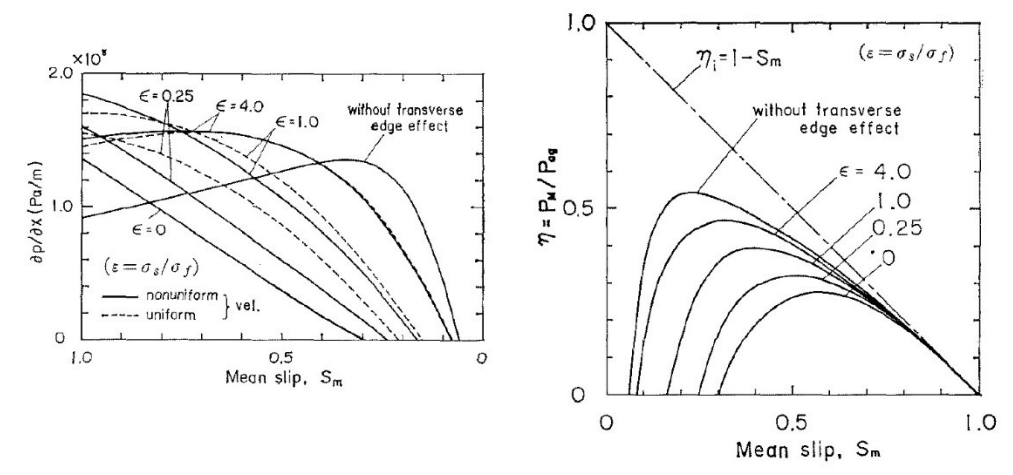


Figure 2-24: Geometry used in a FLIP numerical model. While the results do not directly represent a PMIP, the channel geometry is similar and the results do provide insight into the finite width effects of a PMIP [45].

Very little experimental literature could be found investigating finite width effects in PMIPs. A single study exists which investigates the impact of copper side bars on a drum-type PMIP using GaInSn [46]. Figure 2-25 shows a sketch of the experimental setup. Four configurations were studied to investigate the impact of a ferromagnetic yoke and copper side bar combinations.

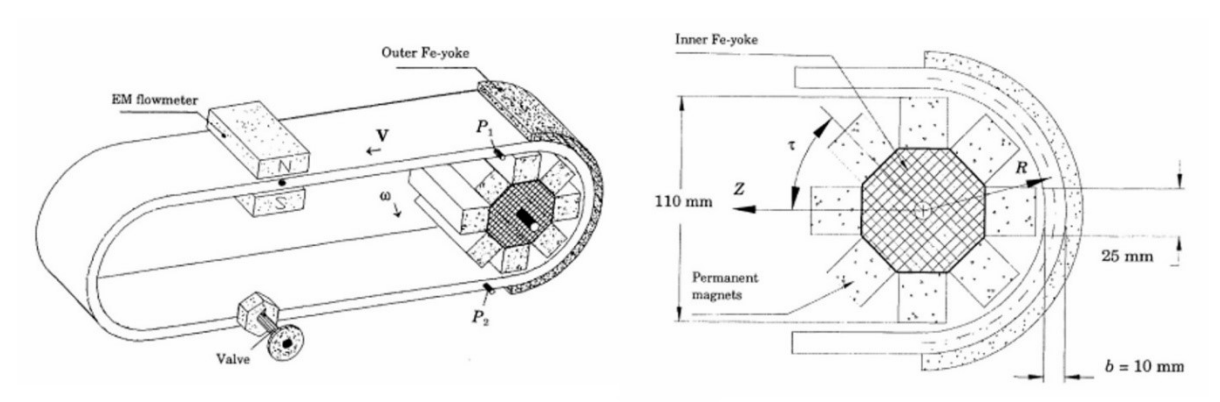


Figure 2-25: Experimental setup of a Drum-Type PMIP used to pump GaInSn. Four configurations were used to study the impact of outer ferrous yokes and copper side bars [46].

Figure 2-26 shows that the presence of side copper bars increased the maximum developed pressure regardless of the ferromagnetic yoke [46]. Note that the electrical conductivity ratio of copper to GaInSn at 20 °C is approximately 0.17. Assuming the original walls were made of a material with zero conductivity, this work seems to experimentally confirm that higher conductivity side walls improve PMIP performance.

However, it should be noted that the author was not clear on the materials of the walls or whether the bars were simply affixed to an existing wall of finite conductivity.

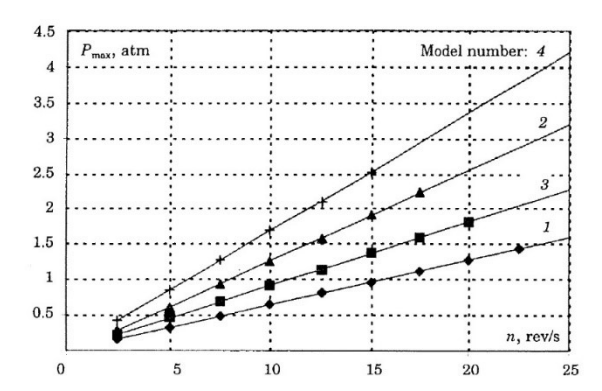


Figure 2-26: Experimental pressure output of the Drum-Type PMIP with, 1 no ferromagnetic yoke or copper side bars, 2 with a ferromagnetic yoke and no copper side bars, 3 no ferromagnetic yoke and with copper side bars, and 4 with a ferromagnetic yoke and copper side bars [46].

## 2.3.4 Summary

In total, this literature review presented the fundamental PMIP theory which can be used to estimate the output pressure and efficiency performance for a finite width pump. Additionally, this review identified the Finite Width Effect as the main PMIP Edge Effect. This effect is a direct result of current continuity. The resulting induced current loops will have a component which produces no useful pumping force. Consequently, the PMIP performance is reduced relative to the ideal. This effect is exacerbated as the width of the pump becomes small relative to the current loops. Additionally, another factor must be considered for PMIPs. Since PMIPs use finite-width permanent magnets, the flux distribution across the pump-width is non-uniform. Therefore, the non-uniform flux will result in reduced pump performance relative to the ideal.

# 3. ALIP PERFORMANCE CHARACTERISTICS AND THE IMPACT OF THE FINITE LENGTH EDGE EFFECT

## 3.1 ALIP SPECIFICATIONS

A custom ALIP was designed and built by CMI-Novacast for studying coil shifting and coil grading. Figure 3-1 shows the experimental pump installed in the system. Table 3-1 provides some nominal operating conditions while Table 3-2 provides some relevant geometric information.

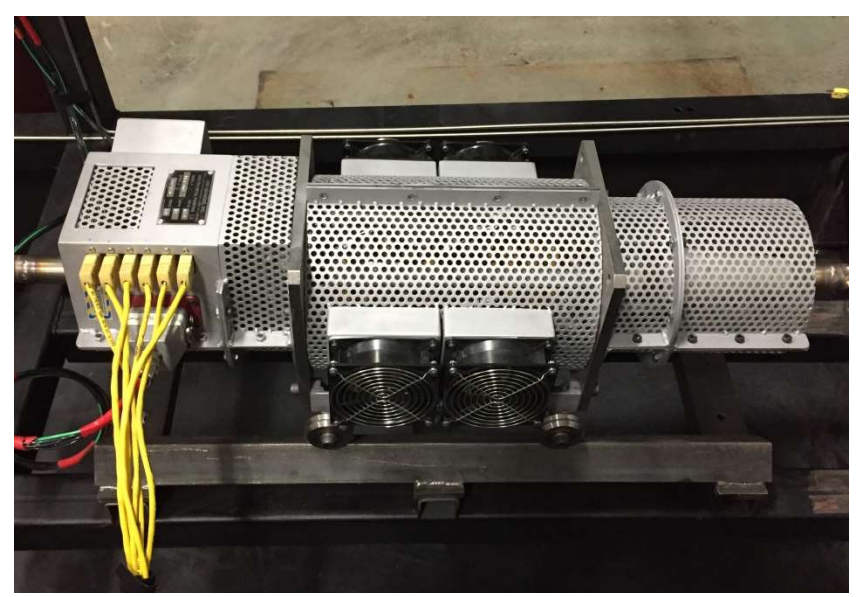


Figure 3-1: Custom designed and built CMI-Novacast model LA125 ALIP used in experimental testing.

Table 3-1: Rated conditions for CMI-Novacast's LA125 ALIP.

Property	Value	Unit
Maximum Voltage	480	$V_{rms}$
Maximum Current	15	$A_{rms}$
Frequency	120	Hz
Maximum Temperature	600	${}^{\circ}C$
Maximum System Pressure	15	bar

Property	Value	Unit
Number of Coils	12	-
Poles	4	-
Stator Length	300	mm
Channel Width	3.9	mm
Mean Channel Radius	19.4	mm

Table 3-2: Some relevant geometric properties for CMI-Novacast's LA125 ALIP.

The experimental ALIP has two modifications compared to a standard model. The first modification accommodates shifting of the outer coils and outer ferromagnetic core by up to 75 mm towards the inlet or outlet of the pump. This corresponds to roughly a single pole-pitch in either direction. Figure 3-2 shows a schematic of the three coil shifting configurations tested. The centered, 75 mm entrance-shifted, and 75 mm exit-shifted are denoted as Configuration 100, Configuration 200, and Configuration 300 respectively.

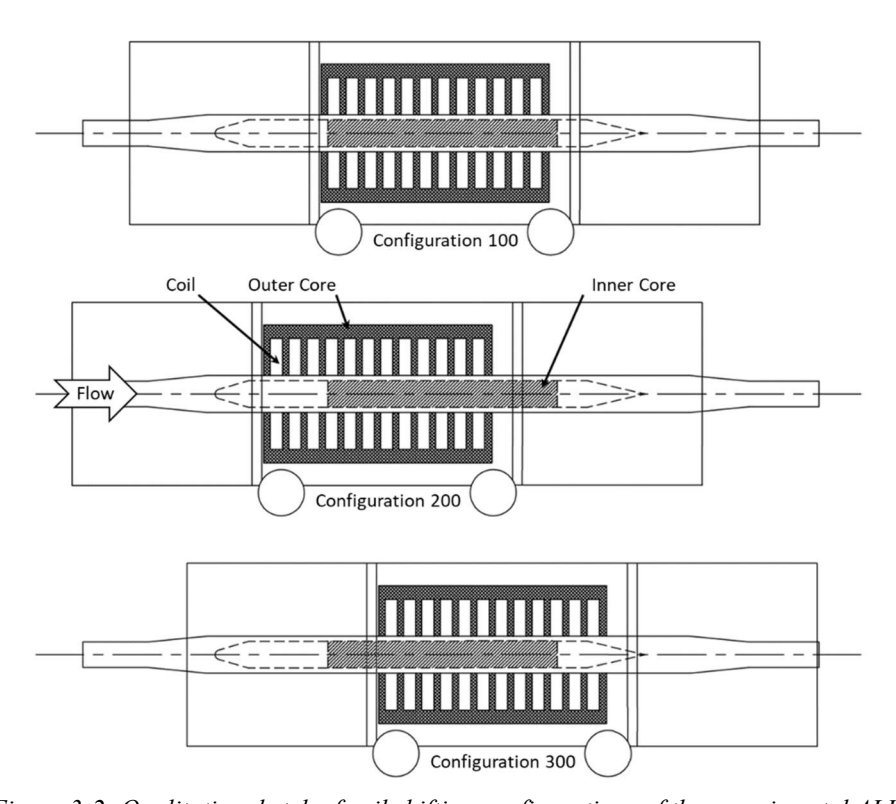


Figure 3-2: Qualitative sketch of coil shifting configurations of the experimental ALIP.

The second modification accommodates coil grading with multi-tapped coils. Figure 3-3 shows a twodimensional sketch of a modified coil which has four taps are located on the 1<sup>st</sup>, 20<sup>th</sup>, 31<sup>st</sup>, or 80<sup>th</sup> turn. Figure 3-4 presents a cut-away of the ALIP is shown which shows the position and coil number in the pump. Finally, Table 3-3 provides a summary of each configuration which will be tested in this work.

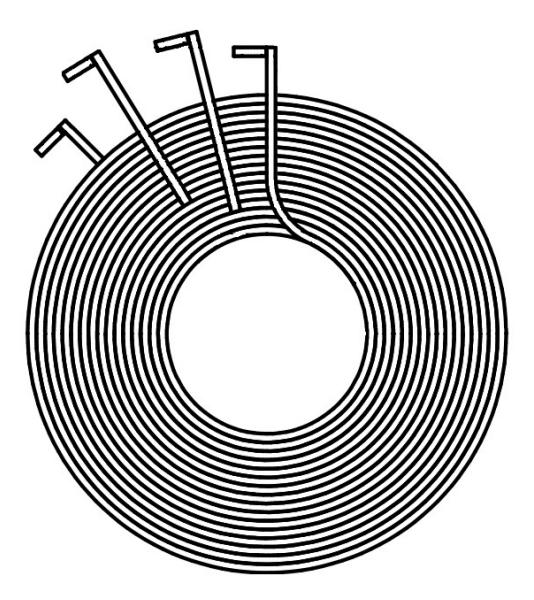


Figure 3-3: Sketch of the tapped coils installed in the first three and last three coil locations. Each of the six coils have taps at the  $1^{st}$ ,  $20^{th}$ ,  $31^{st}$ , or  $80^{th}$  turn.

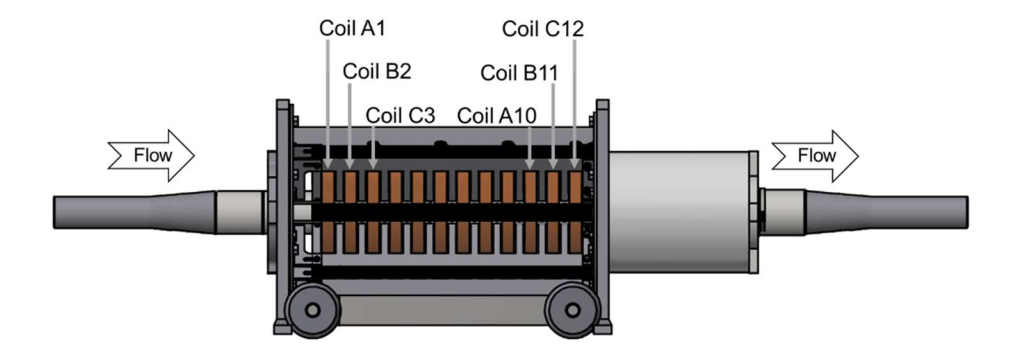


Figure 3-4: Cut away of the experimental ALIP showing each of the 12 polyphase coils in the pump. Note that the first three coils and last three coils are tapped.

Table 3-3: Summary of the setup of each configuration studied in this work.

Configuration	Chifting	Coil Taps						
Configuration	Shifting	AI	<i>B2</i>	<i>C3</i>	A4-C9	A10	B11	C12
100	None			A	ll Coils 1-	80		
101	None	61-80	50-80	1-50	1-80	1-50	50-80	61-80
102	None	50-61	61-80	50-80	1-80	50-80	61-80	50-61
200	75 mm-Inlet				1-80			
300	75mm-Outlet			A	ll Coils 1-	80		

## 3.2 EXPERIMENTAL SETUP

# 3.2.1 Facility Overview

ALIP performance was evaluated using a high-temperature liquid-sodium test loop called the ALIP Test Facility. Figure 3-5 presents both a 2D-schematic and overview of the ALIP Test Facility. This system is designed to operate at a maximum temperature of 600 °C and is fully instrumented to qualify pump performance using a calibrated Electromagnetic Flowmeter (EMFM), differential pressure transducers, and a counter-flow air-cooled heat exchanger.

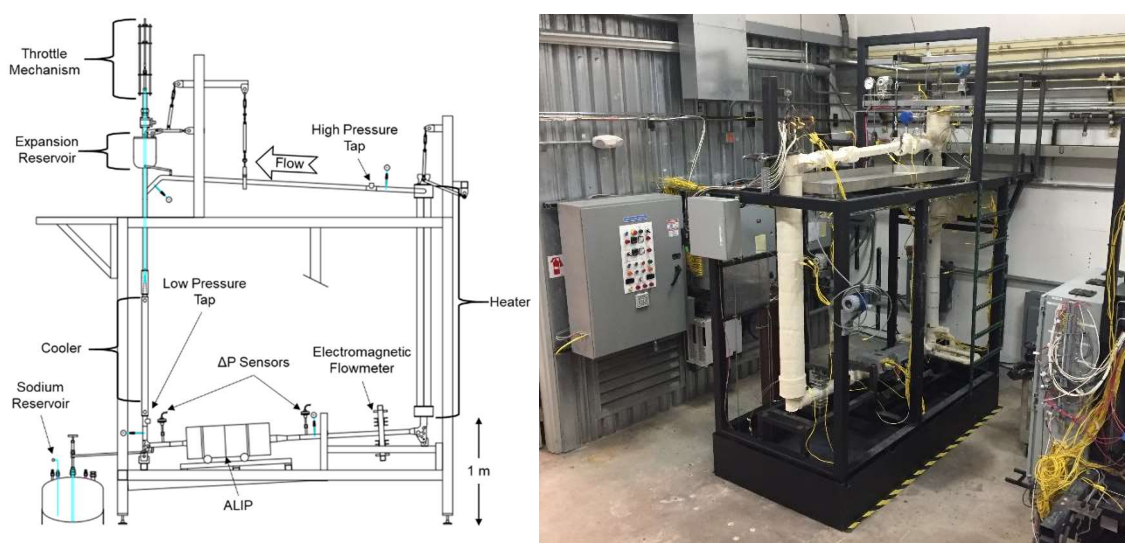


Figure 3-5: Schematic of the ALIP Test Facility used in the characterization of the finite length effect on an Annular Linear Induction Pump.

## 3.2.2 Magnetic Field Measurement

Prior to testing, the axial distribution of the ALIP's radial-component magnetic field was characterized using a calibrated air-cored pick-up coil. Figure 3-6 shows one of the pick-up coils used in this work while Table 3-4 show some specifications of these coils.

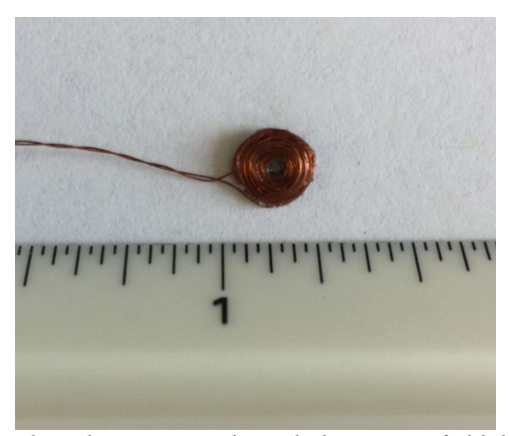


Figure 3-6: Air-cored pick-up coil used to measure the radial magnetic field distribution in the ALIP channel.

Table 3-4: Relevant dimensions of the air-cored pick-up coil in Figure 3-6.

Property	Value	Units
Inner Diameter	1.3	mm
Outer Diameter	5	mm
Height	0.635	mm
Number of Turns	150	-
Wire Gauge (AWG)	38	-
Nominal Wire Diameter	0.127	mm

An air-cored pick-up coil operates on the principle of Faraday's law in Equation 3-1 where  $V_{coil}$  is the included voltage, n is the number of turns,  $\partial B/\partial t$  is the time derivative of the magnetic field B, and  $A_{eff}$  is the effective area in Equation 3-2 where  $L_i$  and  $L_o$  are the inner and outer diameter of the coil respectively.

$$V_{coil} = -nA_{eff} \frac{\partial B}{\partial t}$$
Equation 3-1

$$A_{eff} = \frac{\pi}{16} (L_i + L_o)^2$$
 Equation 3-2

For simplicity, integrating the induced voltage signal is avoided. Instead, peak voltages  $V_{pk}$  were correlated to peak magnetic field amplitudes  $B_{pk}$  by Equation 3-3 where  $f_B$  is the magnetic field frequency. The constant  $C_1$  is the correlation coefficient found by plotting  $V_{pk}/nA_{eff}f_B$  against  $B_{pk}$ .

$$V_{pk} = C_1 \cdot nA_{eff}f_B \cdot B_{pk}$$
Equation 3-3

The constant C<sub>1</sub> was found under the known magnetic field amplitude and frequency. Peak magnetic field amplitudes were measured using a Hall-Sensor at frequencies of 18 Hz, 36 Hz, 54 Hz, and 72 Hz. Then, the signal's fundamental frequency component was extracted using a Fast Fourier Transform (FFT). Peak values of this frequency component were then normalized by nA<sub>eff</sub>f<sub>B</sub>. Using the model in Equation 3-4, a linear regression analysis was used to find calibration constant C<sub>1</sub>. Figure 3-7 plots the normalized peak signals as a function of peak magnetic field amplitude while Table 3-5 presents the resulting correlation coefficients, their standard errors, and correlation coefficient. Figure 3-8 presents the calibration residuals from the linear regression analysis. For simplicity, the pick-up coil measurement error is estimated from the calibration residuals as 5% the measured value.

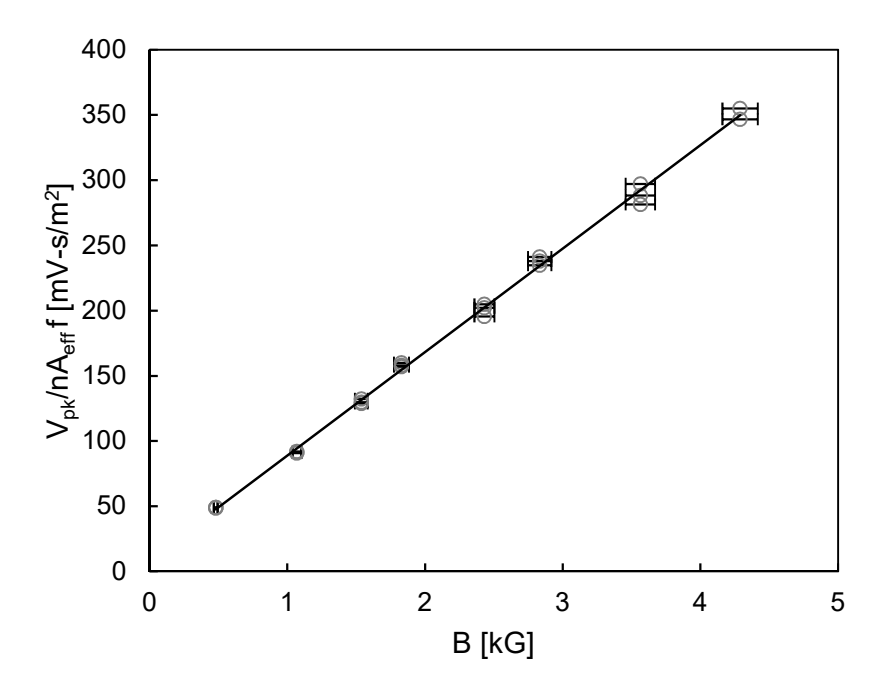


Figure 3-7: Calibration curve for the pick-up coil in Figure 3-6 used to measure the radial magnetic field component in the ALIP channel.

$$y = C_1 \cdot x + C_0$$
Equation 3-4

Coefficient	Value	Standard Error	Units	
$C_0$	9.6	1.96	$mV$ - $s/m^2$	
$C_1$	79.3	0.80	$mV$ - $s/kG$ - $m^2$	

0.9989

Table 3-5: Pick-up coil correlation coefficients, their standard errors, and correlation coefficient.

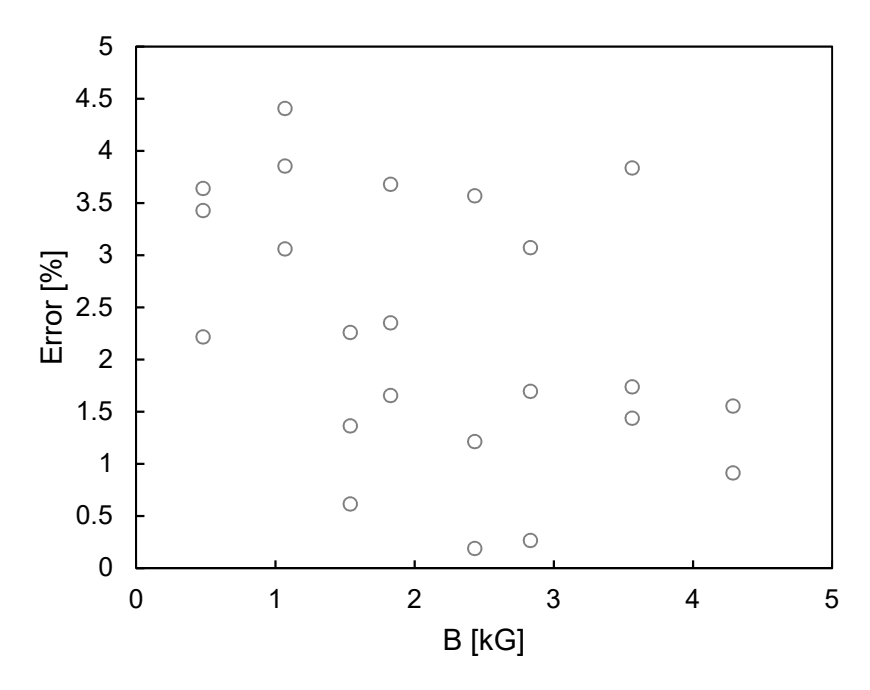


Figure 3-8: Pick-up coil calibration residuals. For simplicity, the measurement error was taken as 5% the measured value. Note that the calibration can be improved with more data points which would allow for a more sophisticated error analysis.

Note that the calibration above can be improved with more data points. Due to the small number of points, the standard error of the intercept is large. Consequently, the total calibration error following the Guide to the Expression of Uncertainty in Measurement will also be large. Therefore, the magnetic field measured by the pick-up coil is qualitative and the reader is cautioned against taking quantitative data from the resulting figures.

### 3.2.3 Flowrate Measurement

Primary flowrate measurements were made with a calibrated Electromagnetic Flowmeter (EMFM). Figure 4-3 presents the ALIP-EMFM flowmeter used in this work. An EMFM measures flowrate by measuring

the voltage induced by an electrically conductive fluid passing through a stationary magnetic field. Note that a magnetic field oriented perpendicular to the fluid velocity will induce a mutually orthogonal voltage that can be measured by a pair of externally mounted electrodes. Table 4-3 lists the specifications of the ALIP-EMFM used in this work.

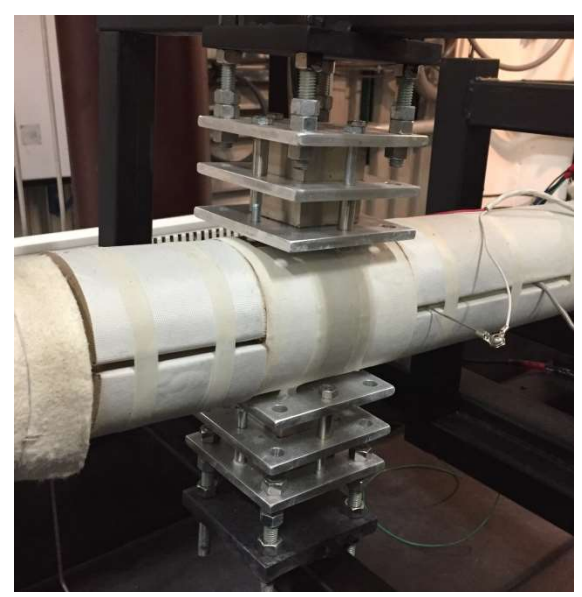


Figure 3-9: Photo of the ALIP-EMFM used for primary flowrate measurements.

Table 3-6: Additional specifications of the ALIP- EMFM.

Tuote 5 6. Hadittonai specifications of the HEII EMI M.					
Quantity	Value	Units			
Туре	NdFeB	-			
Grade	N42	-			
Dimensions	$5 \times 5 \times 5$	cm			
Spacing	11.7	cm			
$d_{\mathbf{i}}$	2.66	cm			
$D_{o}$	3.34	cm			
Material	316/316L	-			

Measured voltages  $\Delta V_{EMFM}$  are related to volumetric flowrates Q velocity by Equation 3-5 where  $K_1$ ,  $K_2$ ,  $K_3$  are correction factors, and  $B_0$  is the magnetic field magnitude across the inner channel diameter  $d_i$  [47].

$$\Delta V_{EMFM} = K_1 K_2 K_3 B_0 \frac{4}{\pi} \frac{Q}{d_i}$$
Equation 3-5

Factor  $K_1$  in Equation 3-5 corrects for wall-shunting effects. Equation 3-6 defines  $K_1$  where  $d_i$  and  $D_o$  are the channel inner and outer diameters respectively, while  $\rho_f$  and  $\rho_{ch}$  are the fluid and channel electrical resistivity respectively [48] [49] [50]. Note that in this work, the wall temperature is assumed to be the same as the sodium temperature.

$$K_{1} = \frac{\frac{2d_{i}}{D_{o}}}{1 + \left(\frac{d_{i}}{D_{o}}\right)^{2} + \frac{\rho_{f}(T_{Na})}{\rho_{ch}(T_{Na})} \left(1 - \left(\frac{d_{i}}{D_{o}}\right)^{2}\right)}$$
Equation 3-6

Correction factor  $K_2$  corrects for end-shunting at the inlet and outlet of the flowmeter where the magnetic field is weakest. Equation 3-7 defines the  $K_2$  where  $L_{FM}$  is the flowmeter length and  $d_i$  is the inner diameter of the conduit [51] [52] [53] [54]. Note that this form is only valid for  $1 \le \frac{L_{FM}}{d_i} \le 3.5$ .

$$K_{2} = -0.0047 \left(\frac{L_{FM}}{d_{i}}\right)^{4} + 0.0647 \left(\frac{L_{FM}}{d_{i}}\right)^{3} - 0.3342 \left(\frac{L_{FM}}{d_{i}}\right)^{2} + 0.7729 \left(\frac{L_{FM}}{d_{i}}\right) + 0.3172$$

$$Equation 3-7$$

Lastly, correction factor  $K_3$  corrects for magnet temperature effects. Equation 3-8 defines the  $K_3$  where  $T_{mag}$  is the magnet temperature in °C [55]. The magnet temperature is assumed to be constant at 20 °C since the insulation is assumed to protect the EMFM from excessive temperatures.

$$K_3 = e^{-(1.1 \times 10^{-3})(T_{\text{mag}} - 20)}$$
Equation 3-8

In theory, these three factors accurately correct the measured induced voltage. In practice, the flowmeter must be experimentally calibrated to account for non-ideal effects. Therefore, the experimental ALIP-EMFM was calibrated against the Foxboro M83 vortex shedding flowmeter. As specified by the manufacturer, the Vortex Shedding flowmeter accuracy is Reynolds number dependent. Table 3-7 reports

these ranges in flowrates in a 2.66 cm diameter conduit with sodium properties evaluating using Fink [2] at 200 °C.

Table 3-7: Reported accuracy of the Vortex Shedding Flowmeter. Flowrates were calculated in a 2.66 cm diameter conduit with sodium properties evaluated using Fink [2] at 200 °C.

Reynolds Number	Flowrate	Accuracy		
	m³/hr	%		
20,000-30,000	0.78-1.16	1		
30,000-200,000	1.16-7.75	0.5		
>200,000	>7.75	1		

Prior to calibration, the ALIP-EMFM walls were wetted with sodium for approximately 20 hours. Sodium has been noted to have poor initial wetting characteristics of stainless steel [56]. This will increase the resistance across the EMFM measurement leads and decrease the measured voltage. However, over time the sodium will 'wet' the conduit walls and reach a steady state. To quantify this behavior, the vortex shedding flowmeter signal was compared to the ALIP-EMFM signal over the course of 20 hours in contact with sodium at various temperatures. Figure 3-10 shows that the initial wetting occurred in the first two hours. After roughly eight hours, the stainless steel was deemed to be fully wetted by sodium.

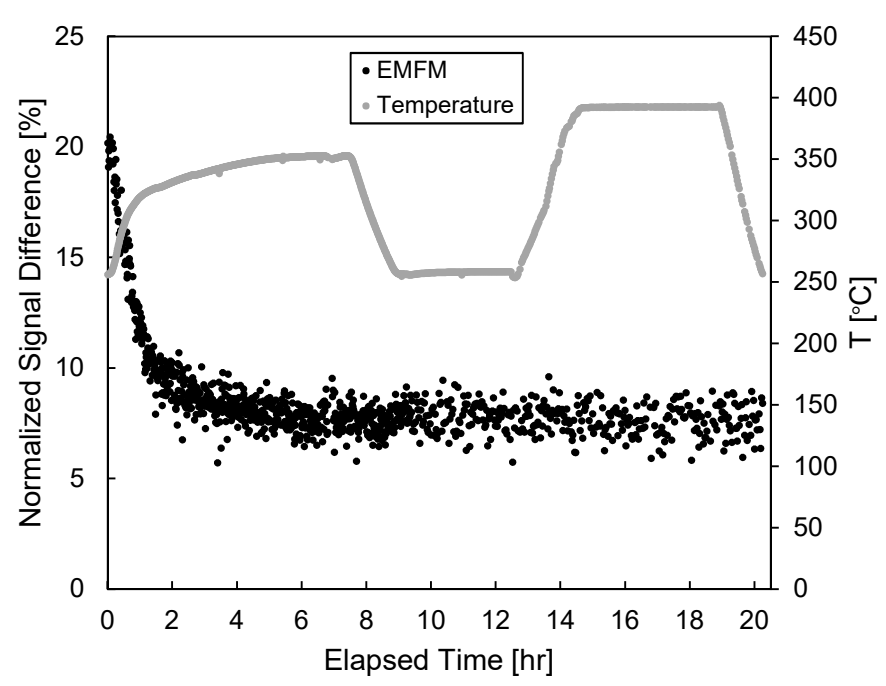


Figure 3-10: Normalized signal difference between the reference vortex shedding flowmeter and ALIP-EMFM over a period of 20 hours. Note that the initial wetting occurred over the first two hours.

After wetting, the ALIP-EMFM was calibrated against the vortex shedding flowmeter. Figure 4-4 plots the predicted flowrates as a function of reference flowrates. Using the model in Equation 4-1, correlation coefficients  $A_0$  and  $A_1$  were found using a linear regression analysis. Table 4-4 presents the calculated coefficients, their standard errors, and correlation coefficient.

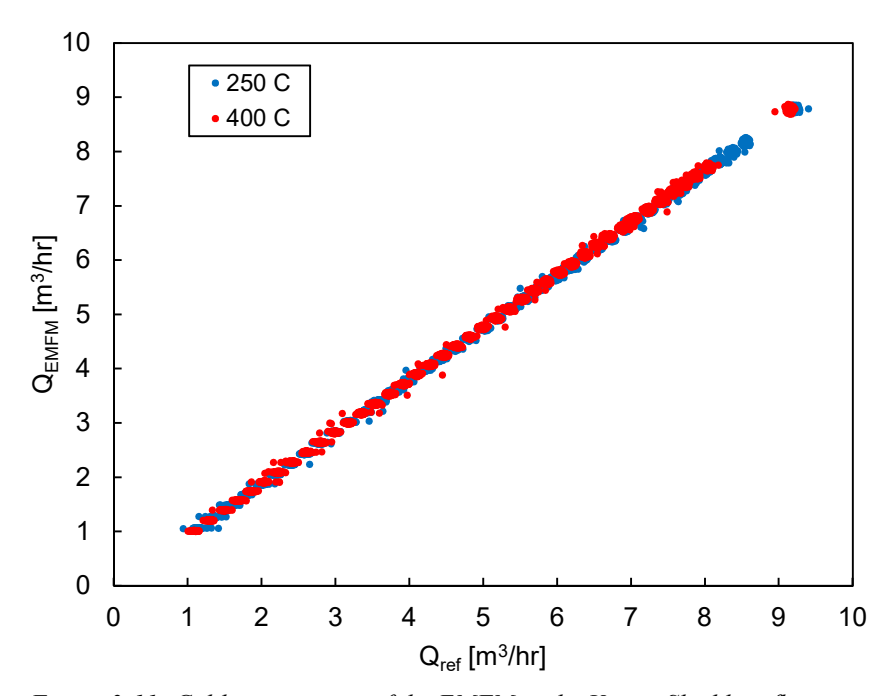


Figure 3-11: Calibration curve of the EMFM to the Vortex Shedding flowmeter.

$$\begin{aligned} \mathbf{Q}_{\mathrm{EMFM}} &= \mathbf{A}_0 + \mathbf{A}_1 \cdot \mathbf{Q}_{\mathrm{ref}} \\ & \textit{Equation 3-9} \end{aligned}$$

Table 3-8: ALIP-EMFM coefficients, their associated standard errors, and correlation coefficient.

Quantity	Value	Units
$A_0$	-0.0471	m³/hr
$A_1$	0.9623	-
$S.E.(A_0)$	0.0005	$m^3/hr$
$S.E.(A_1)$	0.0001	-
r	1	-

A total calibration error was calculated in two parts. First, an EMFM measurement error was analytically estimated by propagating the error in Table 3-9 through Equation 3-5 using the general law of propagation of uncertainty. This defined an EMFM measurement error as a function of flowrate. Secondly, a total

calibration error was calculated following the Guide to the Expression of Uncertainty in Measurement [57]. This approach combined the estimated EMFM measurement error with the standard errors of the coefficients  $A_0$  and  $A_1$  using the same general law of propagation of uncertainty mentioned earlier. Figure 3-12 plots the total estimated calibration error and the resulting calibration residuals. Note that the estimated instrument error follows a similar trend and magnitude as the residuals. As a conservative estimate, the accuracy of the ALIP-EMFM is broken into two ranges; in the range of  $1 \text{ m}^3/\text{hr} \leq Q < 2.5 \text{ m}^3/\text{hr}$  the accuracy is reported as 1.5% the measured value while in the range of  $2.5 \text{ m}^3/\text{hr} \leq Q < 9.5 \text{ m}^3/\text{hr}$  the accuracy is reported at 0.75% the measured value.

Table 3-9: Estimated uncertaintities of the primary ALIP-EMFM measurements

Quantity	Value	Units
$d_i$	0.0508	mm
$D_{o}$	0.0508	mm
$T_{mag}$	1	$^{\circ}\mathrm{C}$
$T_{Na}$	0.5	$^{\circ}\mathrm{C}$
$\Delta V_{EMFM}$	$\sqrt{(0.001 * \Delta V_{EMFM})^2 + (15)^2}$	$\mu - V$

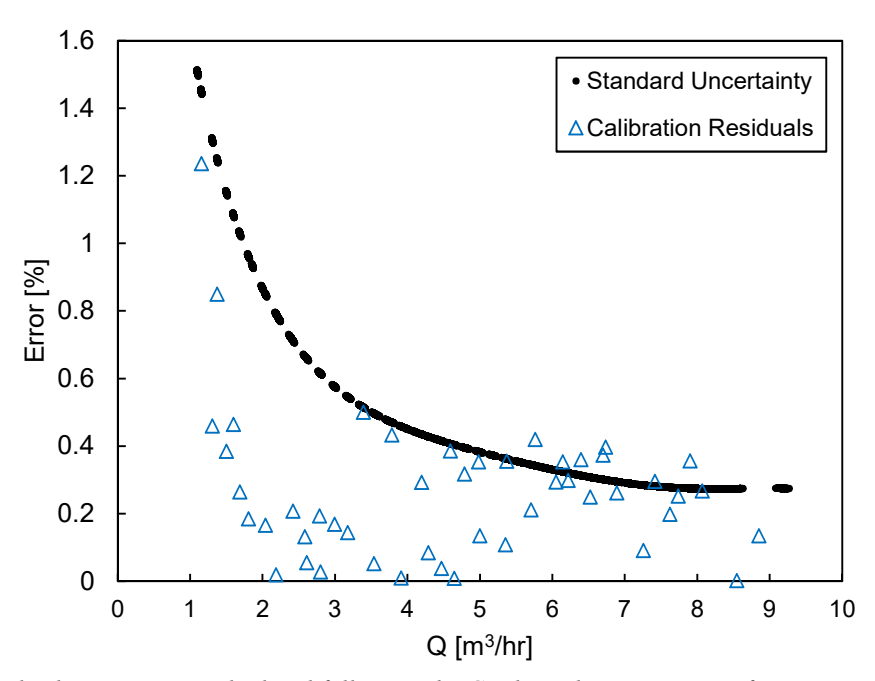


Figure 3-12: Standard Uncertainty calculated following the Guide to the Expression of Uncertainty in Measurement standard compared to the calculated calibration residuals. As a conservative estimate, the accuracy of the ALIP-EMFM is broken into two ranges; in the range of  $1\,\mathrm{m}^3/\mathrm{hr} \le Q < 2.5\,\mathrm{m}^3/\mathrm{hr}$  the accuracy is reported as 1.5% the measured value while in the range of  $2.5\,\mathrm{m}^3/\mathrm{hr} \le Q < 9.5\,\mathrm{m}^3/\mathrm{hr}$  the accuracy is reported at 0.75% the measured value.

### 3.2.4 Pressure Measurement

ALIP pressure output  $\Delta p$  and channel frictional pressure losses  $p_{loss,chan}$  were characterized prior to pump testing. Figure 3-13 shows the location of both the  $\Delta p$  and the  $p_{loss,chan}$  measurements. Note that the two taps were at different locations due to space limitations. These additional frictional losses are ignored in the following analysis as they were estimated to be small.

ALIP  $\Delta p$  was measured in sodium using a Rosemont 3051T differential pressure transducers fitted with a pair of silicon oil-filled thermal stand-offs. Figure 3-13 shows the location of the  $\Delta p$  taps on the ALIP conduit. Note that prior to testing, the sensors were initially zeroed at a zero-flowrate condition. Over the course of testing, these zero-flowrate readings were recorded and found to drift by 70 Pa. However, the Rosemont 3051T pressure transducer used in this work has a reported accuracy of roughly 766 Pa. Since the drifts are within the reported accuracy, the reported sensor accuracy was used in the uncertainty analysis.

Channel frictional pressure losses  $p_{loss,chan}$  were measured in water using a Siemens SitransP pressure transducer with a measurement span of 16 mbar to 1600 mbar. Two effects impact the accuracy of pressure measurements. Equation 3-10 defines a linear characteristic where r is the ratio between the maximum span and the set span. The total span of the instrument is 1600 mbar and the set span used for the majority of testing was 675 mbar resulting in an r value of 2.37.

$$\sigma_{\Delta p, lin} = 0.001 \text{ for } r \le 10$$
Equation 3-10

A temperature effect must also be considered which is given in Equation 3-11. The total accuracy of the differential pressure measurements can be found using Equation 3-12. For a total span of 1600 mbar and a set span of 675 mbar, the total accuracy of the pressure measurement was found to be approximately 0.45% of the differential pressure measurement.

$$\sigma_{\Delta p,T} = 0.001 \cdot r + 0.002$$
Equation 3-11

$$\sigma_{\Delta p} = \sqrt{\sigma_{\Delta p, lin}^2 + \sigma_{\Delta p, T}^2}$$
Equation 3-12

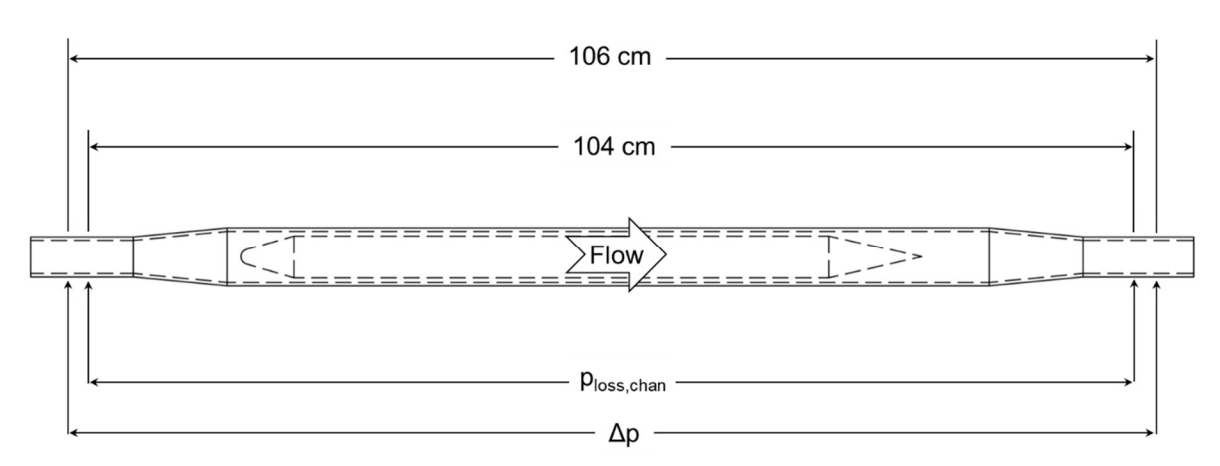


Figure 3-13: Location of differential pressure measurement for the channel frictional losses  $p_{loss,chan}$  and developed pressure  $\Delta p$ . Note that any height-induced pressures were recorded at several zero-flowrate conditions and subsequently offset from the final pressure measurements. Due to space constraints,  $p_{loss,chan}$  was measured at a different location than  $\Delta p$ .

#### 3.2.5 Power Measurement

ALIP input power was measured using a Yokogawa WT1600 power analyzer. Note that the source for the ALIP is 3-phase delta configured  $480 \, V_{rms}$  with a wild-leg connection. Due to the lack of neutral connection, the power analyzer was wired following the 3V3A wiring schematic, also known as the three-wire method or the three watt-meter method. Figure 3-14 presents a schematic of the wiring diagram for the ALIP-power analyzer system. Figure 3-14 also denotes the locations of current and voltage measurement. Note that the current and voltage were directly wired into the power analyzer for improved accuracy.

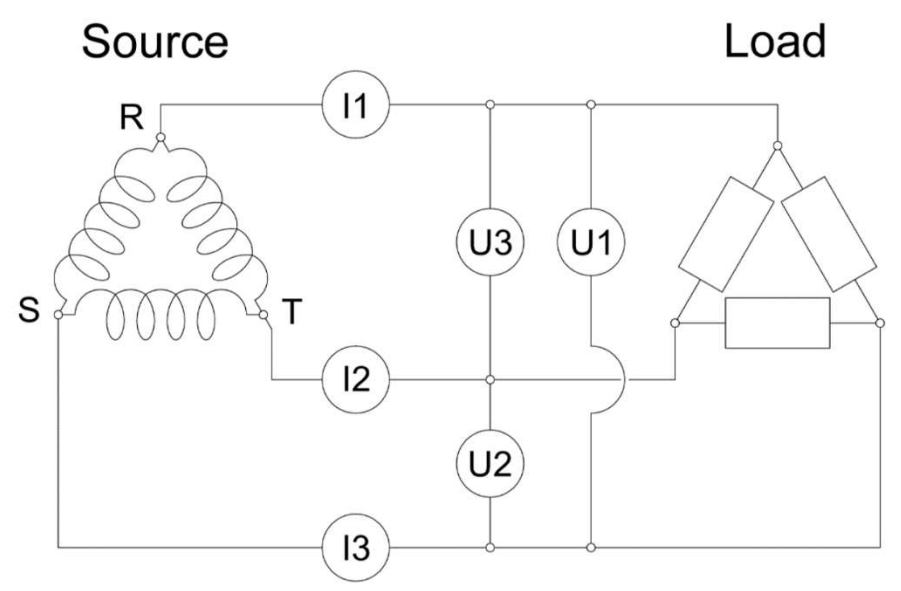


Figure 3-14: Wiring diagram of the ALIP to the Power Meter. Note that the source is a 480  $V_{rms}$ , delta configuration source with a 'wild-leg' and no neutral was used when wiring the power meter.

Each of the three I-U pairs (I1-U1, I2-U2, I3-U3) form a single watt-meter and a single power measurement. Following Blondel's theorem, the number of watt-meters need to accurately calculate the active is simply N-1 where N is the number of wires in the system [58]. For the three watt-meter method where three wires are used, Blondel's theorem states that only two power measurements are needed. Equation 3-13 shows the mathematical result of this theorem. Note that the I3-U3 pair never enter the active power calculation.

$$W_{e} = I_{1} \cdot U_{1} + I_{2} \cdot U_{2}$$
Equation 3-13

As specified by the manufacturer, the WT1600 has several factors which impact accuracy. Firstly, the accuracy is frequency dependent. Since the ALIP operating frequency of 120 Hz is in range  $66 \text{ Hz} < f \le 1 \text{kHz}$ , Equation 3-14 provides the base accuracy where Rng is the instrument range. Lastly, an additional factor of 1.5 was included to account for inaccuracies since the last calibration. Therefore, Equation 3-14 presents the total active power measurement error.

$$\sigma_{W_e} = \pm \{0.001 \cdot W_e + 0.001 \cdot Rng\} \times 1.5$$
Equation 3-14

#### 3.3 EXPERIMENTAL MEASUREMENTS

### 3.3.1 Axial Magnetic Field Distribution

Prior to installation, the axial distribution of the applied magnetic field's radial-component was characterized for each pump configuration. These measurements used a calibrated using an air-cored pick-up coil attached to a long rod. The pick-up coil and rod were inserted into the ALIP channel and the relative position of the coil was recorded. All measurements were taken in a dry pump with an applied voltage and current of  $100 \, V_{rms}$  and  $6 \, A_{rms}$ , respectively.

Figure 3-15 plots the Configuration-100 axial distribution of the radial magnetic field component at  $100 \, V_{rms}$  and  $6 \, A_{rms}$  in a dry pump. The axial position 'z' is reference from the start of the inner stator core at z=0 mm. Note that the end of the stator core is denoted by the solid black vertical line at z=300 mm. Observe that the applied magnetic field is non-uniform due to the finite-width coils. Peaks in the applied magnetic field appear due to the relative position of the pick-up coil and pump coils. For example, near the edge of a pump coil the applied field will spike in magnitude. Conversely, half-way between pump coils the applied field will have a minimum magnitude. While the coil position was attempted to measure the same location relative to the coil, errors were incurred in axial position as the coil was inserted. However, the same positions were measured for all configurations. Therefore, the Configuration-100 measurements will form the base-line on which the other configuration measurements are compared.

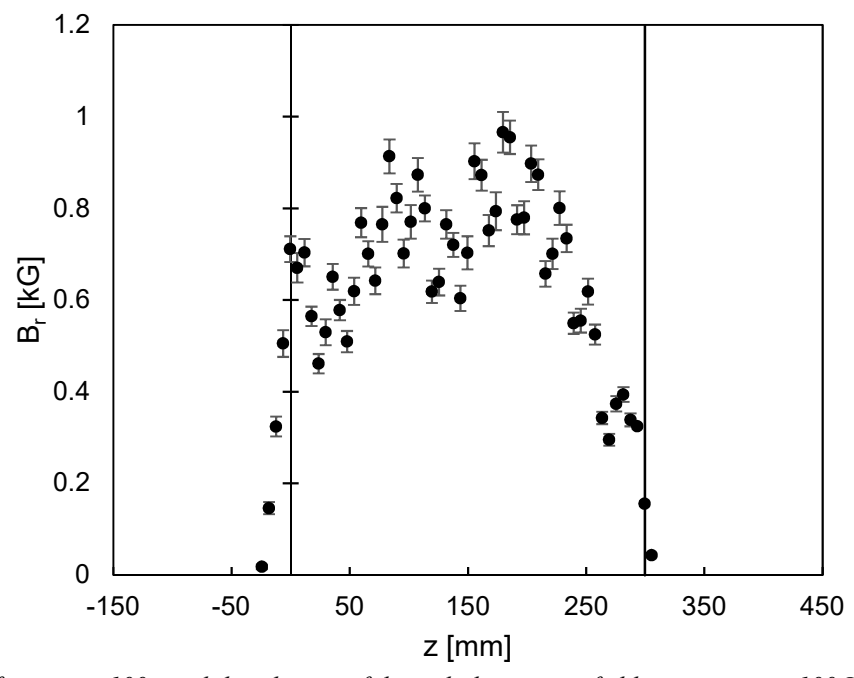


Figure 3-15: Configuration-100 axial distribution of the radial magnetic field component at  $100 \ V_{rms}$  and  $6 \ A_{rms}$  in a dry pump. The axial position 'z' is reference from the beginning of the inner stator at z=0 mm. Note that the end of the stator is denoted by the solid black vertical line at z=300 mm. Observe that the applied magnetic field is non-unifom and will produce peaks depending on the relative position of the pick-up coil and pump coils.

Figure 3-16 compares the Configuration-100 and Configuration-200 axial distribution of the radial magnetic field component at  $100~V_{rms}$  and  $6~A_{rms}$  in a dry pump. Recall that Configuration-200 shifted the coils and outer core by 75 mm toward the inlet. Note that the axial measurement 'z' is referenced from the inner core where z=0~mm and z=300~mm represent the start and end of the inner core, respectively. Additionally, the dashed vertical lines denote the start and end of the outer core and coils. Observe that applied field magnitude of Configuration-200 is suppressed at the outlet relative to Configuration-100. This can be explained by noting the lack of coils in this region to induce a magnetic field. Also, observe that the magnitude near the inlet of Configuration-200 is only slightly larger than Configuration-100. This can be explained by the existence of coils in this region. However, the magnitude is small due to the lack of the inner-ferromagnetic core which provides a low reluctance path for the magnetic field lines to travel. Therefore, it is concluded that Configuration-200 effectively shortens the active region of the pump.

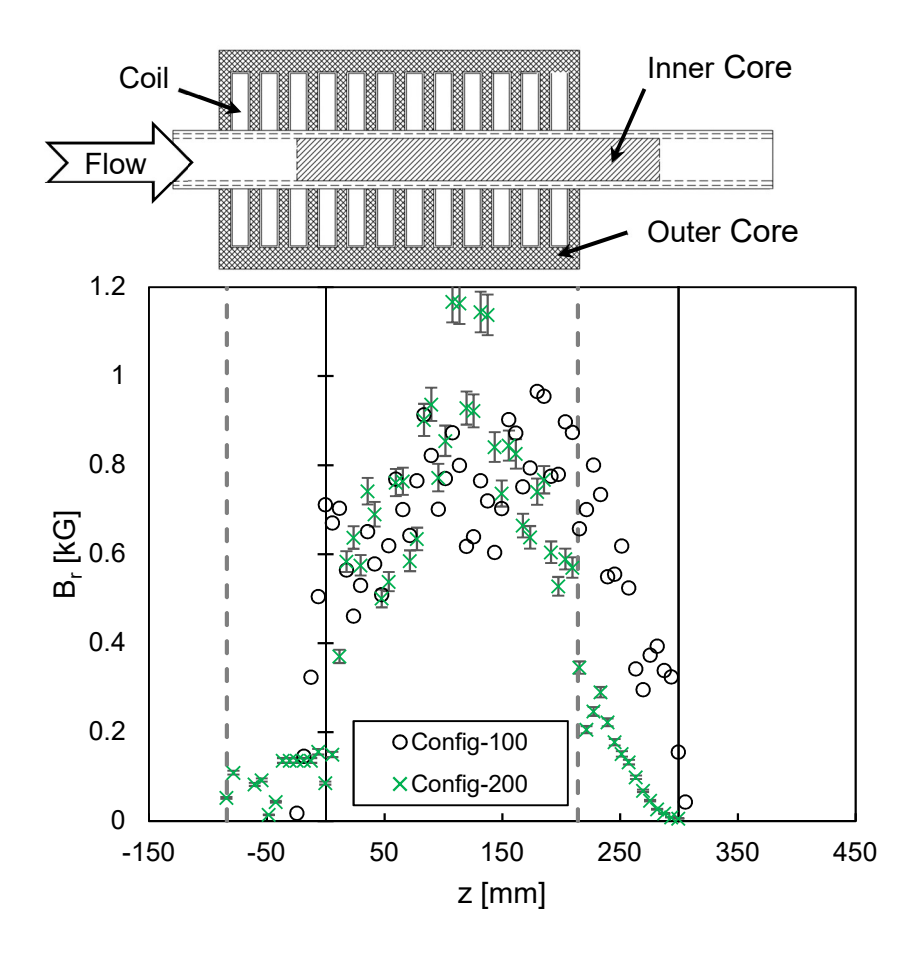


Figure 3-16: Comparison of Configuration-100 and Configuration-200 axial distribution of the radial magnetic field component at 100  $V_{rms}$  and 6  $A_{rms}$  in a dry pump. The axial position 'z' is reference from the beginning of the inner stator at z=0 mm. Note that the end of the stator is denoted by the solid black vertical line at z=300 mm. Also note that the dashed vertical lines denote the start and end of the outer stator.

Figure 3-17 compares the Configuration-100 and Configuration-300 axial distribution of the radial magnetic field component at  $100 \text{ V}_{rms}$  and  $6 \text{ A}_{rms}$  in a dry pump. Recall that Configuration-300 shifted the coils and outer core by 75 mm toward the outlet. Observe that applied field magnitude of Configuration-300 is suppressed at the inlet relative to Configuration-100. Like the suppression of the inlet field in Configuration-200, this can be explained by noting the lack of coils in this region to induce a magnetic field. Additionally, observe that the magnitude near the outlet of Configuration-300 is only slightly larger than Configuration-100. This can be explained by the existence of coils in this region but the lack of the inner-ferromagnetic core which provides a low reluctance path for the magnetic field lines to travel. Therefore, it is concluded that Configuration-300 effectively shortens the active region of the pump.

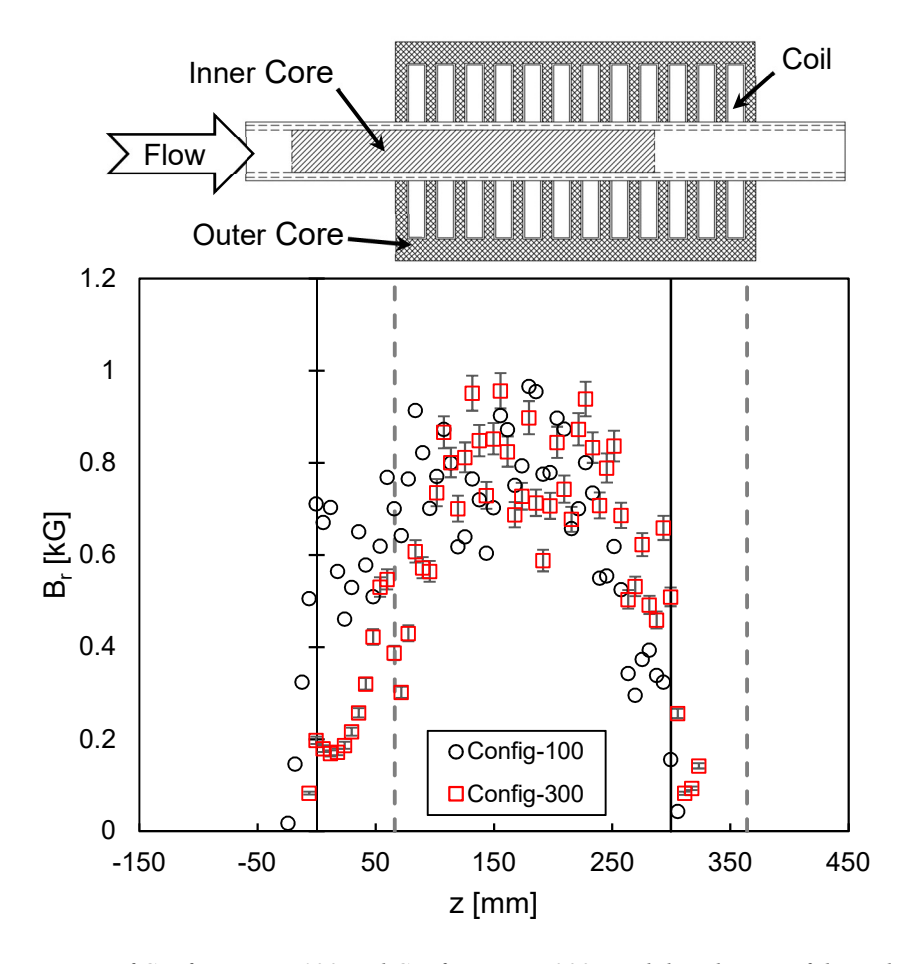


Figure 3-17: Comparison of Configuration-100 and Configuration-300 axial distribution of the radial magnetic field component at  $100\ V_{rms}$  and  $6\ A_{rms}$  in a dry pump. The axial position 'z' is reference from the beginning of the inner stator at z=0 mm. Note that the end of the stator is denoted by the solid black vertical line at z=300 mm. Also note that the dashed vertical lines denote the start and end of the outer stator.

Figure 3-18 and Figure 3-19 compare the axial distribution of the radial magnetic field component at 100  $V_{rms}$  and 6  $A_{rms}$  in a dry pump for Configuration-100 to Configuration-101 and Configuration-102, respectively. Recall that Configuration-101 and Configuration-102 apply the coil grading in Table 3-10 at the three inlet and three outlet coils. Note that the axial measurement 'z' is referenced from the inner core where z=0 mm and z=300 mm represent the start and end of the inner core, respectively. Observe that both configurations produce a suppression of the magnetic field over the first and last 100 mm of the inner stator length. Note that Configuration-102 is a more aggressive suppression compared to Configuration-101. Therefore, it is concluded that the magnetic field magnitude is effectively tapered at

these locations, beginning at near zero and increasing to roughly the same magnitude as in Configuration-100 in the center of the pump.

Table 3-10: Tap locations for each coil on the coil grading configuration tests.

CC	Cl.:C:	Coil Taps						
Configuration	Shifting	A1	B2	<i>C3</i>	A4-C9	A10	B11	C12
100	None	All Coils 1-80						
101	None	61-80	50-80	1-50	1-80	1-50	50-80	61-80
102	None	50-61	61-80	50-80	1-80	50-80	61-80	50-61

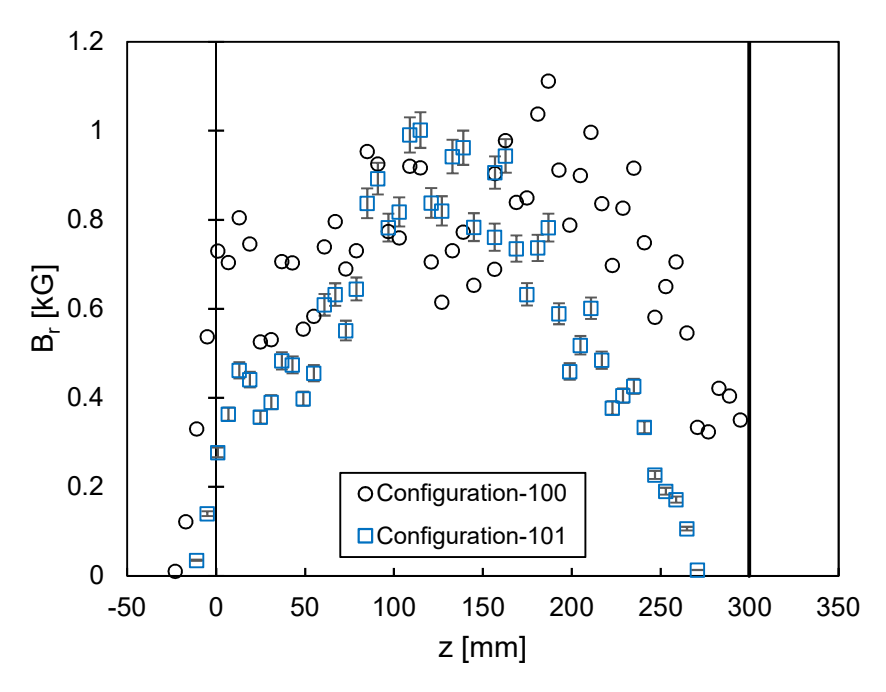


Figure 3-18: Comparison of Configuration-100 and Configuration-101 axial distribution of the radial magnetic field component at  $100\ V_{rms}$  and  $6\ A_{rms}$  in a dry pump. The axial position 'z' is reference from the beginning of the inner stator at z=0 mm. Note that the end of the stator is denoted by the solid black vertical line at z=300 mm. Also note that the dashed vertical lines denote the start and end of the outer stator.

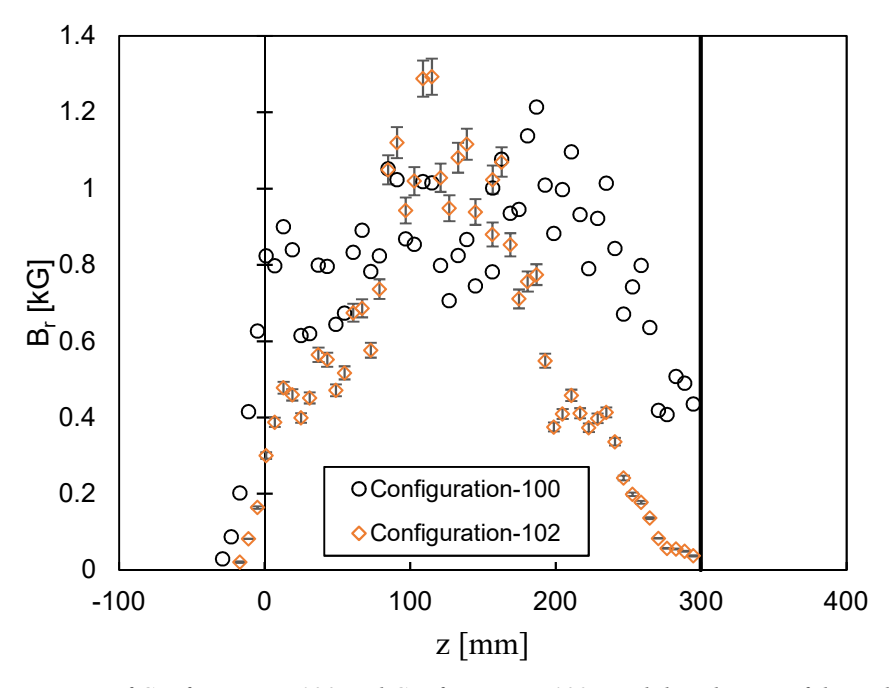


Figure 3-19: Comparison of Configuration-100 and Configuration-102 axial distribution of the radial magnetic field component at 100  $V_{rms}$  and 6  $A_{rms}$  in a dry pump. The axial position 'z' is reference from the beginning of the inner stator at z=0 mm. Note that the end of the stator is denoted by the solid black vertical line at z=300 mm. Also note that the dashed vertical lines denote the start and end of the outer stator.

### 3.3.2 Frictional Pressure Losses

Frictional pressure losses in the ALIP channel were characterized using water prior to pump installation. Figure 3-13 shows the location of the  $p_{loss,chan}$  measurements. Note that  $p_{loss,chan}$  was measured at a different location than  $\Delta p$  due to space limitations. These additional frictional losses are ignored in the following analysis as they were estimated to be small.

Water was used to measure frictional pressure losses due to limitations with installing the ALIP in another sodium system. In addition, the water testing was limited to testing a single temperature of 20 °C and a single pressure of roughly two bar gauge. Therefore, since the water testing did not achieve dimensional similitude with water, these data will produce an inaccurate friction factor. To overcome these limitations, water p<sub>loss,chan</sub> measurements were used to correct an empirical annular channel flow friction factor by using an effective ALIP length.

An effective ALIP length was quantified by comparing the experimental p<sub>loss,chan</sub> data in water to the empirical correlation. Equation 3-15 shows that the pressure drop in an annular channel can be related to flowrate through the Darcy Friction Factor f<sub>D</sub>. This friction factor can be determined through an empirical correlation which is a function of Reynolds number and relative channel roughness. Therefore, a pressure drop through the annular channel can be empirically calculated by knowing these parameters as well as the length, effective diameter, and density. However, the ALIP has an inlet and outlet cone as well as straight pipe sections between the transducers. This was corrected by varying the length L<sub>e</sub> to minimize the residuals between the experimental data and empirical correlation.

$$p_{loss,chan} = f_{D} \frac{L_{e}}{D_{H}} \frac{\rho U_{0}^{2}}{2}$$
Equation 3-15

Figure 3-20 plots the experimental and empirically calculated  $p_{loss,chan}$  data in water while Figure 3-21 plots the residuals. This analysis determined an effective ALIP channel length of 1.215 m would minimize the total residuals. Note that the physical ALIP channel length is 0.44 m.

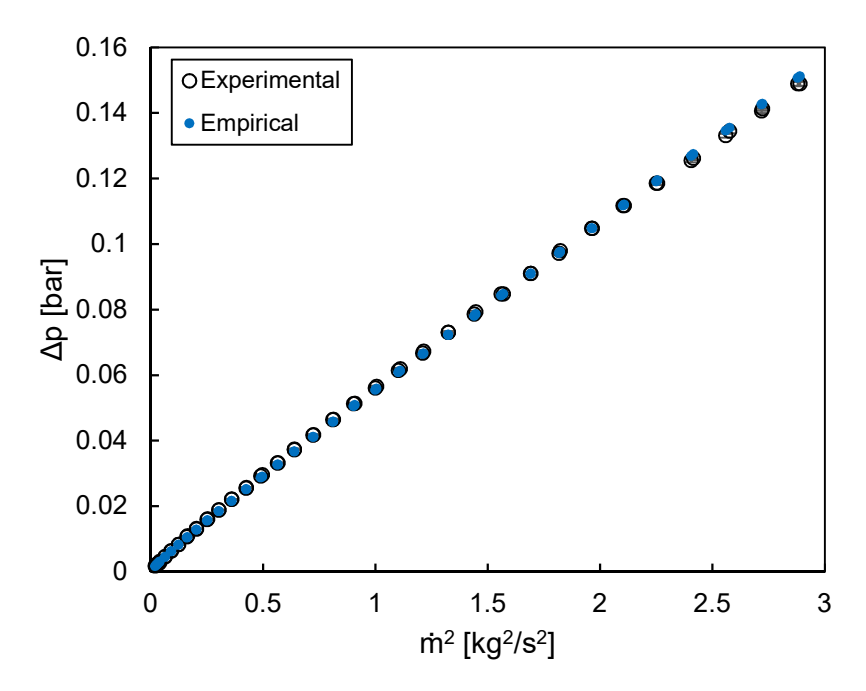


Figure 3-20: Experimental  $p_{loss,chan}$  data measured in water at 20 °C and 2 bar gauge pressure. Also plotted are the empirically calculated pressure losses in an annular channel using an effective ALIP channel length of 1.215 m. Note that the physical ALIP channel length is 0.44 m.

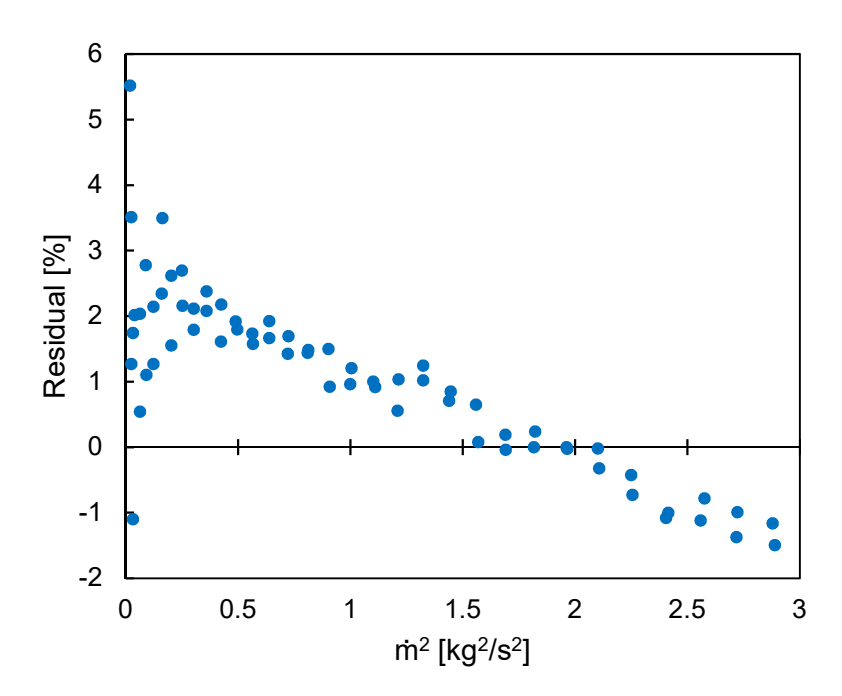


Figure 3-21: Residuals between the experimental  $p_{loss,chan}$  data and the empirical correlation.

Sodium frictional pressure losses were empirically calculated using Equation 3-15 with the effective length  $L_{\rm e}$  of 1.215 m found in the previous analysis. Note that the same annular channel friction factor correlation

was used with updated Reynolds numbers using sodium properties. Figure 3-22 plots the friction factor as a function of mass flowrate at 200  $^{\circ}$ C and 400  $^{\circ}$ C while Figure 3-23 plots the empirically calculated  $p_{loss,chan}$ .

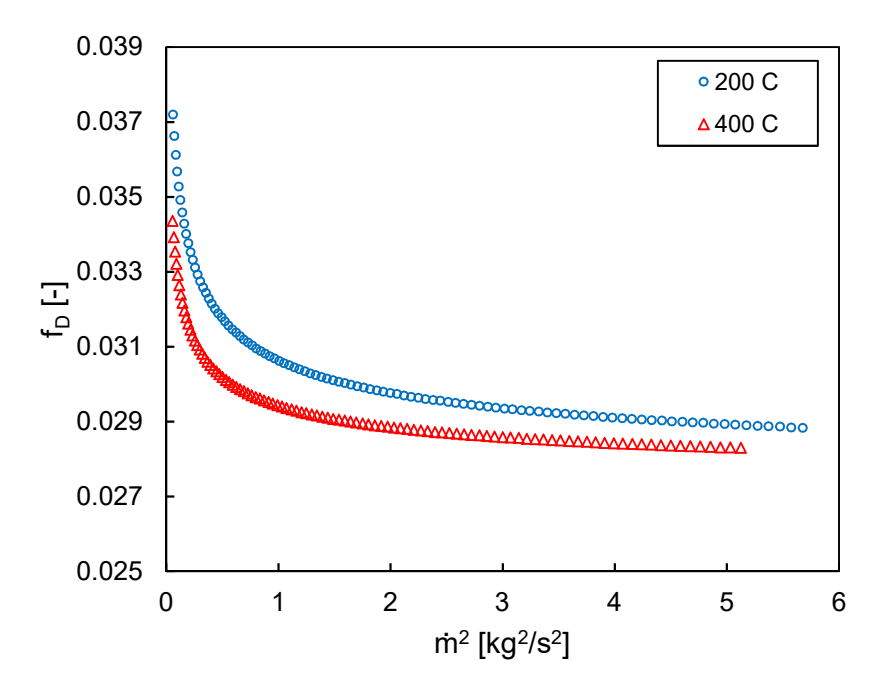


Figure 3-22: Empirical friction factor  $f_D$  evaluated using 200 °C and 400 °C sodium.

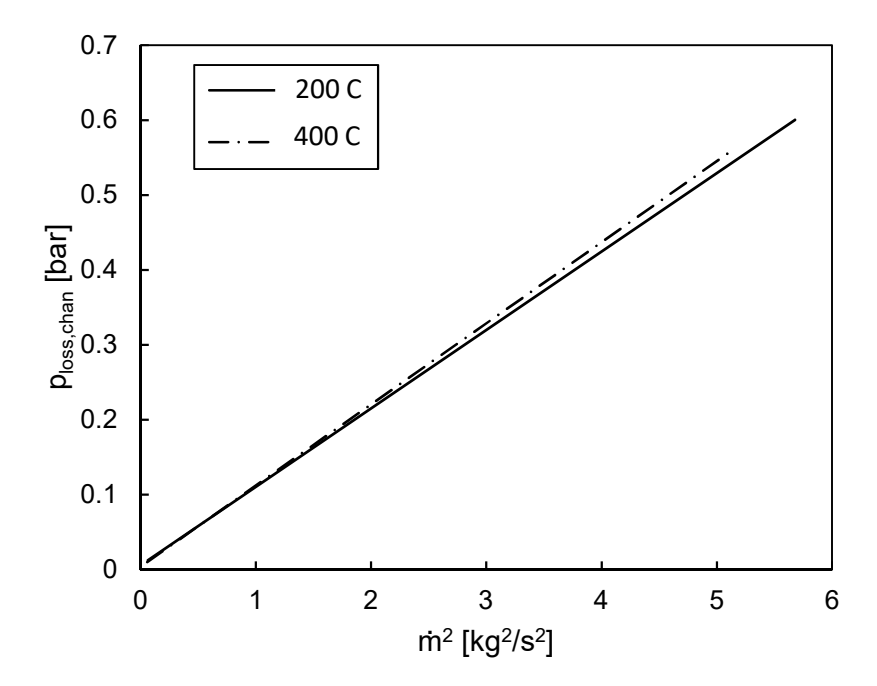


Figure 3-23: Empirically calculated  $p_{loss,chan}$  in 200 °C and 400 °C sodium using an effective channel length of 1.415 m.

# 3.3.3 Resistive Heating Losses

Input power was measured in a dry ALIP at several applied currents to characterize the resistive heating and other losses. Theoretical analysis identified resistive heating in the fluid and channel walls as major component to the total energy balance. The resistive heating in the channel walls was estimated by measuring the input power in a dry pump without sodium. Note that the pump channel has no external heaters. Coolers are located on the outside of the pump to cool the coils. However, these are fixed speed. Therefore, the final channel wall temperature is a result of inducting heating and parasitic losses. Therefore, the steady-state temperature was recorded as a function of magnet frequency and used to correct the theoretical electrical conductivity. Figure 3-24 plots the resulting temperatures and the curve used to correct for wall temperature.

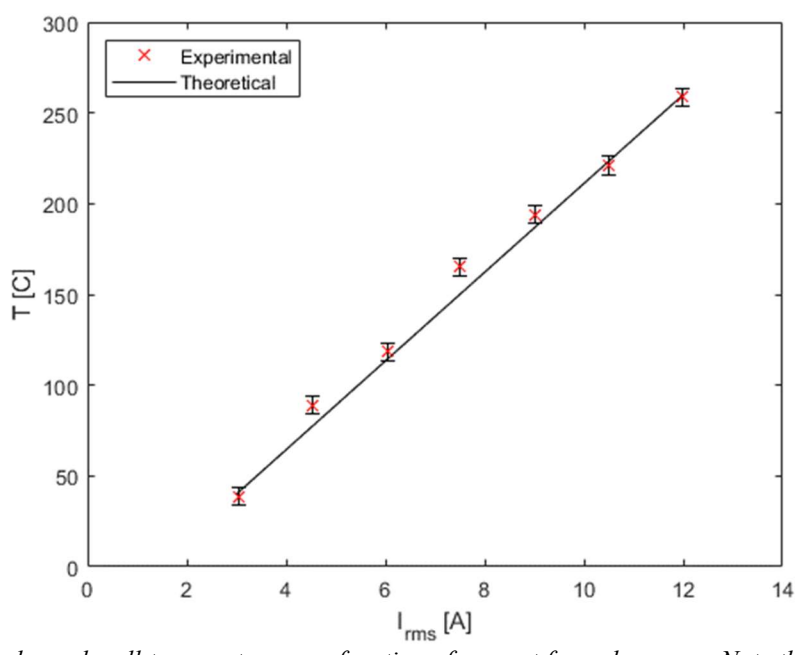


Figure 3-24: ALIP channel wall temperature as a function of current for a dry pump. Note that the temperature is a result of inductive heating and parasitic losses; no heaters or coolers were used to control the temperature.

Figure 3-25 plots the experimentally measured ALIP input power for a dry pump. Using the data from Figure 3-24, the resistive heating losses were analytically calculated using Equation 2-50 and compared to

the experimental measurements in Figure 3-25. Note that the theory seems to provide an accurate estimate of the resistive heating in the channel walls. However, recognize that the theory produces artificially lower estimates since it neglects the pump cores, resistive heating losses in the coils, as well as others. These factors would tend to increase the analytically calculated losses.

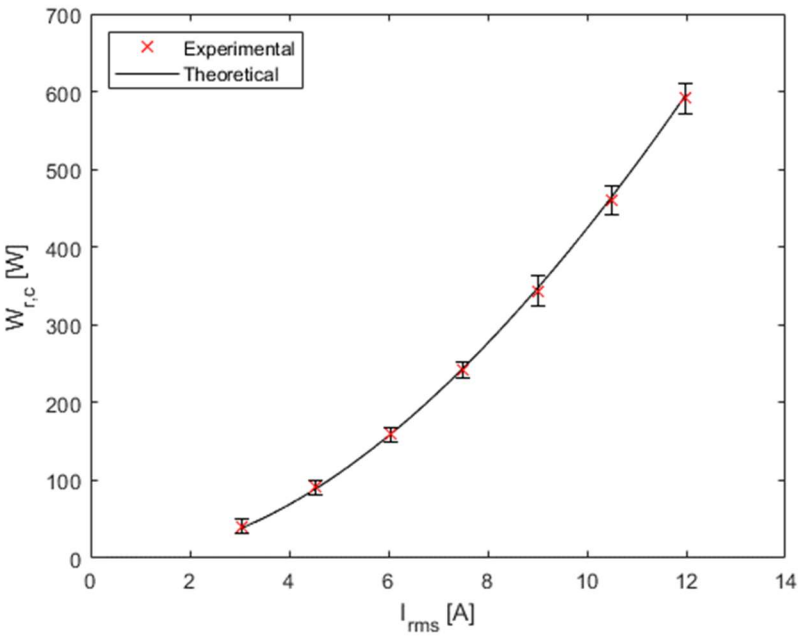


Figure 3-25: Experimentally measured ALIP input power for a dry pump compared to the analytically calculated resistive heating losses in the channel walls. Note that the analytic theory neglects core losses, coil resistive heating losses, as well as others. These factors would therefore tend to increase the analytically calculated term.

## 3.3.4 Standard Configuration Pressure-Flowrate and Efficiency Performance

ALIP pressure-flowrate curves of a standard configuration pump were measured in sodium at 200 °C and 400 °C. Figure 3-26 plots the pressure-flowrate curves at applied voltages of 50 V<sub>rms</sub>, 75 V<sub>rms</sub>, 100 V<sub>rms</sub>, and 150 V<sub>rms</sub>. During tests, the pump voltage was held constant and the flowrate was varied by a throttle. Note that the pump was tested in an envelope with a lower bound restricted by the ALIP-EMFM calibration and the upper bound restricted by the system loss curves. Figure 3-27 plots the ALIP pressure output as a function of mean slip under the same conditions. In contrast to typical centrifugal pressure-flowrate curves, the ALIP curves are nearly linear.

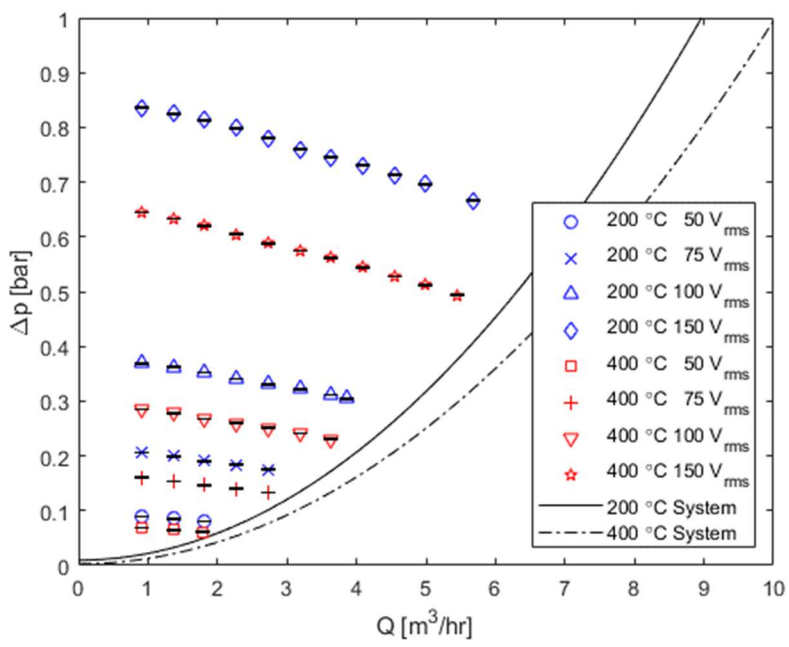


Figure 3-26: ALIP pressure-flowrate data at sodium temperatures of 200 °C and 400 °C and applied voltages of 50  $V_{rms}$ , 75  $V_{rms}$ , 100  $V_{rms}$ , and 150  $V_{rms}$ . The pump pressures were measured in an envelope with the lower flowrate bound restricted by the EMFM calibration and the upper flowrate bound restricted by the system loss curves.

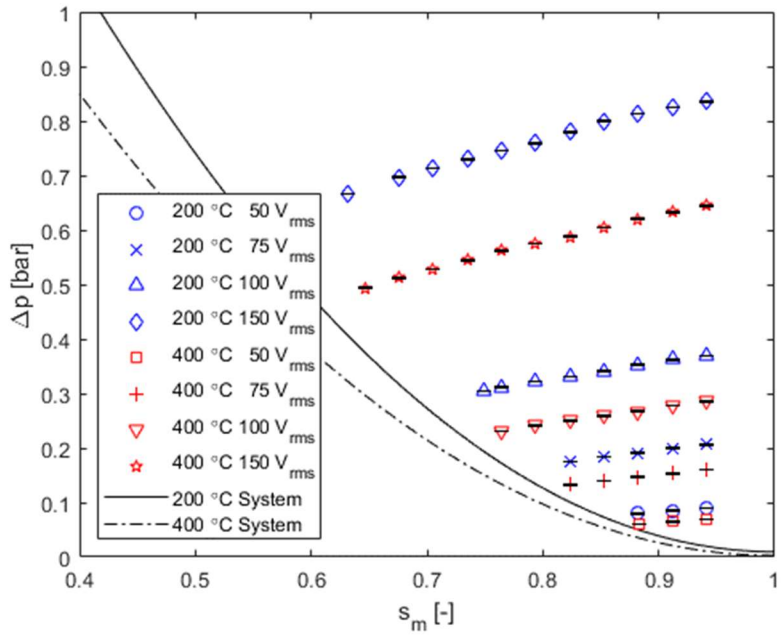


Figure 3-27: ALIP pressure-slip data at sodium temperature of 200 °C and 400 °C and applied voltages of 50  $V_{rms}$ , 75  $V_{rms}$ , 100  $V_{rms}$ , and 150  $V_{rms}$ . The pump pressures were measured in an envelope with the lower slip bound restricted by the system loss curves and the upper slip bound restricted by the EMFM calibration.

Electrical input power was measured concurrently at each pressure-flowrate condition. Equation 3-16 was used to define the pump efficiency from these measurements. Figure 3-28 plots the experimental efficiency measurements at as a function of mean-slip at voltages of 50 V<sub>rms</sub>, 75 V<sub>rms</sub>, 100 V<sub>rms</sub>, and 150 V<sub>rms</sub> at 200 °C and 400 °C. During these tests, the voltage was held constant and the flowrate was varied by a throttle. The maximum pump efficiency occurred at 53% mean slip and was measured as 12% and 10% at 200 °C and 400 °C, respectively.

$$\eta = \frac{\Delta p \cdot Q}{W_e}$$
Equation 3-16

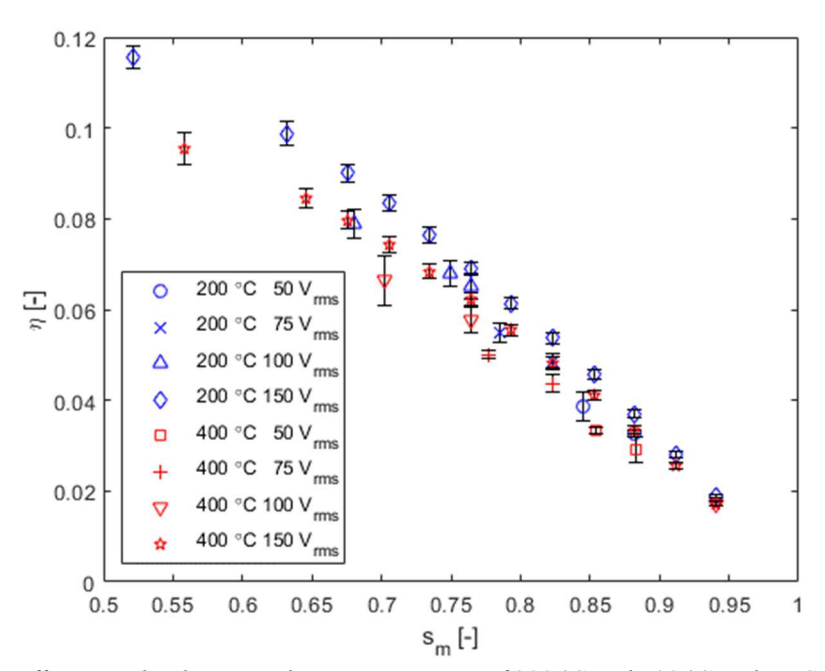


Figure 3-28: ALIP efficiency-slip data at sodium temperatures of 200 °C and 400 °C and RMS voltages of 50  $V_{rms}$ , 75  $V_{rms}$ , 100  $V_{rms}$ , and 150  $V_{rms}$ .

## 3.3.5 Coil Shifting Pressure-Flowrate and Efficiency Performance

ALIP pressure-flowrate curves were measured in sodium at 200 °C for two coil shifting configurations. Figure 3-29 shows that the two configurations shifted the coils and outer core by 75 mm towards the ALIP inlet and outlet. The inlet-shifted and outlet-shifted configurations are denoted as Configuration-200 and

Configuration-300, respectively. Additionally, note that the pressure-flowrate curves obtained in this section differ from the curves obtained in the previous section. Whereas the curves in Figure 3-26 were obtained by fixing the voltage and varying the loop resistance, the following curves were obtained by fixing the loop resistance and varying the pump voltage. This approach was deemed sufficient for comparing the performance of the modified pump to the standard pump.

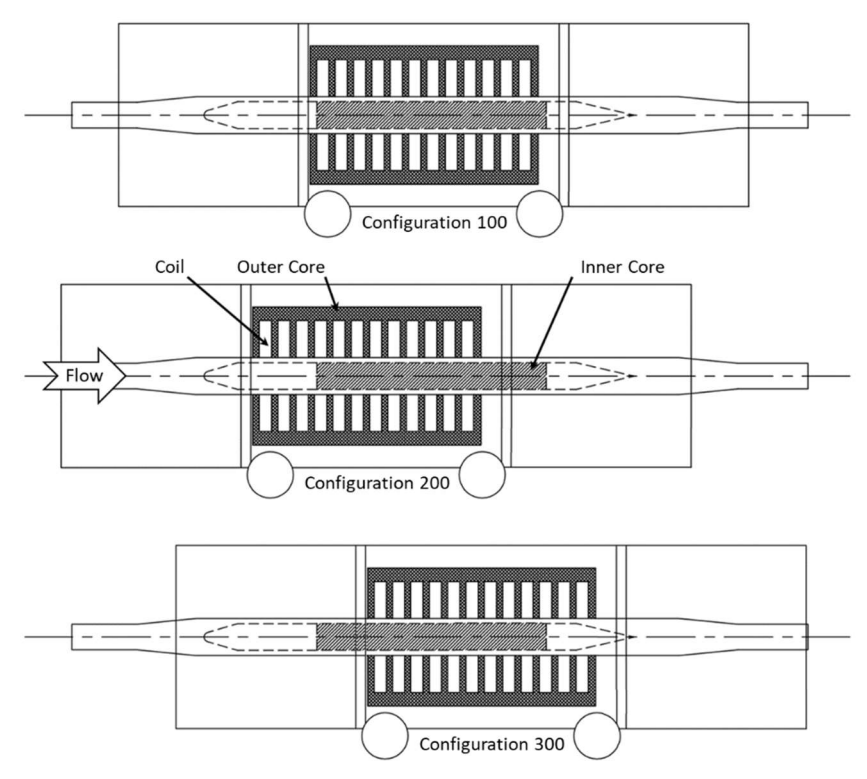


Figure 3-29: Qualitative sketch of coil shifting configurations of the experimental ALIP.

Figure 3-30 and Figure 3-31 compare the Configuration-100 and Configuration-200 pressure-flowrate and efficiency-flowrate curves at 200  $^{\circ}$ C. Note that these curves were obtain under fixed losses and variable pump voltages between 20  $V_{rms}$  and 150  $V_{rms}$ . Additionally, note that ALIP input power was measured concurrently at each pressure-flowrate condition and Equation 3-16 was used to define the pump efficiency. From these measurements, it was observed that Configuration-200 produced effectively no change in pressure-flowrate and efficiency-flowrate performance relative to Configuration-100.

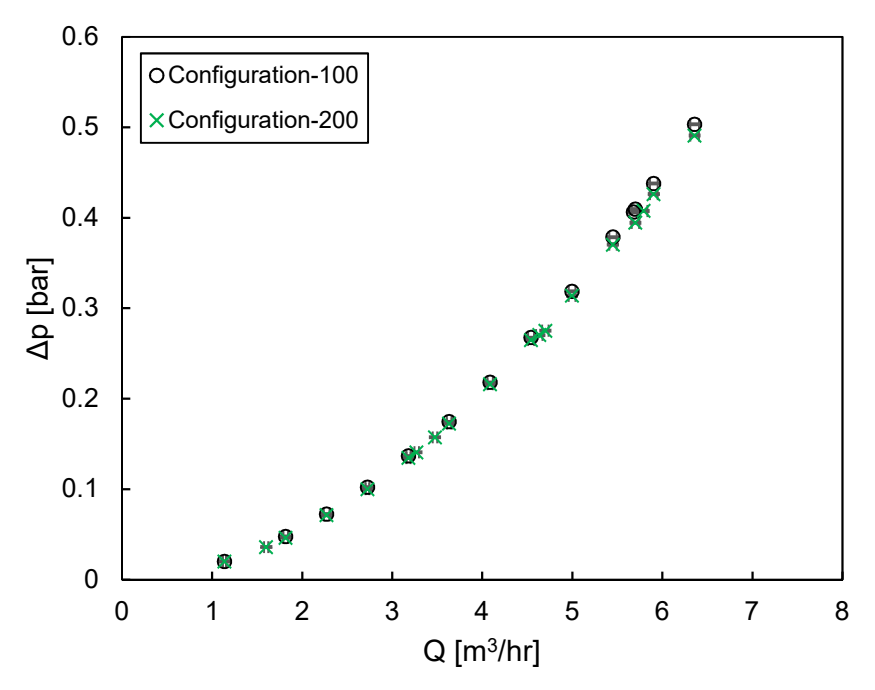


Figure 3-30: Comparison of Configuration-100 and Configuration-200 ALIP pressure-flowrate data at 200 °C. Note that these curves were obtained with fixed system losses and variable pump voltages between 20  $V_{rms}$  and 150  $V_{rms}$ .

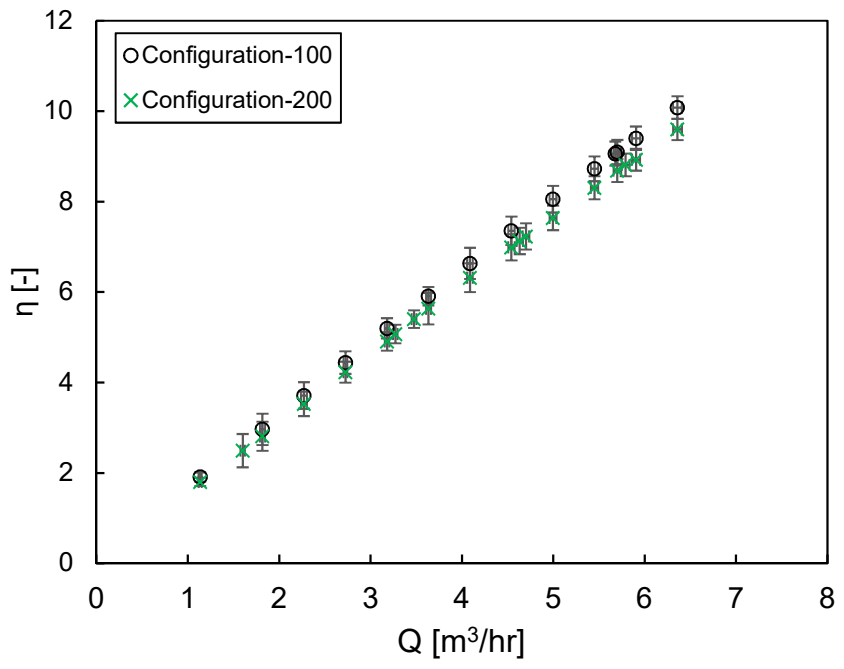


Figure 3-31: Comparison of Configuration-100 and Configuration-200 ALIP efficiency-flowrate data at 200 °C. Note that these curves were obtained with fixed system losses and variable pump voltages between 20  $V_{rms}$  and 150  $V_{rms}$ .

Figure 3-32 and Figure 3-33 compare the Configuration-100 and Configuration-300 pressure-flowrate and efficiency-flowrate curves at 200 °C. Note that these curves were obtain under fixed losses and variable

pump voltages between 20  $V_{rms}$  and 150  $V_{rms}$ . Additionally, note that ALIP input power was measured concurrently at each pressure-flowrate condition and Equation 3-16 was used to define the pump efficiency. From these measurements, it was observed that Configuration-300 produced a slight decrease in both pressure-flowrate and efficiency-flowrate performance relative to Configuration-100.

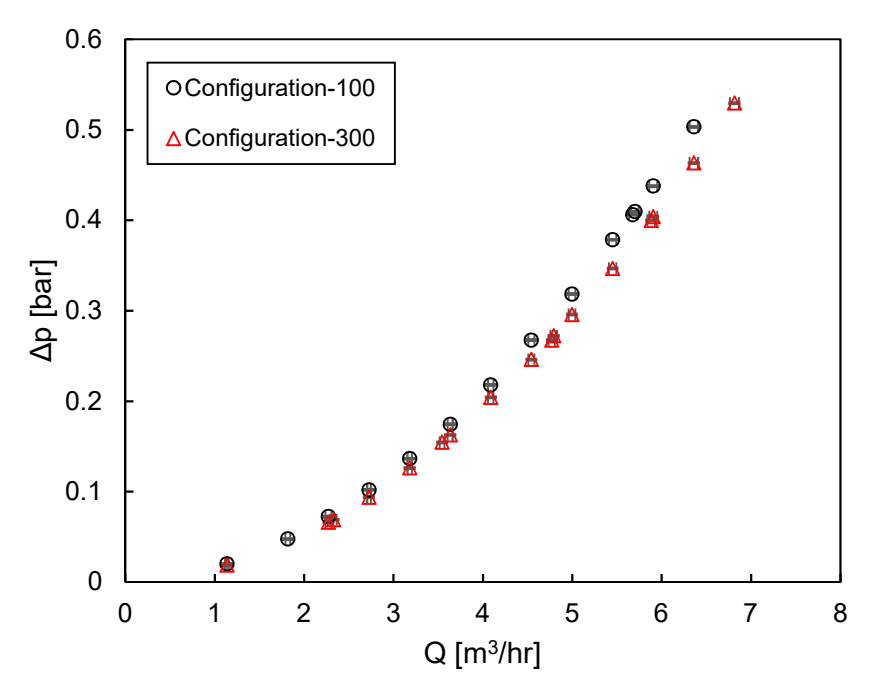


Figure 3-32: Comparison of Configuration-100 and Configuration-300 ALIP pressure-flowrate data at 200 °C. Note that these curves were obtained with fixed system losses and variable pump voltages between 20  $V_{rms}$  and 150  $V_{rms}$ .

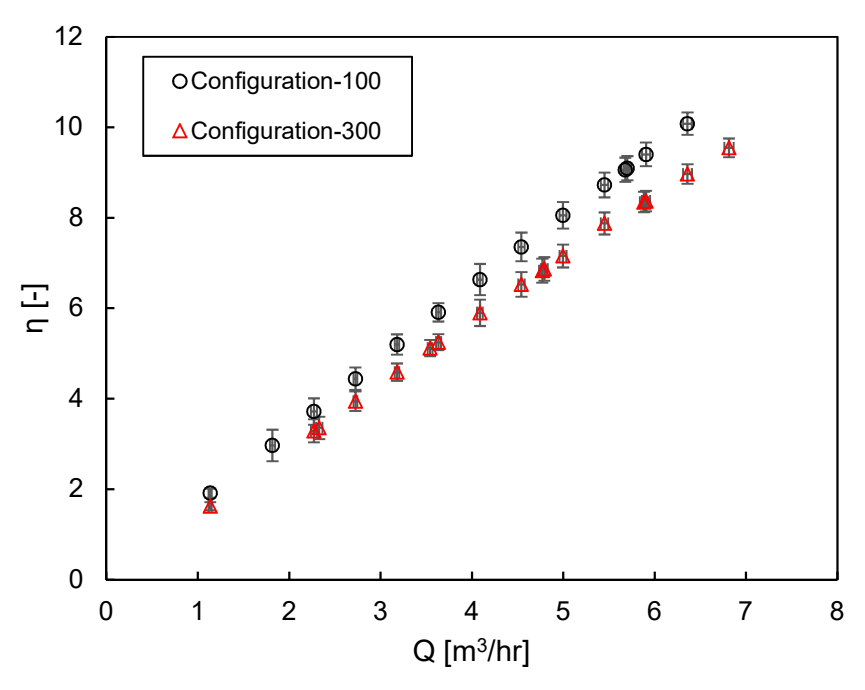


Figure 3-33: Comparison of Configuration-100 and Configuration-300 ALIP efficiency-flowrate data at 200 °C. Note that these curves were obtained with fixed system losses and variable pump voltages between 20  $V_{rms}$  and 150  $V_{rms}$ .

# 3.3.6 Coil Grading Pressure-Flowrate and Efficiency Performance

ALIP pressure-flowrate curves were measured in sodium at 200 °C for two coil grading configurations. Table 3-11 denotes the taps used in the first and last three ALIP coils. Two coil grading configurations were tested and denoted as Configuration-101 and Configuration-102. Like the Configuration-200 and Configuration-300 testing, the pressure-flowrate curves obtained in this section differ from the curves in Figure 3-26. While the curves in Figure 3-26 were obtained by fixing the voltage and varying the loop resistance, the following curves were obtained by fixing the loop resistance and varying the pump voltage. This approach was deemed sufficient for comparing the performance of the modified pump to the standard pump.

*Table 3-11: Tap locations for the coil grading configurations.* 

Configuration	Chifting	Coil Taps						
	Shifting	AI	<i>B2</i>	<i>C3</i>	A4-C9	A10	B11	C12
100	None	All Coils 1-80						
101	None	61-80	50-80	1-50	1-80	1-50	50-80	61-80
102	None	50-61	61-80	50-80	1-80	50-80	61-80	50-61

Figure 3-34 and Figure 3-35 compare the Configuration-100 and Configuration-101 pressure-flowrate and efficiency-flowrate curves at 200 °C. Note that these curves were obtain under fixed losses and variable pump voltages between 20  $V_{rms}$  and 150  $V_{rms}$ . Additionally, note that input power was measured concurrently at each pressure-flowrate condition and Equation 3-16 was used to define the pump efficiency. From these measurements, it was observed that Configuration-101 produced no change in pressure-flowrate and efficiency-flowrate performance relative to Configuration-100.

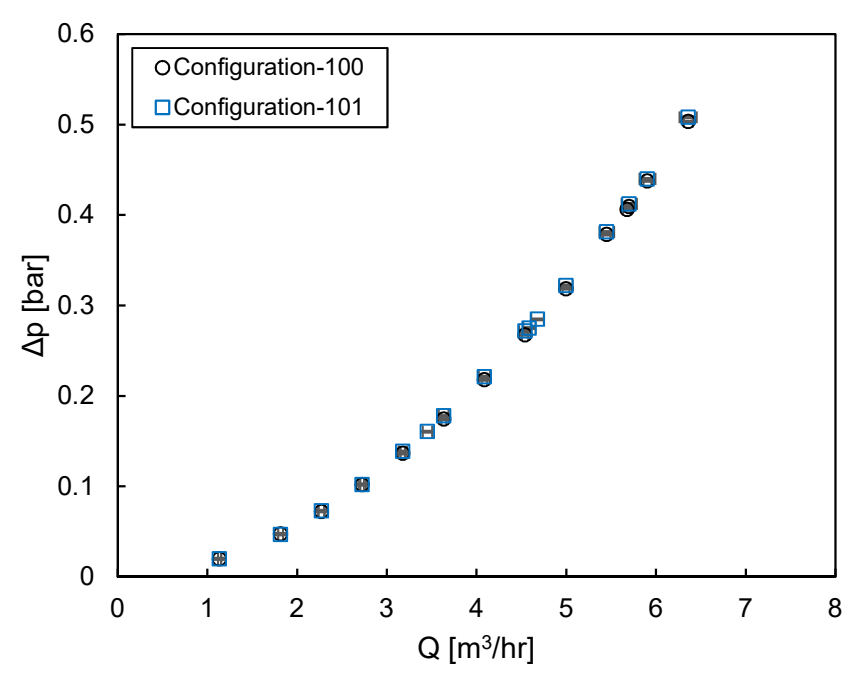


Figure 3-34: Comparison of Configuration-100 and Configuration-101 ALIP pressure-flowrate data at 200 °C. Note that these curves were obtained with fixed system losses and variable pump voltages between 20  $V_{rms}$  and 150  $V_{rms}$ .

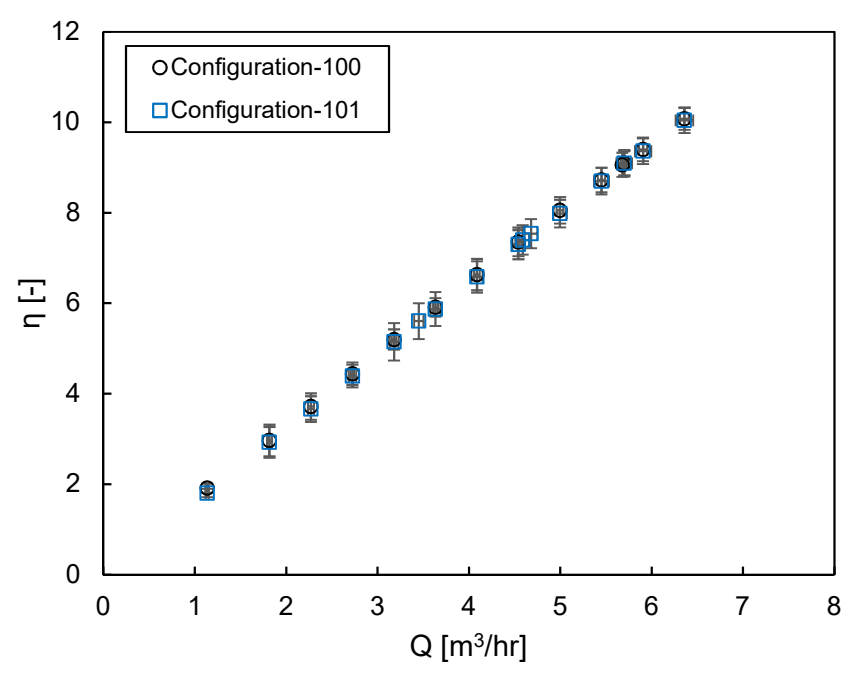


Figure 3-35: Comparison of Configuration-100 and Configuration-101 ALIP efficiency-flowrate data at 200 °C. Note that these curves were obtained with fixed system losses and variable pump voltages between 20  $V_{rms}$  and 150  $V_{rms}$ .

Figure 3-36 and Figure 3-37 compare the Configuration-100 and Configuration-102 pressure-flowrate and efficiency-flowrate curves at 200 °C. Note that these curves were obtain under fixed losses and variable pump voltages between 20 V<sub>rms</sub> and 150 V<sub>rms</sub>. Additionally, note that input power was measured concurrently at each pressure-flowrate condition and Equation 3-16 was used to define the pump efficiency. From these measurements, it was observed that Configuration-102 produced no change in pressure-flowrate and a slight change in efficiency-flowrate performance relative to Configuration-100.

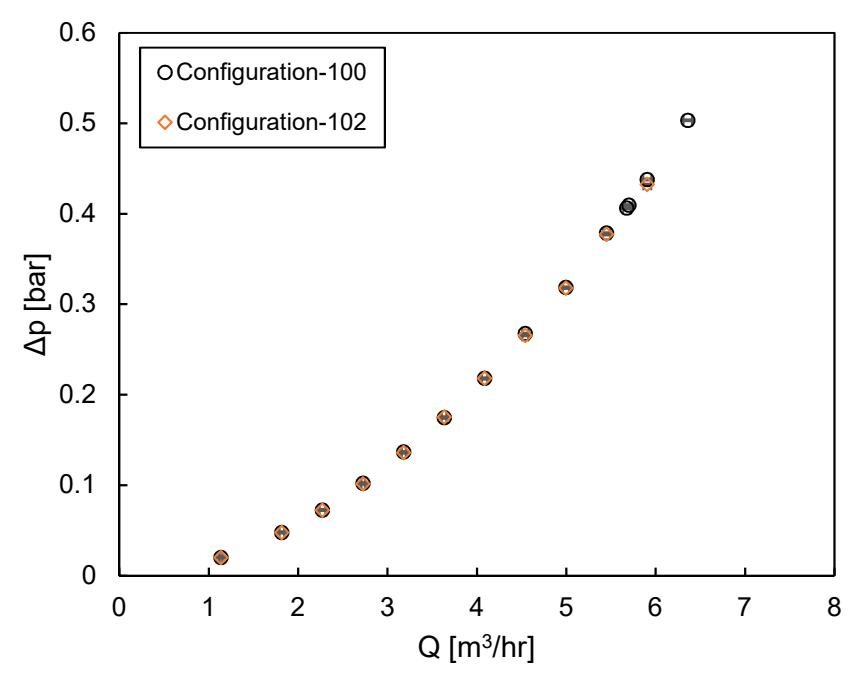


Figure 3-36: Comparison of Configuration-100 and Configuration-102 ALIP pressure-flowrate data at 200 °C. Note that these curves were obtained with fixed system losses and variable pump voltages between 20  $V_{rms}$  and 150  $V_{rms}$ .

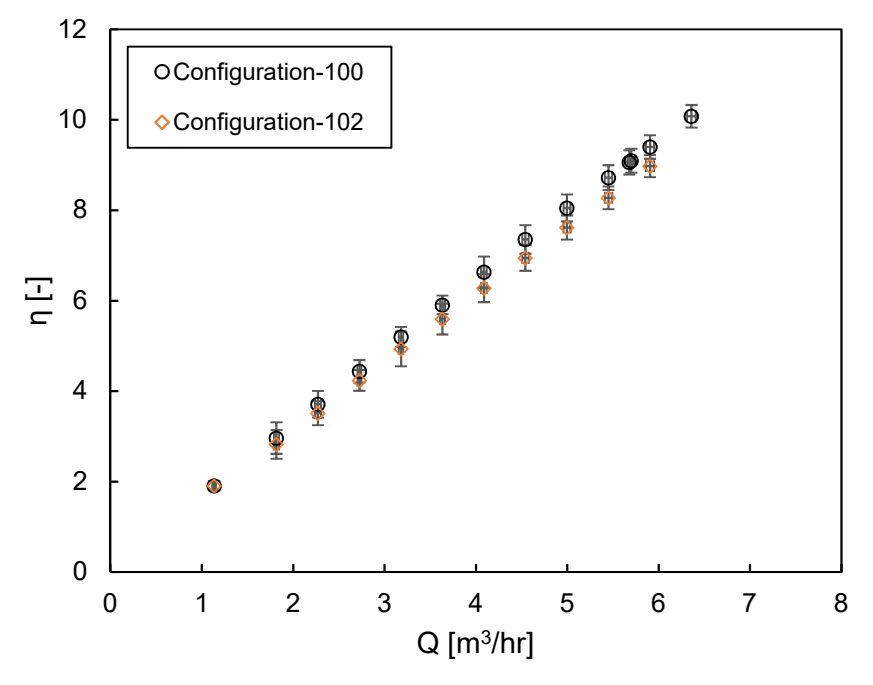


Figure 3-37: Comparison of Configuration-100 and Configuration-102 ALIP efficiency-flowrate data at 200 °C. Note that these curves were obtained with fixed system losses and variable pump voltages between 20  $V_{rms}$  and 150  $V_{rms}$ .

### 3.4 EFFECT OF THE FINITE LENGTH

Additional insights into ALIP performance characteristics can be gained by comparing the experimental pressure-flowrate and efficiency-flowrate curves to the analytic theory discussed earlier. However, recall that the ALIP theory calculated  $p_{EM}$  which is the total maximum pressure developed by the pump. However, the experimental measurements  $\Delta p$  also include frictional pressure losses in the pump channel and test system. Therefore, direct comparison of experimental data and analytic theory requires the transformation of  $\Delta p$  to  $p_{EM}$ . In this work, Equation 3-17 is used to relate the two where  $p_{EM,exp}$  is the experimentally measured maximum developed pressure and  $p_{loss,chan}$  are the pump channel pressure losses. Using Equation 3-17, a new efficiency is defined in Equation 3-18. Note that  $p_{EM,exp}$  is used instead of  $\Delta p$  as was done in Equation 3-16.

$$p_{\text{EM,exp}} = \Delta p + p_{\text{loss,chan}}$$
Equation 3-17

$$\eta_{\text{EM,exp}} = \frac{p_{\text{EM,exp}} \cdot Q}{W_e}$$
Equation 3-18

Recall that Equation 3-19 was used to calculated the theoretical maximum developed pump pressure. Note that  $p_{EM}$  is directly proportional to the relative velocity ( $U_B - U_0$ ) and the square of the magnetic field amplitude  $B_0^2$  by a constant C. Additionally, recall from ALIP theory that Equation 2-20 defined an important non-dimensional parameter called the effective Magnetic Reynolds number. This non-dimensional parameter describes the relative magnitudes of magnetic diffusion to induction. Note that the definition in Equation 2-20 neglects the non-magnetic gap between the cores. Therefore,  $Rm_f \cdot s_m$  is rescaled in Equation 3-20 where  $h_{ch}$  is the channel height and  $h_{gap}$  is the non-magnetic gap height [59]. Note that  $Rm_f \cdot s_m$  is also directly proportional to the relative velocity by a constant D. Thus, it is expected that  $p_{EM}$  will be linearly proportional to  $Rm_f \cdot s_m$  which can be interpreted as a non-dimensional flowrate or frequency. Thus, the transformed data will be plotted against this non-dimensional parameter.

$$p_{EM} = \frac{1}{2}\sigma_f L_e (U_B - U_0) B_0^2 = C \cdot B_0^2 \cdot (U_B - U_0)$$
Equation 3-19

$$Rm_f \cdot s_m = \frac{\mu_f \sigma_f}{k_0} \frac{h_{ch}}{h_{gap}} U_B \cdot s_m = D \cdot (U_B - U_0)$$
Equation 3-20

Note that in Equation 3-17 the term  $p_{loss,sys}$  is missing which accounts for frictional pressure losses in the system. In the ALIP work,  $p_{loss,sys}$  is neglected due to difficulty of characterizing this term given the pump control parameters. Recall that a system loss curve was generated by sweeping the pump over a range of applied voltages. By adjusting the voltage, the input current is adjusted to match the load, which in turn determines the magnetic field magnitude. Now, recall from Equation 3-19 that  $p_{EM}$  and  $Rm_f \cdot s_m$  are linearly proportional by  $(U_B - U_0)$  while only  $p_{EM}$  is dependent on  $B_0^2$ . Consequently, changing  $B_0^2$  will change the slope of  $p_{EM}$  with respect to  $Rm_f \cdot s_m$ . Therefore, the losses predicted by the system curve are only valid for the voltage at which it was evaluated. Generating a valid  $p_{loss,sys}$  curve requires fixing  $B_0^2$  and varying  $U_B$ . However, the ALIP is designed to run at a fixed frequency. Therefore, varying  $U_B$  to obtain a valid  $p_{loss,sys}$  curve was deemed impractical and neglected in this analysis.

## 3.4.1 Unmodified Pump Results

The experimental pressure data were transformed and compared to ALIP theory evaluated under the same conditions. Figure 3-38 and Figure 3-39 plot the 200 °C and 400 °C respectively at 50  $V_{rms}$ , 100  $V_{rms}$ , and 150  $V_{rms}$  under a constant frequency of 120 Hz.

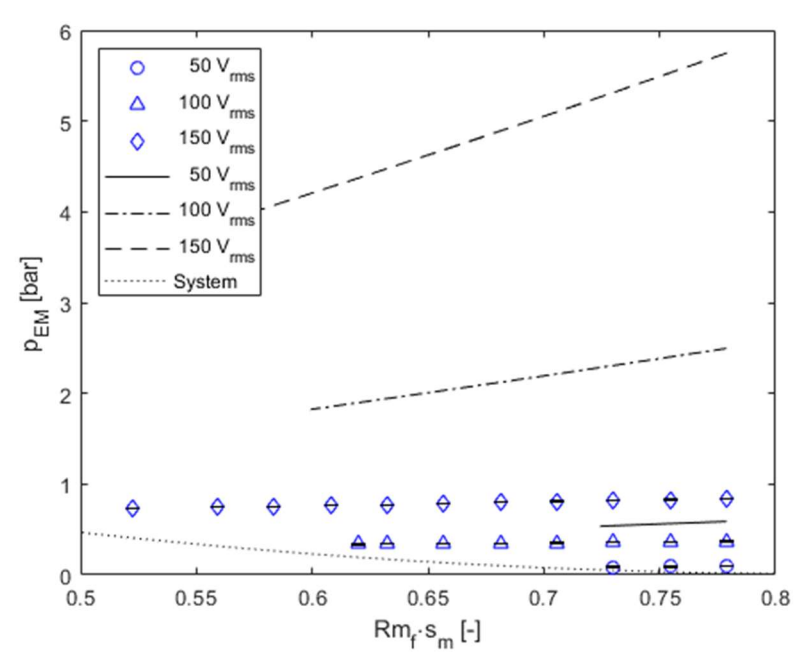


Figure 3-38: Plot of maximum output pressure as a function of  $Rm_f \cdot s_m$  at 200 °C at 50  $V_{rms}$ , 100  $V_{rms}$ , and 150  $V_{rms}$ . Note that changing the voltage changes the input current which therefore changes the magnitude field magnitude. Analytic theory shows that this will change the slope which is why three distinct curves appear versus a single curve.

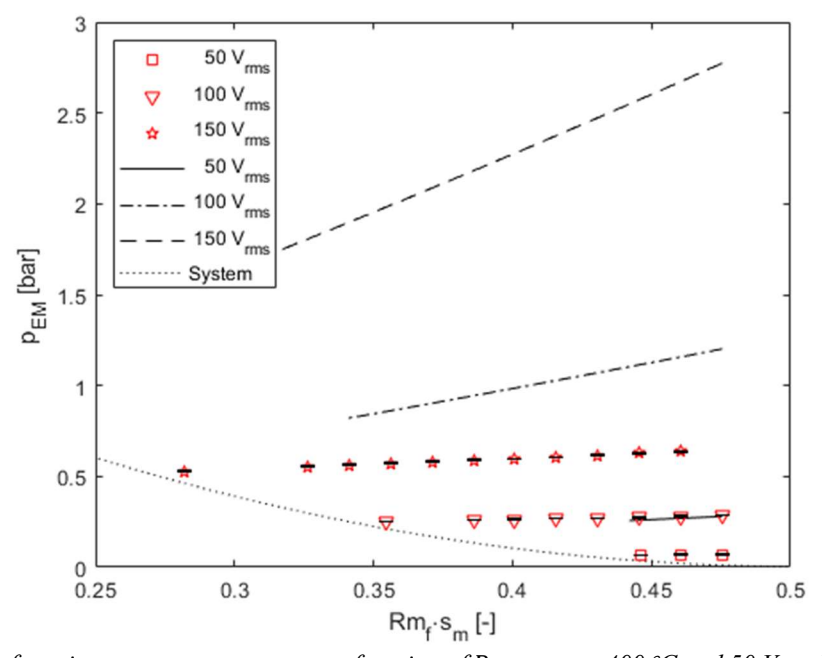


Figure 3-39: Plot of maximum output pressure as a function of  $Rm_f \cdot s_m$  at 400 °C and 50  $V_{rms}$ , 100  $V_{rms}$ , and 150  $V_{rms}$  under a fixed frequency of 120 Hz. Note that changing the voltage changes the input current which therefore changes the magnitude field magnitude. Analytic theory shows that this will change the slope which is why three distinct curves appear versus a single curve.

Figure 3-38 and Figure 3-39 show that the pressure-flowrate curves from Figure 3-27 are still a function of applied voltage. This is a result of the applied voltage changing the magnitude of  $B_0$  which changes the slope of  $p_{EM}$  as a function of  $Rm_f \cdot s_m$ . This effect is reflected in the theoretical predictions of  $p_{EM}$  using ALIP theory. However, note that ALIP theory significantly over-predicts the slope of  $p_{EM,exp}$ . This can partially be explained by  $p_{loss,sys}$  which was neglected in  $p_{EM,exp}$  due to the complexity of experimentally measuring the appropriate system loss curve.

Additionally, recall that  $B_0$  used by ALIP theory was experimentally characterized in a dry pump and averaged over the length. Clearly, this is unrealistic as the presence of a sodium flow load will impact the current draw, which will in turn impact  $B_0$ . Furthermore, the applied field is non-uniform over the pump length due to the finite-width coils and finite width core slots. Thus, it is likely that a simple average over the pump length will produce an inaccurate representation of  $B_0$  used in ALIP theory. In total, considering  $p_{loss,sys}$  will increase the slope of  $p_{EM,exp}$  and a better representation of  $B_0$  will decrease the slope of the theoretical  $p_{EM}$ . This will tend to bring the experimental data and theoretical predictions closer to agreeance.

Next, the experimental efficiency data were transformed and compared to ALIP theory evaluated under the same conditions. Figure 3-40 plots these data at 200 °C and 400 °C at 50  $V_{rms}$ , 100  $V_{rms}$ , and 150  $V_{rms}$  under a constant frequency of 120 Hz. Also plotted are curves generated from ALIP theory at the same temperatures and applied voltages of 50  $V_{rms}$  and 150  $V_{rms}$ .

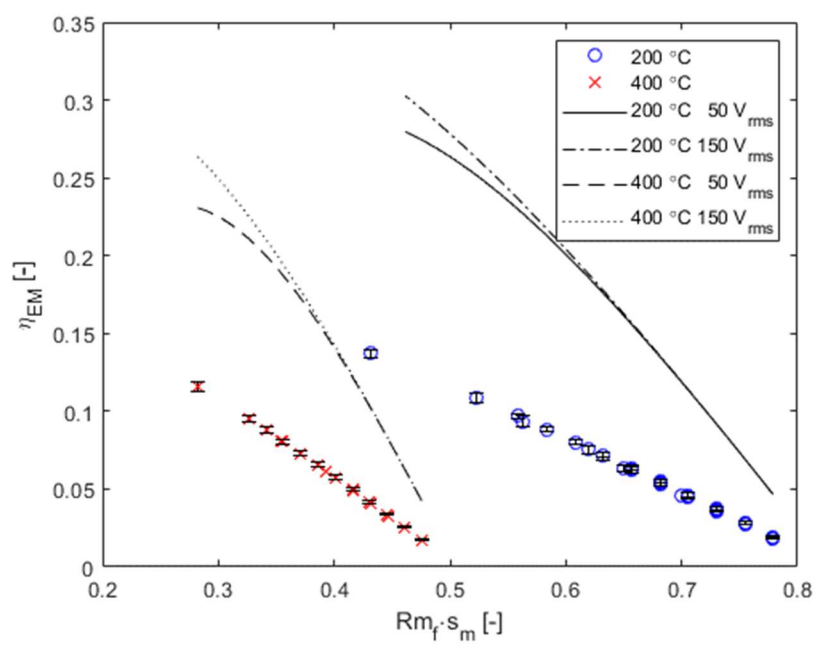


Figure 3-40: Plot of pump efficiency as a function of  $Rm_f \cdot s_m$  at 200 °C and 400 °C under pump voltages of 50  $V_{rms}$  and 150  $V_{rms}$  and a fixed frequency of 120 Hz.

Figure 3-40 shows that the experimental efficiency curves are a weak function of voltage while the theoretical curves are a much stronger function of voltage. As stated earlier, this may also be a result of neglecting  $p_{loss,sys}$  in  $p_{EM,exp}$ . It is expected that at a given voltage, a smaller value of  $Rm_f \cdot s_m$  implies a high fluid velocity, which in turn results in higher frictional losses, and therefore a lower efficiency. Another factor may be the over-prediction of  $W_{r,f}$ . Recall that the magnetic field amplitude  $B_0$  used in ALIP theory was experimentally measured in a dry pump and averaged over the length. This likely results in an over-estimation of the applied magnetic field which will result in an over-prediction of both  $p_{EM}$  and  $W_{r,f}$ . Consequently, the predicted efficiency will be larger than the experiment and will be a stronger function of the applied voltage. In total, considering  $p_{loss,sys}$  will result in  $\eta_{EM,exp}$  having a stronger dependence with applied voltage and a better representation of  $B_0$  will decrease the magnitude of the theoretical  $\eta_{EM}$ . This will tend to bring the experimental data and theoretical predictions closer to agreeance.

While the consideration of  $p_{loss,sys}$  and a better representation of  $B_0$  will improve the theoretical predictions, it is important to note the limitations of the ALIP theory in this work. Firstly, as stated earlier the theory neglects the finite dimensions of the outer stator and coil assembly. It has been observed that the finite dimensions of this assembly will significantly impact the resulting distribution of  $B_r(z)$  [38] [60]. Consequently, in addition to impacting  $B_0$  this effect also means that the ALIP theory will be unable to consider the grading of individual coils. Therefore, the analytic theory will provide little insight into the effects of coil grading. Considering the effect of finite width coils and stator teeth requires a more sophisticated ALIP model which was deemed to be out of scope for this work.

Secondly, the ALIP theory used in this work considers an infinite permeability stator core of zero conductivity as well as an infinite current sheet. While these assumptions made an analytic solution tractable, it means that the pump powers cannot be directly derived [30]. Additionally, this means that the magnetic field must be a known. This is rarely the case in a real ALIP and the limitations of measuring the field in air prior to testing have already been discussed. Furthermore, this suggests that the theory will provide little inside into the effects of coil shifting. Considering the effect of finite permeability cores and electrical powers requires a more sophisticated ALIP model which was deemed to be out of scope for this work.

Overall, the ALIP theory in this form predicts the experimental pump performance characteristics with some great degree of accuracy given its simplicity. Additional accuracy could be gained by measuring an appropriate p<sub>loss,sys</sub> curve and defining an improved representation of B<sub>0</sub>. Nevertheless, when compared to ALIP theory, the experimental data shows that the finite length of the channel strongly impacts ALIP performance. Unfortunately, more detailed consideration of the finite length and the impact of coil grading and coil shifting will require a more sophisticated ALIP model. However, this is deemed to be out of scope

for this work. Thus, moving forward the impact of coil grading and coil shifting will be evaluated through the comparison of the standard configuration to modified configuration performance.

### 3.4.2 Coil Shifting Results

Figure 3-41 and Figure 3-42 compare the Configuration-100, Configuration-200, and Configuration-300 experimental pressure and efficiency performance as a function of flowrate. Recall that Configuration-100 is the standard configuration pump, Conifugration-200 shifts the outer core by 75 mm towards the inlet, and Configuration-300 shifts the outer core by 75 mm towards the outlet. Also note that all the coils have the full number of turns. Recall from the previous section that since the ALIP-theory in this work neglects the finite permeability of the ferromagnetic cores, the effectiveness of a modified configuration will be evaluated through comparison of the Configuration-100 performance. Note that the performance curves were taken at a fixed frequency with variable pump voltages. Fixing the voltages was deemed unnecessary for evaluating the effectiveness of a given configuration.

Figure 3-41 shows that the pressure performance remained effectively unchanged between Configuration-100 and the two shifted configurations. A slight decrease in pressure performance was observed in Configuration-300. Similarly, Figure 3-42 shows only a marginal decrease in efficiency for the shifted configurations compared to Configuration-100. Configuration-300 was observed to have a slightly greater reduction in efficiency compared to Configuration-200.

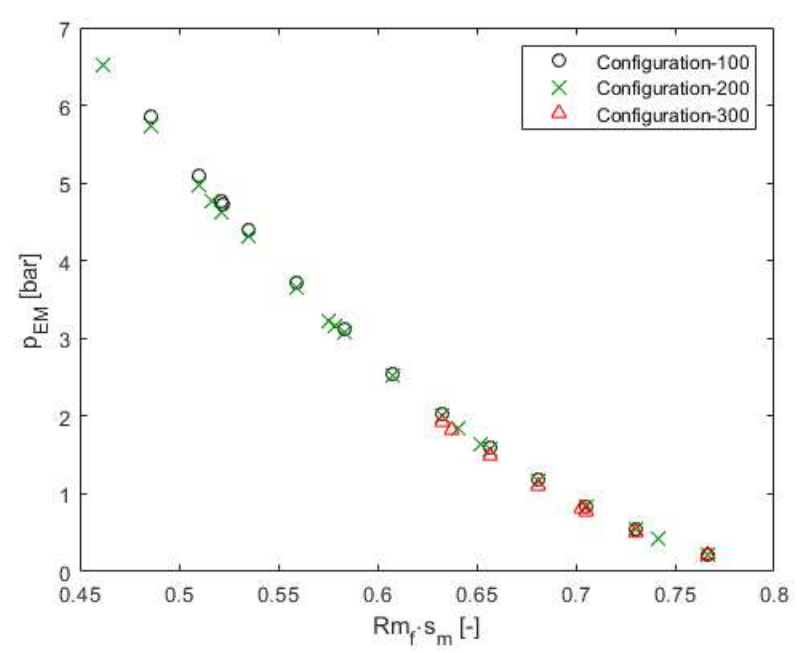


Figure 3-41: Comparison of Configuration-100, Configuration-200, and Configuration-300 differential pressure output as a function of flowrate over the applied voltages of 20  $V_{rms}$  and 150  $V_{rms}$  and under a frequency of 120 Hz.

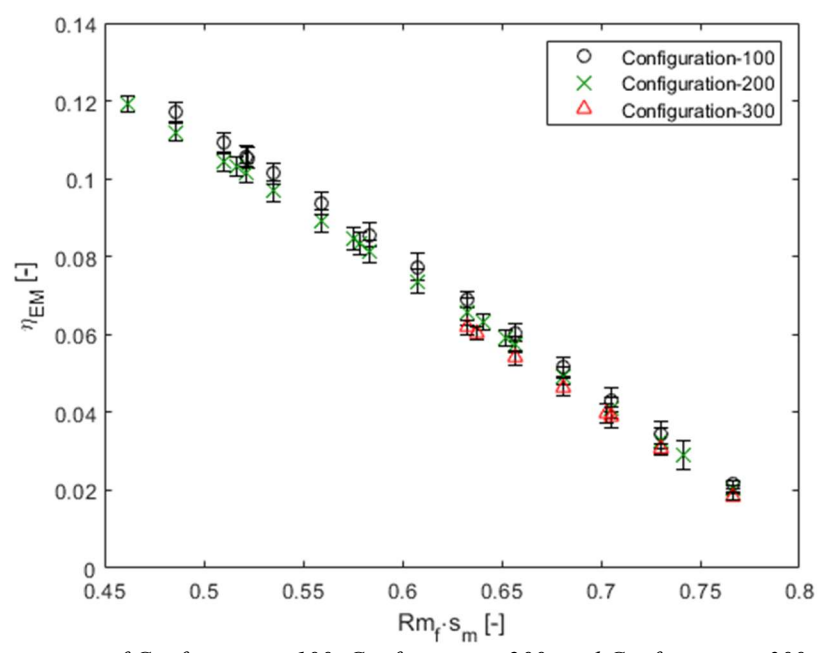


Figure 3-42: Comparisons of Configuration-100, Configuration-200, and Configuration-300 efficiency as a function of flowrate over the applied voltages of 20  $V_{rms}$  and 150  $V_{rms}$  and under a frequency of 120 Hz.

The insignificant change in pressure-flowrate and efficiency performance in Figure 3-41 and Figure 3-42 respectively can be explained by recalling equation for the maximum ALIP output pressure. Equation 3-19

states that given a fixed frequency and flowrate, the only free parameter to adjust pressure is B<sub>0</sub>. Recall from Figure 3-16 and Figure 3-17 that the coil shifting effectively reduced the active pump length. Consequently, for the pump to match the system pressure at a given flowrate, B<sub>0</sub> must be increased for Configuration-200 relative to Configuration-100 at the same pressure-flowrate condition. This requires that the input current increase as well as the input voltage. Thus, the performance of the pump will be approximately constant but the efficiency will be reduced due to the increased current draw.

It is likely that coil shifting only marginally impacts pump performance due to the high operating frequency relative to the fluid velocity. During the literature review, it was noted that the Finite Length Effect was most pronounced at frequencies which were comparable to the fluid velocity. However, recall that the lowest mean slip was roughly 50% meaning that the magnetic field velocity was at least twice as large as a fluid velocity. Therefore, it is likely that the frequency was too large to observe any significant effect. Note that while the frequency of the pump can be adjusted to reduce the relative velocity, recall that the maximum developed pump pressure also decreases proportionally. Consequently, given a fixed current, the pump will be unable to produce enough pressure to match the system resistance. This can be compensated by increasing the applied current. However, note that the maximum continuous pump current is only 12 A<sub>rms</sub>. Therefore, it is concluded that the pump is simply too small to observe the Finite Length Effect and any changes in performance caused by the coil shifting configuration.

# 3.4.3 Coil Grading Results

Figure 3-43 and Figure 3-44 compare the Configuration-100, Configuration-101, and Configuration-102 experimental pressure and efficiency performance as a function of flowrate. Recall that the coil grading configurations are given in Table 3-11. Also note that the coils are centered and remain un-shifted. Recall from the previous section that since the ALIP-theory in this work neglects the individual coils, the effectiveness of a modified configuration will be evaluated through comparison of the Configuration-100

performance. Note that the performance curves were taken at a fixed frequency with variable pump voltages. Fixing the voltages was deemed unnecessary for evaluating the effectiveness of a given configuration.

Figure 3-43 shows that the pressure performance remained unchanged between Configuration-100 and the two coil grading configurations. Similarly, Figure 3-44 shows only a slight decrease in efficiency for the shifted configurations compared to Configuration-100.

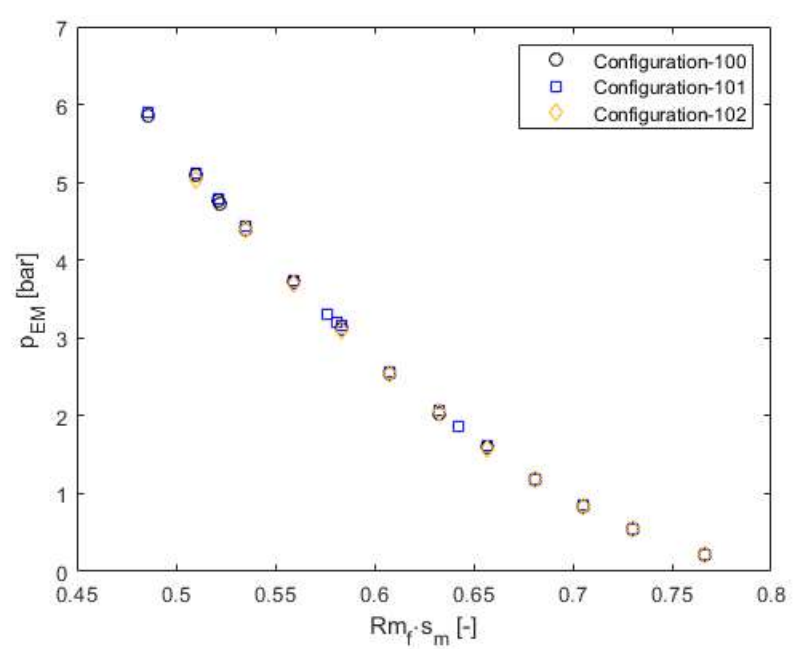


Figure 3-43: Comparison of Configuration-100, Configuration-101, and Configuration-102 differential pressure output as a function of flowrate over the applied voltages of 20  $V_{rms}$  and 150  $V_{rms}$  and under a frequency of 120 Hz.

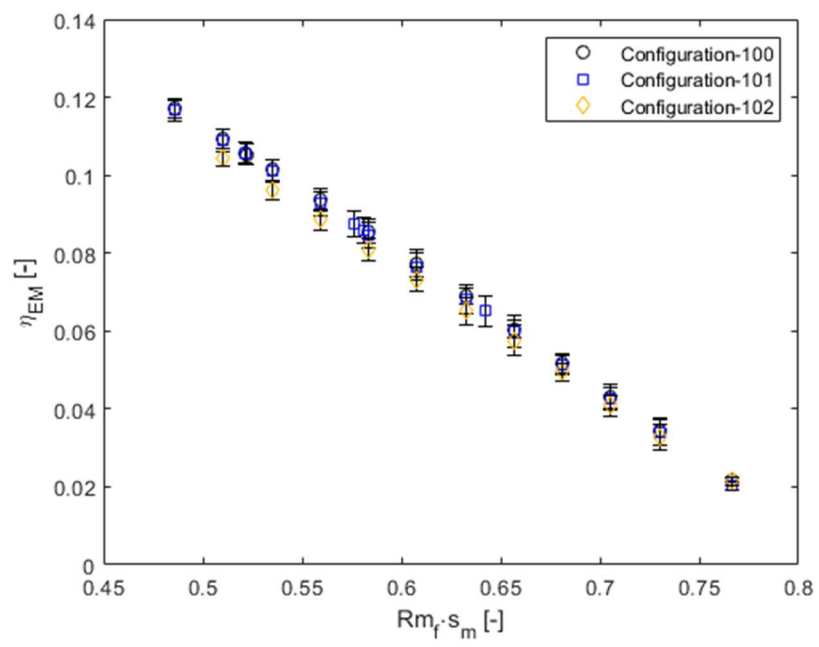


Figure 3-44: Comparison of Configurations-100, Configuration-101, and Configuration-102 efficiency as a function of flowrate over the applied voltages of 20  $V_{rms}$  and 150  $V_{rms}$  and under a frequency of 120 Hz.

The insignificant change in pressure-flowrate performance from Figure 3-43 and the slight reduction of efficiency from Figure 3-44 can be interpreted like the coil shifting results. For a given flowrate, the relative velocity is fixed and therefore the only free parameter to adjust pump pressure is B<sub>0</sub>. As observed in Figure 3-18 and Figure 3-19, coil grading effectively reduces the active length of the pump. Consequently, for the pump to match the system pressure at a given flowrate, B<sub>0</sub> must be increased for Configuration-101 and Configuration-102 relative to Configuration-100 at the same pressure-flowrate condition. Thus, the pressure-flowrate performance remains unchanged. Since the resistance of the coil-system was reduced by the grading, the increases in current were matched with a reduction in the applied voltage. Therefore, the resulting power draw remained roughly constant. Consequently, the efficiency performance remained unchanged.

Similar to the explanation given in the coil shifting results, it is likely that the coil shifting will have little impact on the pump performance due to the high operating frequency relative to the fluid velocity. During

the literature review, it was noted that the Finite Length Effect was most pronounced at frequencies which were comparable to the fluid velocity. However, the lowest mean slip measured was 50% meaning that the magnetic field velocity was at least twice that of the fluid velocity. Note that while the frequency of the pump can be adjusted to reduce the relative velocity, this will likely result in the pump being unable to produce enough pressure to match the system resistance. Therefore, it is concluded that the pump is simply too small to observe the Finite Length Effect and any changes in performance caused by the coil grading configurations.

## 3.5 CONCLUSIONS AND FUTURE WORK

To summarize, the pressure-flowrate and efficiency performance of a standard configuration ALIP was measured in sodium at 200 °C and 400 °C under applied voltages of 50 V<sub>rms</sub>, 75 V<sub>rms</sub>, 100 V<sub>rms</sub>, and 150 V<sub>rms</sub> and a frequency of 120 Hz. These measurements were compared to the analytical predictions evaluated under the same conditions. This comparison showed that the finite length has a significant impact on the performance of an ALIP. However, it is important to recognize that the fundamental ALIP theory neglects aspects of real ALIPs which may impact the predictions. For example, the analytic theory neglects the finite dimensions of the outer ferromagnetic core and coil assembly which has a strong impact on applied magnetic field distribution. Additionally, the analytic theory replaces the electric coils with an infinitely thing current sheet and assumes an infinite permeability and zero conductivity ferromagnetic core. This means that the magnetic field must be known. However, this is rarely the case as the field magnitude is a function of applied current which is also a function of the pump load. Moreover, accurate calculation of the input power is impossible using the infinite current sheet and infinite permeability core approximation. Therefore, this suggested that the ALIP theory would provide little insight into the effects of coil grading and coil shifting. Nevertheless, the ALIP theory in this form predicts the experimental pump performance characteristics with some great degree of accuracy given its simplicity and demonstrates the significant impact the finite length has on ALIP performance.

Next, the pressure-flowrate and efficiency performance of two coil shifting and two coil grading configurations was measured in sodium at 200 °C and under applied voltages of 50 V<sub>rms</sub>, 75 V<sub>rms</sub>, 100 V<sub>rms</sub>, and 150 V<sub>rms</sub> and a frequency of 120 Hz. These measurements were compared to the baseline performance measurements of the standard configuration pump evaluated under the same conditions. This comparison shows that all four configurations had either an insignificant impact on the total performance of the ALIP or marginally reduced the total efficiency. In the case of the coil shifting configurations, the shifted core effectively shortened the active length of the pump. Consequently, keeping the pump load constant requires a larger magnitude magnetic field. This requires additional current to be drawn, increasing the total power drawn, and therefore reducing the efficiency. It is likely that the reduction in efficiency is small due to the small size and current draw of the pump. In a larger pump, one may observe a more significant effect. However, this method results in a reduction of efficiency and is therefore deemed ineffective in address the finite length effect.

Like the coil shifting configurations, the coil grading configurations effectively shortened the active length of the pump. Therefore, keeping the pump load constant requires a larger magnitude magnetic field. This requires additional current to be drawn. However, since the number of turns in the coils is reduced the system resistance is reduced. Thus, the increase in current drawn is balanced by a decrease in applied voltage. Consequently, the efficiency remains constant compared to the baseline.

It is likely that the coil shifting and coil grading configurations had little impact on the pump performance due to the high operating frequency relative to the fluid velocity. During the literature review, it was noted that the Finite Length Effect was most pronounced as frequencies which were comparable to the fluid velocity. However, recall that the lowest mean slip was roughly 50% meaning that the magnetic field velocity was at least twice as large as a fluid velocity. While the frequency of the pump can be adjusted to

reduce the relative velocity, it is likely that the pump will be unable to produce enough pressure to match the system resistance. This can compensated by increasing the applied current. However, the maximum continuous pump current is only  $12 A_{rms}$ . Therefore, it is concluded that the pump is simply too small to observe the Finite Length Effect and any changes in performance caused by the coil shifting configuration.

From the unsuccessful results of coil shifting and coil grading, several paths have been identified for future work on the finite length effects of ALIPs. Firstly, it is clear that a detailed model must be constructed which accounts for effects like the finite dimensions of the stator core and coils as well as the finite core permeability. This will allow for direct comparisons between the coil shifting and coil grading results to theory. Additionally, the model may provide improved performance predictions over the fundamental theory discussed in this work. Secondly, a larger capacity ALIP may be needed in order to measure a significant change in efficiency for the coil shifting and coil grading configurations. This could be validated with the improved ALIP model discusses earlier.

# 4. PMIP PERFORMANCE CHARACTERTISTCS AND THE IMPACT OF THE FINITE WIDTH EDGE EFFECT

# 4.1 PMIP SPECIFICATIONS

Figure 4-1 shows the PMIP developed by M.G. Hvasta [16] which will be the focus on this work. This pump is a 12-Pole Double-Array Disc-Type PMIP developed driven at a 1:1 ratio by a 7.5 kW, 3-phase, 240 V electric motor with a maximum rotational speed of 188.5 rad/s. Relevant pump configuration data are given in Table 4-1 while relevant magnet data are given in Table 4-2. Note that the magnets are magnetized through their height.



Figure 4-1: An example of the 12-Pole Double-Array Disc-Type PMIP studied in this work.

Table 4-1: Relevant PMIP configuration data.

Tubie 4-1. Keievani I MII Conjiguration auta.					
Property	Symbol	Value	Units		
Array Spacing	hg	3.37	ст		
Average Flow Channel Radius	$R_{avg}$	12	ст		
Flow Channel Width	2 · b	5	cm		
Flow Channel Height	$h_{ch}$	6.35	mm		
Wall Material	-	316/316L-SS	-		
Wall Thickness	$h_{\mathbf{w}}$	2.54	mm		
Effective Length	$L_e = \pi R_{avg}$	38	cm		

Table 4-2: Relevant PMIP magnet data	l.
--------------------------------------	----

Property	Symbol	Value	Units
Magnet Type	-	SmCo	-
Residual Magnetism	$B_{\mathbf{r}}$	1.08	T
Width x Length x Height	$M \times N \times T$	2.5 x 2.5 x 5	$cm \ x \ cm \ x \ cm$
Number of Magnets	n <sub>mag</sub>	12	-
Pole-Pitch	$\tau_{\rm B} = 2\pi R_{\rm avg}/n_{\rm mag}$	16	ст
Yoke Material	-	Carbon Steel	-
Peak Magnitude	$B_0$	3.1	kG

# 4.2 EXPERIMENTAL SETUP

# **4.2.1** Facility Overview

Experimental PMIP measurements were completed in one of UW-Madison's three sodium test facilities. The PMIP Test Facility shown in Figure 4-2 was constructed for materials corrosion studies, testing liquid metal flow components, and impurity measurement and control instrumentation. Several modifications were made to accommodate pump testing such as the addition of a Vortex Shedding flowmeter, high temperature differential pressure transducers, a throttle, and a torque sensor.

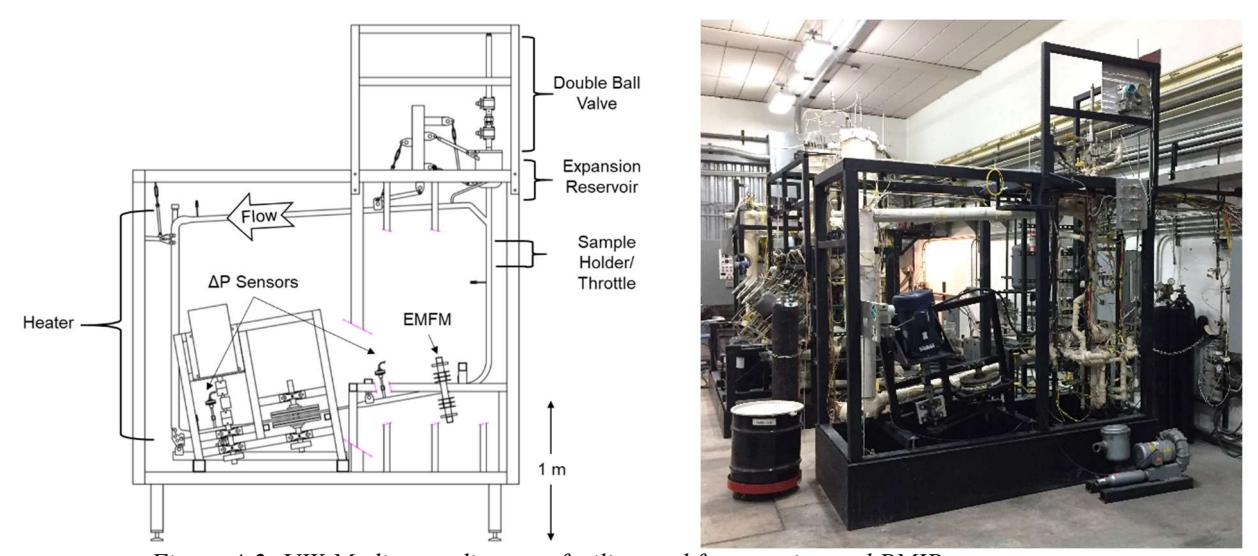


Figure 4-2: UW-Madison sodium test facility used for experimental PMIP measurements.

## 4.2.2 Flowrate Measurement

Primary flowrate measurements were made with a calibrated Electromagnetic Flowmeter (EMFM). Figure 4-3 show the PMIP-EMFM used in this work. An EMFM measures flowrate by measuring the voltage

induced by an electrically conductive fluid passing through a stationary magnetic field. Note that a magnetic field oriented perpendicular to the fluid velocity will induce a mutually orthogonal voltage that can be measured by a pair of externally mounted electrodes. Table 4-3 lists the specifications of the PMIP-EMFM used in this work.



Figure 4-3: Photo of the PMIP-EMFM used for primary flowrate measurements.

Table 4-3: Additional specifications of the PMIP-EMFM used to measure volumetric flowrates in this work.

Quantity	Value	Units
Туре	NdFeB	-
Grade	N42	-
Dimensions	$5 \times 5 \times 5$	cm
Spacing	11.7	cm
$d_i$	2.66	cm
$D_{o}$	3.34	cm
Material	316/316L	-

Like the ALIP-EMFM discussed in earlier, the PMIP-EMFM used in this work follows the same principles. Similarly, the ALIP-EMFM and PMIP-EMFM were calibrated using a Vortex Shedding flowmeter.

Therefore, the reader is referred to Section 3.2.3 for more details on the theory of EMFM operation and the calibration procedure.

Prior to performance measurements, the PMIP-EMFM was calibrated against a Foxboro model M83 vortex shedding flowmeter. Figure 4-4 plots the predicted EMFM flowrate as a function of reference flowrates at 200 °C and 400 °C. From these data, a linear regression analysis was used to find correlation coefficients P<sub>0</sub> and P<sub>1</sub> using the model in Equation 4-1. Table 4-4 presents the calculated coefficients, their standard errors, and the correlation coefficient.

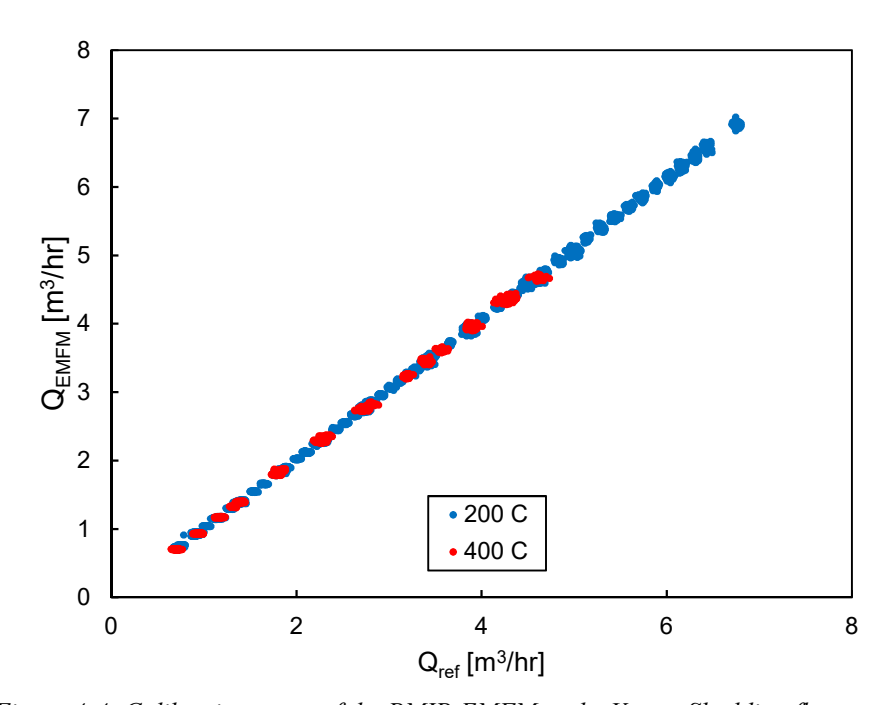


Figure 4-4: Calibration curve of the PMIP-EMFM to the Vortex Shedding flowmeter.

$$\begin{aligned} \mathbf{Q}_{\mathrm{EMFM}} &= \mathbf{P}_0 + \mathbf{P}_1 \cdot \mathbf{Q}_{\mathrm{ref}} \\ & Equation \ 4\text{-}1 \end{aligned}$$

Table 4-4: PMIP-EMFM correlation coefficients, their associated standard errors, and the correlation coefficient.

<b>Quantity</b>	Value	Units
$P_0$	-0.0248	m³/hr
$P_1$	1.0223	-
$S.E.(P_0)$	0.00078	$m^3/hr$
S.E.( P <sub>1</sub> )	0.00025	-
r	0.9998	-

A total PMIP-EMFM calibration error was estimated using the Law of Propagation of Uncertainty for correlated quantities as described in the Guide to the Expression of Uncertainty Measurement [57]. This method estimates the total uncertainty using the standard errors of the correlation coefficients A<sub>0</sub> and A<sub>1</sub> and EMFM measurement error. The PMIP-EMFM measurement error was estimated by analytically propagating uncertainties through Equation 2-80 using the general law of uncertainty propagation for uncorrelated quantities. Table 4-5 presents the estimated uncertainties of the primary measurements used in this analysis.

Table 4-5: Estimated uncertaintities of the primary EMFM measurements

Quantity	Value	Units
$d_i$	0.0508	mm
$D_{o}$	0.0508	mm
$T_{mag}$	1	$^{o}C$
$T_{Na}$	0.5	$^{o}C$
$\Delta V_{EMFM}$	$\sqrt{(0.001 * \Delta V_{EMFM})^2 + (15)^2}$	$\mu - V$

Figure 4-5 plots the analytically calculated PMIP-EMFM measurement error. Also plotted are the experimental calibration residuals. Note that the estimated measurement error follows a similar trend and magnitude as the calibration residuals. From Figure 4-5, the total PMIP-EMFM calibration error was divided over two flow ranges: over the range  $0.9 \, \text{m}^3/\text{hr} \le Q < 2 \, \text{m}^3/\text{hr}$  the total error is taken as 2% the measured flowrate. Over the range  $2 \, \text{m}^3/\text{hr} \le Q \le 7 \, \text{m}^3/\text{hr}$  the total error is taken as 0.75% the measured flowrate.

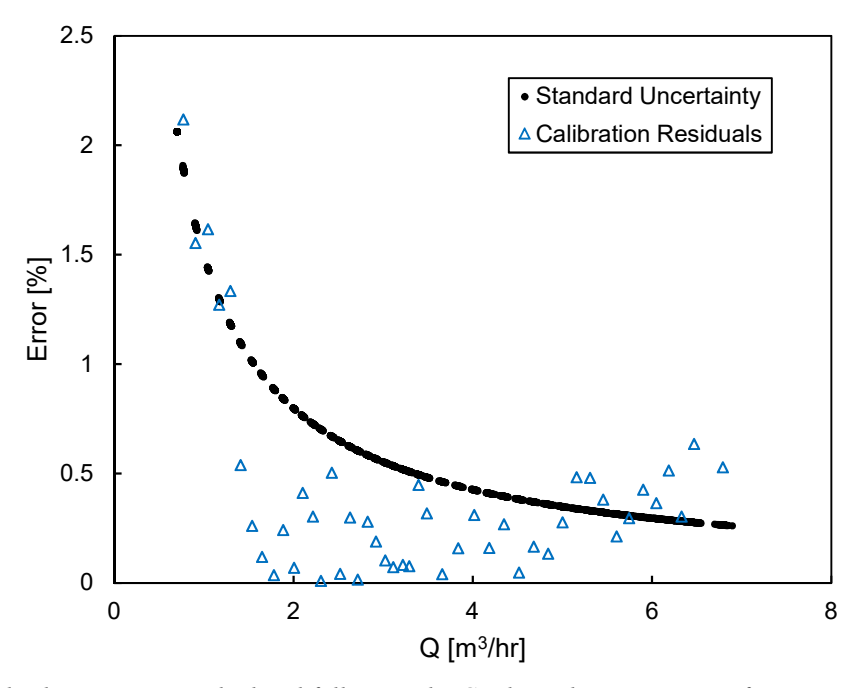


Figure 4-5: Standard Uncertainty calculated following the Guide to the Expression of Uncertainty in Measurement standard compared to the calculated calibration residuals. As a conservative estimate, the flowmeter error is taken as 2% the measured flowrate over the range  $0.9 \, \text{m}^3/\text{hr} \leq Q < 2 \, \text{m}^3/\text{hr}$  and 0.75% the measured flowrate over the range  $2 \, \text{m}^3/\text{hr} \leq Q \leq 7 \, \text{m}^3/\text{hr}$ .

#### 4.2.3 Pressure Measurement

Differential pressures across the pump channel were measured using a Yokogawa EJA110E differential pressure transmitter with a 5 to 500 kPa measurement span. Fitted to the transmitter were a pair of high-temperature NaK-filled diaphragms which acted as a thermal barrier for the transmitter. Given a span of 500 kPa, the manufacturer specifies an accuracy of  $\pm 70$  Pa. However, the thermal stand-off induced additional measurement errors. This error was estimated by noting the variance in zero-flowrate readings recorded throughout testing which were found to drift by up to  $\pm 750$  Pa. Thus, this variance was taken as the pressure measurement error as a conservative estimate.

Figure 4-6 shows the relative position of the pressure transducers for pressure-flowrate measurements  $\Delta p$ , system frictional loss measurements  $p_{loss,sys}$ , the channel pressure loss measurements  $p_{loss,chan}$ , and some relevant PMIP channel dimensions. Note that any height-induced pressures were recorded at several zero-flowrate conditions and subsequently offset from the final pressure measurements. Due to space constraints,

 $p_{loss,chan}$  was measured at a different location than  $\Delta p$  and  $p_{loss,sys}$ . These additional frictional pressure losses were left unaccounted.

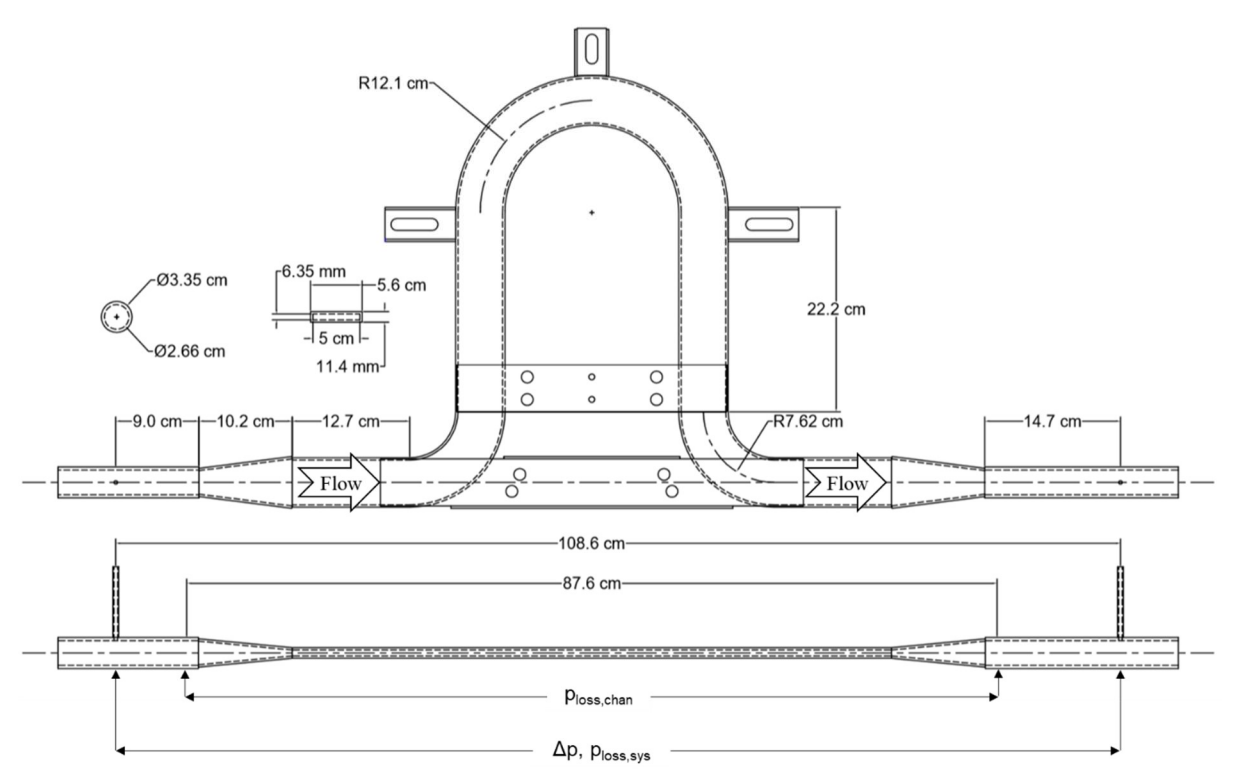


Figure 4-6: Location of differential pressure measurement for the channel frictional losses  $\Delta p_{loss,chan}$  and developed pressure  $\Delta p$  and system loss  $p_{loss,sys}$  testing. Note that any height-induced pressures were recorded at several zero-flowrate conditions and subsequently offset from the final pressure measurements. Due to space constraints,  $\Delta p_{loss,chan}$  was measured at a different location than  $\Delta p$  and  $\Delta p_{loss,sys}$ .

## 4.2.4 Power Measurement

Pump power was calculated by measuring the torque and speed using an Interface T4-50 Torque Sensor. Figure 4-7 shows a sketch of the sensor installed directly into the PMIP drive train. This method of power measurement avoided including the electric motor efficiency which can vary greatly as a function of applied torque and speed.

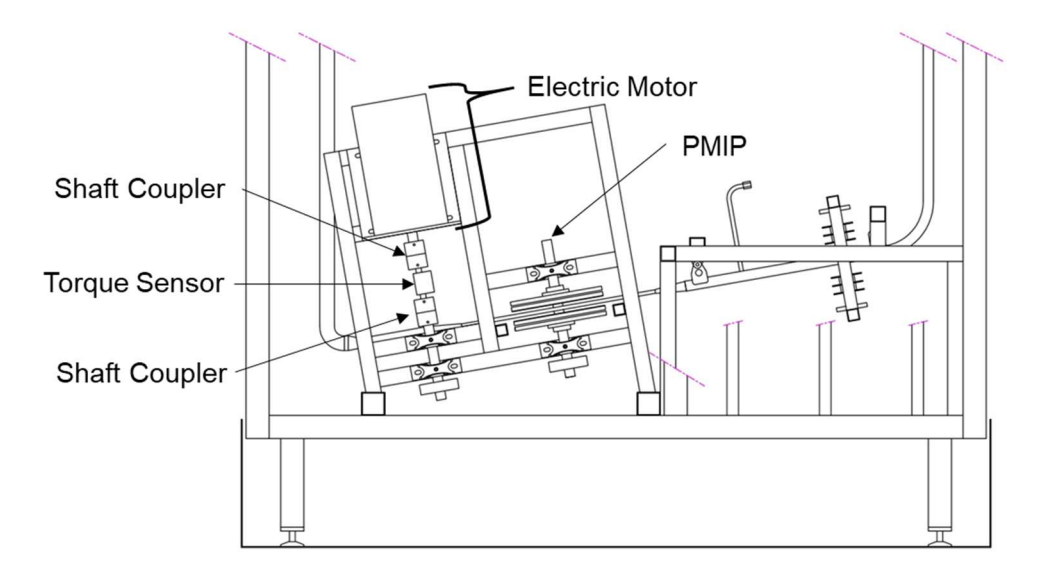


Figure 4-7: Sketch of the experimental PMIP with the installed torque sensor.

Equation 4-2 was used to calculate the total PMIP power using the experimentally measured torque  $\tau$  and rotation speed of the disc  $\omega_{PMIP}$ . The sensor is reported to have a torque measurement error of  $\pm 0.1$  N-m and a speed measurement error of  $\pm 0.1571$  rad/s.

$$W_{in} = \tau \cdot \omega_{PMIP}$$
  
Equation 4-2

# 4.3 EXPERIMENTAL MEASUREMENTS

## 4.3.1 Radial Magnetic Field Distribution

As discussed in the theoretical section, the uniformity of this distribution greatly impact the pump performance through the attenuation factor  $K_{at,2}$ . Therefore, radial magnetic field distributions were characterized at several channel heights using an F.W. Bell 3051 Gauss Meter with a relative measurement error of 3%. Previous work has shown that the magnitude of the applied magnetic field,  $B_{e,y}(x)$  in Equation 2-60 can be approximated by the cosine function in Equation 2-70 across the pump width  $2 \cdot b$  [15] [16]. Recall that the uniformity of the magnetic field across the pump width is characterized by the shape-factor  $\Gamma$ . In theory, this shape-factor is bounded by  $0 \le \Gamma \le \pi/(2 \cdot b)$ . At the lower bound,  $\Gamma = 0$  represents a uniformly applied field across the pump width. At the upper bound,  $\Gamma = \pi/(2 \cdot b)$  represents an applied

field that is zero at  $\pm b$ . The shape factor  $\Gamma$  is a direct result of the finite magnet dimensions. Therefore, it is important to note that both upper and lower bounds are impossible for permanent magnets of a finite width.

To determine the shape factor  $\Gamma$ ,  $B_{e,y}(x)$  was measured as a function of channel width  $2 \cdot b$  at several heights y using a Gauss Meter. Figure 4-8 presents the resulting profiles. Note that the dashed vertical lines represent the boundary of the pump channel with negative values directed toward the magnet array axis of rotation.

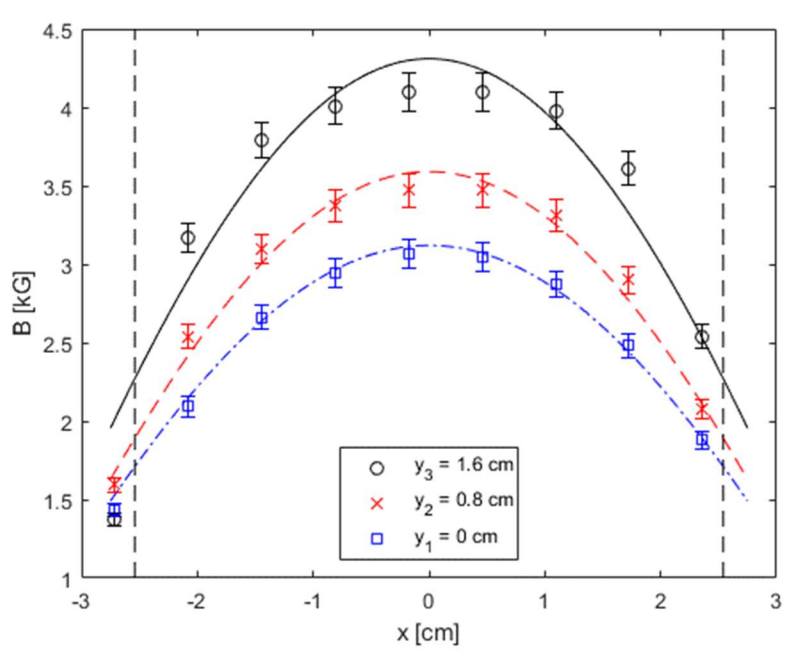


Figure 4-8: Experimental measurements of the applied magnetic field peak amplitude  $B_{e,y}(x)$  as a function of pump width at several heights  $y_i$ . Note that the x-coordinate is centered on the pump channel with negative values directed towards the magnet array's axis of rotation. The dashed vertical lines represent the pump width. Also plotted is Equation 4-3 using the values presented in Table 4-6.

Equation 4-3 was used to model the data from Figure 4-8 where  $B_0(y_i)$  is the peak magnitude at a given height  $y_i$  and  $\Gamma_i$  is the corresponding shape factor. Table 4-6 reports the coefficients found using a linear least squares approach.

$$B_{e}(x, y_{i}) = B_{0}(y_{i}) \cdot \cos(\Gamma_{i} x)$$

Equation 4-3

Table 4-6: Coefficients for the PMIP's applied magnetic field profile across the channel width.

$\mathbf{y_i}$	$\mathbf{B_0}(\mathbf{y})$	$\Gamma_{\mathbf{i}}$
ст	kG	1/cm
0	3.12	0.39
0.8	3.59	0.40
1.6	4.31	0.40

Figure 4-8 shows that the magnetic field profiles are nearly symmetric about x=0 cm. This result supports the assumption that radial effects can be neglected in the analytical theory for this particular PMIP configuration. Additionally, Figure 4-8 shows that near  $y_i=0$  cm, the cosine function in Equation 4-3 accurately models the magnetic field profile. However, at larger heights the cosine function becomes less accurate. For the PMIP in this configuration with a channel half-height  $h_{ch}/2=0.3175$  cm, Figure 4-8 suggests that cosine model is an appropriate approximation.

## 4.3.2 Frictional Pressure Losses

Frictional pressure losses in the PMIP channel and test system were measured in 200 °C and 400 °C sodium. Figure 4-9 and Figure 4-10 presents the frictional pressure loss curve for the PMIP channel  $p_{loss,chan}$  and experimental system  $p_{loss,sys}$ , respectively. Note that in the flow range tested, a single curve characterizing  $p_{loss,chan}$  was assumed following the model in Equation 4-4. Two separate curves were generated for  $p_{loss,sys}$  also following the model in Equation 4-4. A linear regression analysis was used to find coefficients  $p_{loss,sys}$  and  $p_{loss}$  for all three loss curves. Table 4-7 presents the resulting coefficients, their standard errors, and the correlation coefficient.

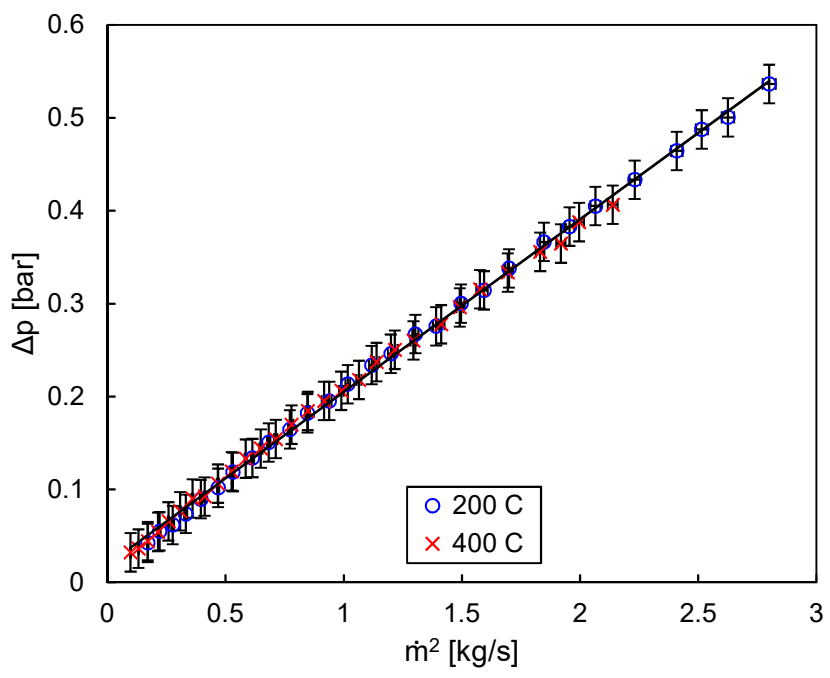


Figure 4-9: PMIP channel pressure loss measurements as a function of mass flowrate at 200 °C and 400 °C. A single curve was fitted using the model in Equation 4-4 with the resulting coefficients and standard errors presented in Table 4-7.

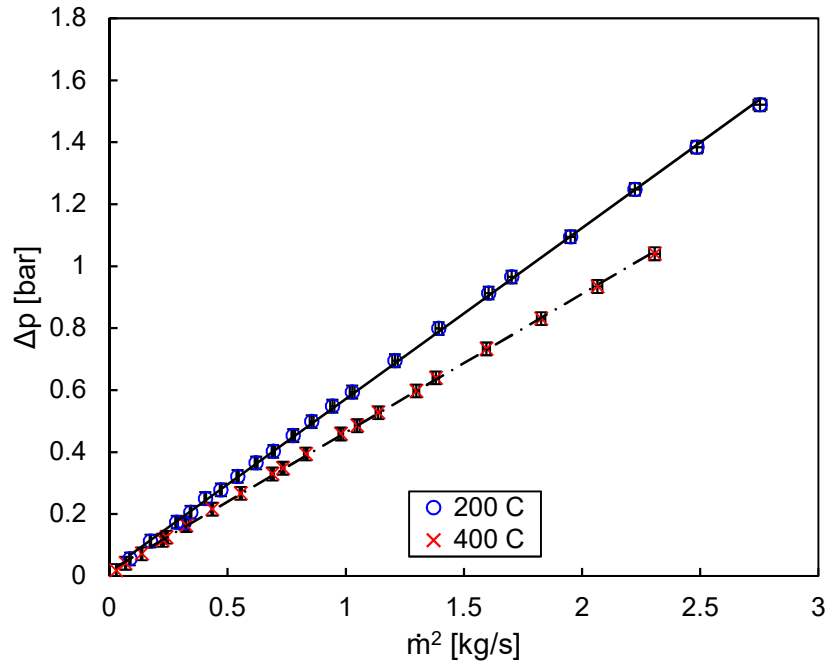


Figure 4-10: Frictional pressure losses in the PMIP test system as a function of mass flowrate at 200 °C and 400 °C.

$$\begin{array}{c} p_{loss} = D_0 + D_1 \cdot \dot{m}^2 \\ \textit{Equation 4-4} \end{array}$$

Table 4-7: PMI	P channel ar	nd system pressure	e loss coefficients, i	their standard	errors, and	the correlation	coefficient.

	$D_0$	$D_1$	S.E.( $D_0$ )	S.E.( $D_1$ )	r
	bar	bar-s²/kg²	bar	bar-s²/kg²	-
Channel Losses	0.0112	0.1858	0.0009	0.0012	0.9994
200 °C System Losses	0.0197	0.5519	0.0032	0.0012	1
400 °C System Losses	0.0162	0.4472	0.0019	0.0017	1

## 4.3.3 Resistive Heating Losses

Input power was measured in a dry PMIP at several frequencies to characterize the resistive heating and other losses. Theoretical analysis identified resistive heating in both the fluid and the channel walls as a major component of the total energy balance. These losses were experimentally estimated by measuring the pump input power without sodium. Note that the pump channel has no external heaters or coolers to control temperature; the final temperature is a result of induction heating and parasitic losses. Therefore, the steady-state temperature was recorded as a function of magnet frequency and used to correct the theoretical electrical conductivity. Figure 4-11 plots the resulting temperatures and the curve used to correct for wall temperature.

Figure 4-12 plots the experimentally measured PMIP input power for a dry pump. Using the data from Figure 4-11, the resistive heating losses were analytically calculated using Equation 2-76 and compared to the experimental measurements in Figure 4-12. Note that the theory using  $K_{at,2}$  produces an accurate estimate of the resistive heating in the pump walls. However, recognize that the theory produces artificially lower estimates since it neglects the channel sidewalls, frictional losses, windage losses from the rotating magnet arrays, pullies, and belt, as well as other losses. These factors would tend to increase the analytically calculated losses. Nevertheless, the results from Figure 4-12 show that the analytic theory is consistent with experimental measurements.

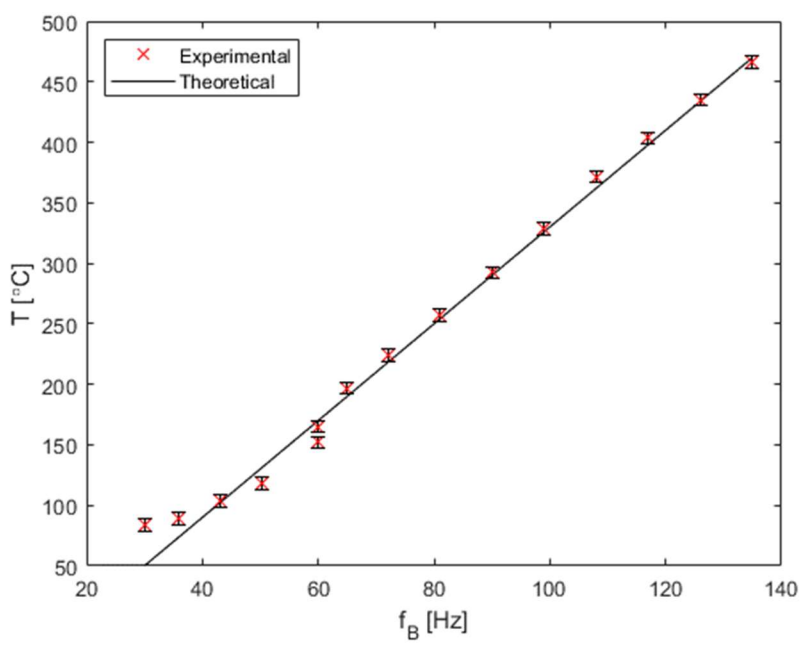


Figure 4-11: PMIP wall temperature as a function of magnetic frequency for the dry pump resistive heating loss measurements. Note the temperature was a result from inductive heating and parasitic losses; no heaters or coolers were used to control the temperature.

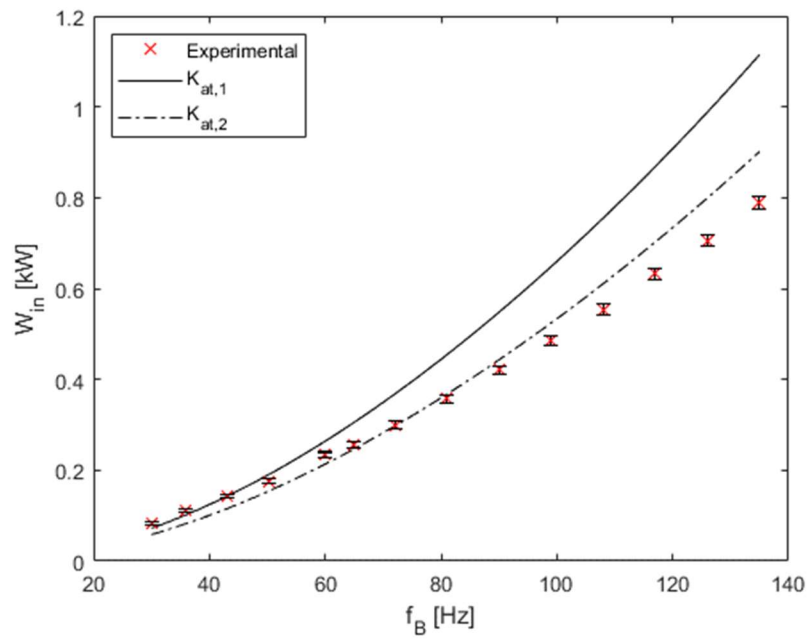


Figure 4-12: Experimentally measured PMIP input power compared to the analytically calculated resistive heating losses in the channel walls. Note that the analytic theory neglects the channel sidewalls, frictional losses in the bearings, windage losses from the rotating magnet arrays, pullies, and belt, as well as other losses. These factors would therefore tend to increase the analytically calculated term.

# 4.3.4 Pressure-Flowrate

PMIP pressure-flowrate curves were measured in sodium at 200 °C and 400 °C. Figure 4-13 plots the curves at magnet frequencies of 30 Hz, 60 Hz, 75 Hz, and 90 Hz. During these tests, the magnet frequency was held constant and the flowrate was varied by a throttle. Note that the pump was tested in an envelope with the lower bound restricted by the PMIP-EMFM calibration and the upper bound restricted by the system loss curves. Figure 4-14 plots the PMIP pressure output as a function of slip under the same conditions. In contrast to typical centrifugal pressure-flowrate curves, the PMIP curves are nearly linear due to the relatively small frictional pressure losses in the pump channel.

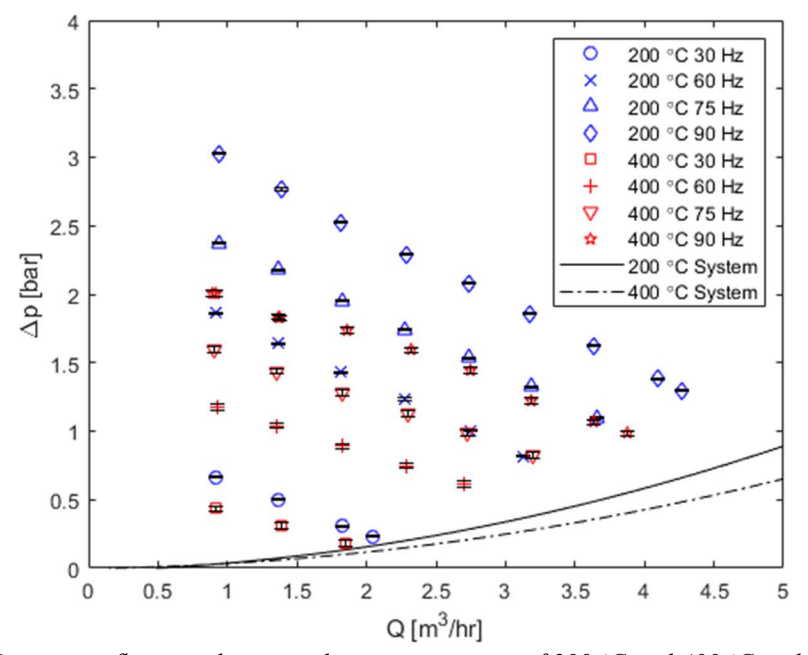


Figure 4-13: PMIP pressure-flowrate data at sodium temperatures of 200 °C and 400 °C and magnet frequencies of 30 Hz, 60 Hz, 75 Hz and 90 Hz. The pump pressures were measured in an envelope with the lower flowrate bound restricted by the PMIP-EMFM calibration and the upper flowrate bound restricted by the system loss curves.

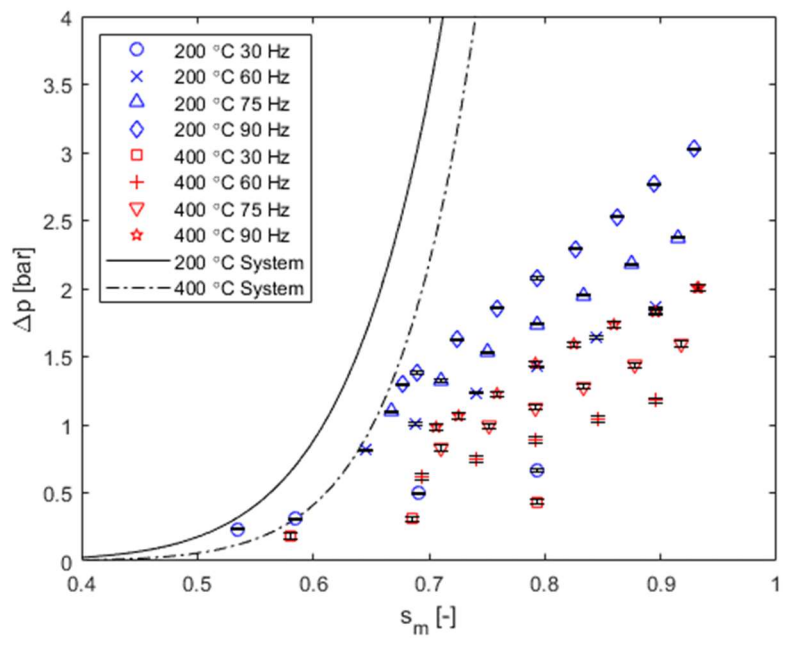


Figure 4-14: PMIP pressure-slip data at sodium temperature of 200 °C and 400 °C and magnet frequencies of 30 Hz, 60 Hz, 75 Hz and 90 Hz. The pump pressures were measured in an envelope with the lower slip bound restricted by the system loss curves and the upper slip bound restricted by the EMFM calibration.

# 4.3.5 Efficiency

Pump torque and speed were measured concurrently at each pressure-flowrate condition. Equation 4-5 was used to define the pump efficiency from these measurements. Figure 4-15 plots the experimental efficiency measurements at as a function of mean-slip at magnet frequencies of 30 Hz, 60 Hz, 75 Hz, and 90 Hz at 200 °C and 400 °C. During these tests, the magnet frequency was held constant and the flowrate was varied by a throttle. Note that the efficiencies below means slips of 65% are the system loss measurements. The maximum pump efficiency occurred at 70% mean slip and was measured as 14% and 11.5% at 200 °C and 400 °C, respectively.

$$\eta = \frac{W_{out}}{W_{in}} = \frac{\Delta p \cdot Q}{\tau \cdot \omega_{PMIP}}$$
 Equation 4-5

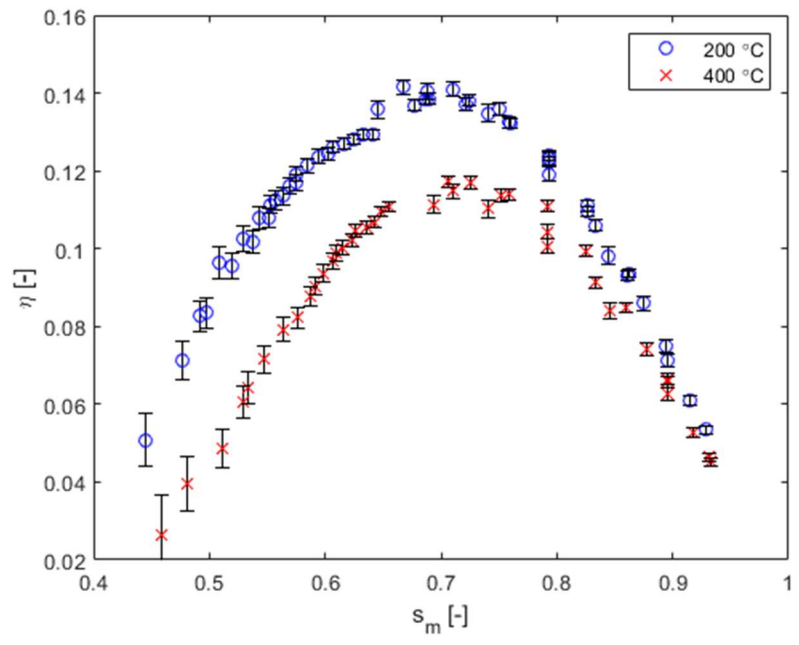


Figure 4-15: PMIP efficiency-slip data at sodium temperatures of 200 °C and 400 °C under magnetic field frequencies of 30 Hz, 60 Hz, 75 Hz, and 90 Hz. Note that the data plotted as mean-slips less than 0.7 are the system loss curves.

## 4.4 EFFECT OF THE FINITE WIDTH

To gain additional insights into PMIP performance characteristics, the experimental pressure-flowrate and efficiency-mean slip data are compared to the analytic theory discussed earlier. However, direct comparisons require the transformation of the experimental data. Recall from PMIP theory that the calculated pressure  $p_{EM}$  is the total maximum developed by the pump. However, the experimentally measured pressure  $\Delta p$  will include frictional pressure losses in the pump channel and the test system. Therefore,  $p_{EM}$  and  $\Delta p$  and related by Equation 4-6 where  $p_{EM,exp}$  is the experimentally measured maximum developed pressure,  $p_{loss,chan}$  are the pump channel pressure losses, and  $p_{loss,sys}$  are the pressure losses in the experimental system.

$$p_{\rm EM,exp} = \Delta p + p_{\rm loss,chan} + p_{\rm loss,sys}$$
Equation 4-6

This new pressure definition is used in Equation 4-7 defining a new efficiency calculation. Here,  $p_{\text{max,exp}}$  is used instead of  $\Delta p$  as was done in Equation 4-4. This new definition allows for direct comparison of the analytical calculated efficiencies using Equation 2-80.

$$\eta_{\text{EM,exp}} = \frac{p_{\text{EM,exp}} \cdot Q}{\tau \cdot \omega_{\text{PMIP}}}$$
Equation 4-7

Lastly, recall that Equation 4-8 was used to calculate the theoretical maximum developed pump pressure. Note that  $p_{EM}$  is directly proportional to the relative velocity ( $U_B - U_0$ ) by a constant C. Additionally, recall from PMIP theory that Equation 2-69 defined an important non-dimensional parameter. This parameter was called the effective Magnet Reynolds number which describes the relative magnitudes of magnetic diffusion to magnetic induction. Note that the definition in Equation 2-69 neglects the non-magnetic gap, which can be large for the Double-Array Disc-Type PMIP. Therefore,  $Rm_f \cdot s_m$  is rescaled in Equation 4-9 where  $h_{ch}$  is the channel height and  $h_{gap}$  is the non-magnetic gap height [59]. Note that  $Rm_f \cdot s_m$  is also directly proportional to the relative velocity by a constant D. Thus, it is expected that  $p_{EM}$  will be linearly proportional to  $Rm_f \cdot s_m$  which can be interpreted as a non-dimensional flowrate or magnet frequency. Thus, the transformed data will be plotted against this non-dimensional parameter.

$$p_{EM} = \frac{1}{2}\sigma_{f}L_{e}(U_{B} - U_{0}) B_{0}^{2} K_{at,(1,2)} = C \cdot (U_{B} - U_{0})$$
Equation 4-8

$$Rm_f \cdot s_m = \frac{\mu_f \sigma_f}{k_0} \frac{h_{ch}}{h_{gap}} U_B \cdot s_m = D \cdot (U_B - U_0)$$
Equation 4-9

The experimental pressure data were transformed and compared to PMIP theory evaluated at the same conditions. Figure 4-14 and Figure 4-15 plot these data under constant flowrate conditions at 200 °C and 400 °C, respectively. Constant flowrate data were plotted with variable frequency since it allowed

measurement of  $p_{EM,exp}$  over a larger range of  $Rm_f \cdot s_m$  at a given condition. Note that under these conditions,  $Rm_f \cdot s_m$  will increase proportionally with magnet frequency.

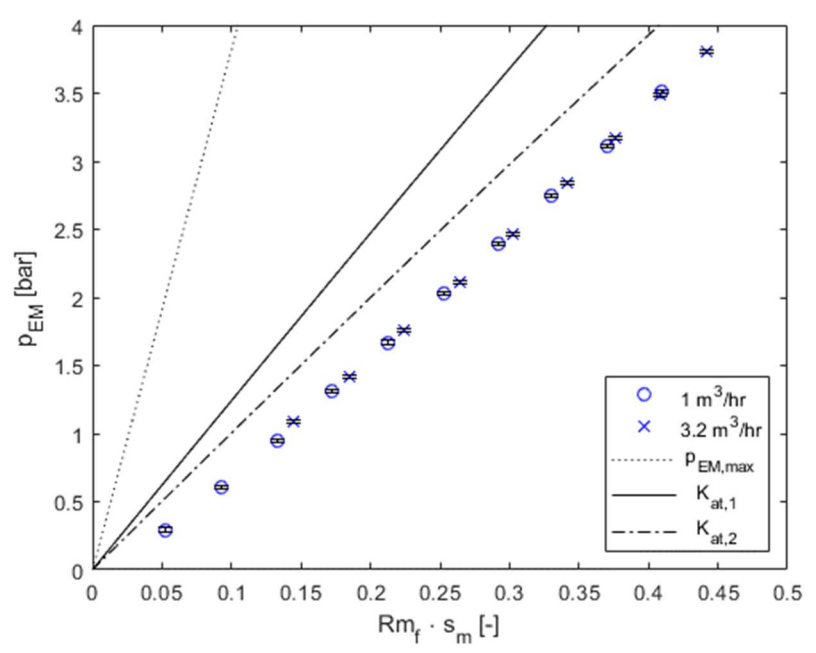


Figure 4-16: Plot of the maximum output pressure as a function of  $Rm_f \cdot s_m$  at 200 °C under constant fluid flowrates of 1  $m^3/hr$  and 3.2  $m^3/hr$ .

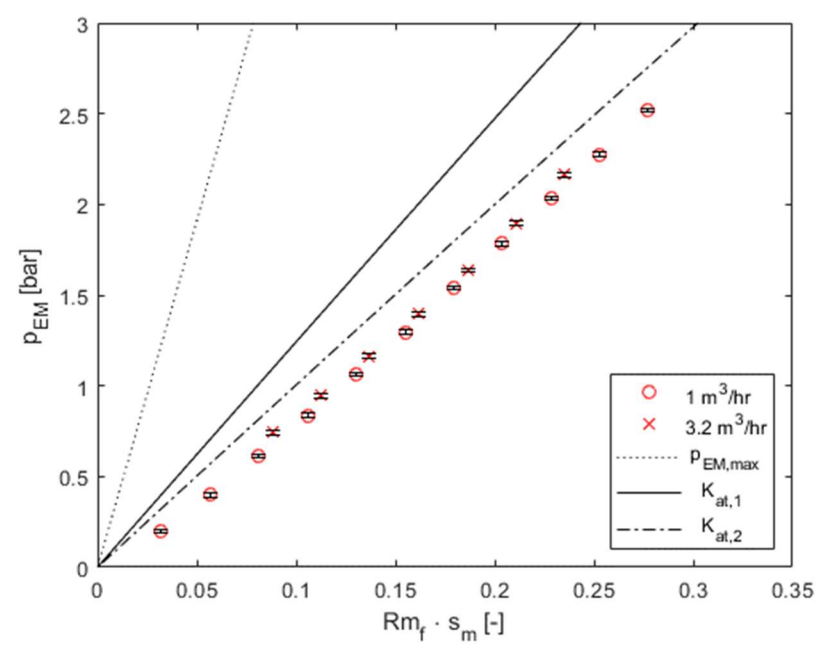


Figure 4-17: Plot of the maximum output pressure as a function of  $Rm_f \cdot s_m$  at 400 °C under constant fluid flowrates of 1  $m^3$ /hr and 3.2  $m^3$ /hr.

Figure 4-14 and Figure 4-15 show that the pressure-flowrate curves from Figure 4-13 collapse into a single  $p_{EM,exp}$  curve which is linear with  $Rm_f \cdot s_m$  over the range of measured flowrates. Additionally, as expected by theory the experimental curves approximately cross the origin. Inaccuracies in this crossing are likely due to errors in the pressure loss correlations at very low flowrates and magnet frequencies. Additionally, these results show the significant impact finite duct have on the pump's pressure performance. Moreover, since  $K_{at,2}$  provides a more accurate prediction of  $p_{EM}$  than  $K_{at,1}$ , this also demonstrates the significant impact radial-magnetic field uniformity has on the pressure output. Therefore, maximizing pressure output requires careful consideration of both channel and magnet geometry.

Next, the experimental efficiency data were transformed and compared to PMIP theory evaluated at the same conditions. Figure 4-18 and Figure 4-19 plot these data under constant frequency conditions at 200 °C and 400 °C, respectively. Note that these data were collected in the same envelope as described earlier where the solid points represent the system frictional pressure losses. For simplicity, only the theory using  $K_{at,1}$  is plotted as under these conditions the calculated efficiency  $K_{at,2}$  varied little from  $K_{at,1}$  as a function of  $Rm_f \cdot s_m$ .

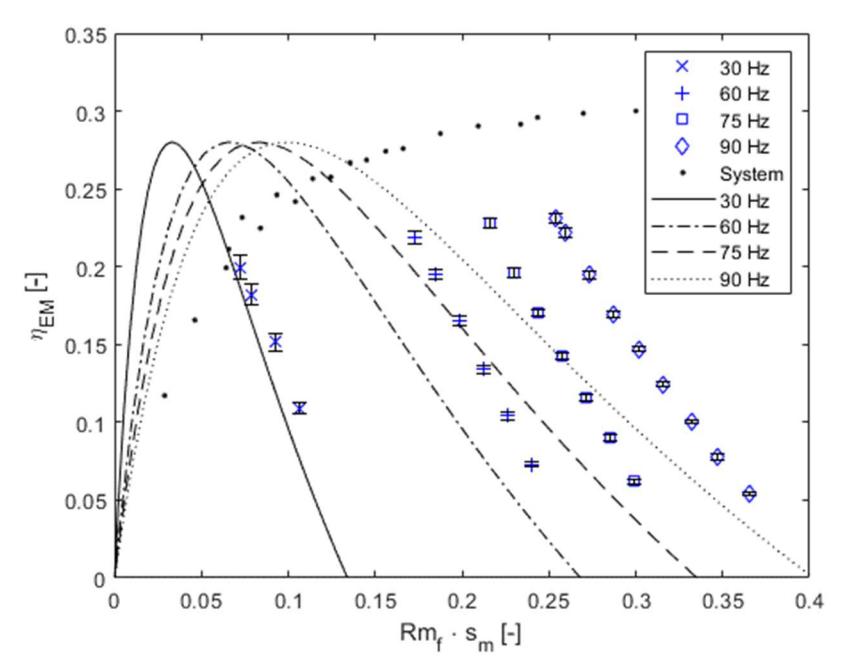


Figure 4-18: Plot of pump efficiency as a function of  $Rm_f \cdot s_m$  at 200 °C under constant frequency conditions. Note that the theoretical efficiencies are calculated using only using the  $K_{at,1}$ .

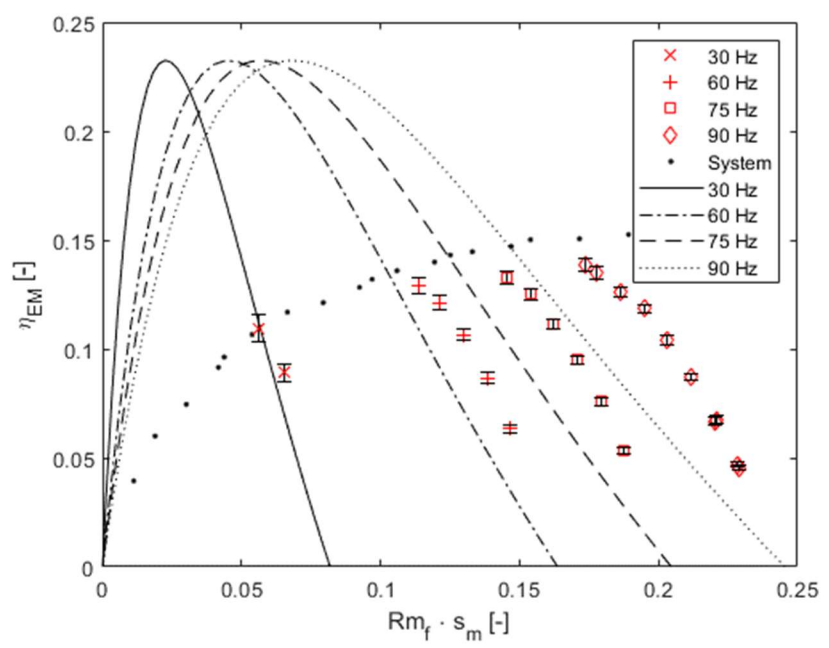


Figure 4-19: Plot of pump efficiency as a function of  $Rm_f \cdot s_m$  at 400 °C under constant frequency conditions. Note that the theoretical efficiencies are calculated using only using the  $K_{at,1}$ .

Figure 4-18 and Figure 4-19 show that the efficiency curves from Figure 4-15 vary with magnet frequency as a function of  $Rm_f \cdot s_m$ . Note that the maximum pump efficiency at a given frequency is roughly constant

as expected by theory. Additionally, the mean-slip at the point of maximum efficiency increases with increasing magnet frequency. However, the pump envelope limits full measurement of each efficiency curve and it therefore is difficult to conclude whether the maximum efficiency is constant with frequency. These results seem to suggest the theoretical accuracy is improved at low magnet frequencies. However, this may be artificially induced by inaccuracies in the pressure loss correlations at low pump frequencies that were discussed earlier.

Finally, it is important to note that the theoretical predictions neglect several factors which may influence the maximum pressure output and pump efficiency. Firstly, the theory neglects the channel sidewalls. MHD channel flow [44] and numerical EMIP models [45] show that the sidewall conductivity and thickness are important in determining the current distribution in the pump channel. This effect will ultimately impact the maximum pressure output, resistive heating losses in both the fluid and channel, and the total pump efficiency. Therefore, further insights into PMIP performance may be improved by developing an analytic correction factor or a numerical model which accounts for the finite conductivity of the channel sidewalls.

Secondly, the theory neglects entrance and exit effects. It has been noted that the effective pump length maybe be significantly under-estimated by ignoring these regions [28]. Overall, this would have the effect of increasing the predicted pump output pressure. However, little work exists which investigates the inlet and outlet regions to quantify their impact on the total pump performance. At the time of this writing, it is unclear whether these regions will have a net positive or negative effect on the theoretically calculated pump performance. Therefore, additional insights into PMIP performance may be enhanced by considering these regions in future analytic expressions or a numerical models.

Overall, the analytic theory in this form predicts the experimental pump performance characteristics with a great degree of accuracy given its simplicity. The experimental data, coupled with the analytic PMIP theory, show that the finite dimensions of the channel and magnets strongly impact PMIP performance. These

effects will be magnified in PMIPs applied to fluids with small electrical conductivities than sodium such a gallium and lead. Therefore, the effects of pump and magnet width must be careful considered for a given application.

#### 4.5 CONCLUSIONS AND FUTURE WORK

To summarize, the pressure-flowrate and efficiency performance of a 12-pole Double-Array Disc-Type PMIP was characterized in sodium at 200 °C and 400 °C under 30 Hz, 60 Hz, 75 Hz, and 90 Hz. Previously, few works have characterized the pressure-flowrate and efficiency performance of this particular PMIP configuration. In additional, three additional key PMIP performance parameters were characterized. Firstly, the PMIP magnetic field was characterized and shown to approximately follow a cosine across the centerline channel width. Moreover, at small channel heights the magnetic field was observed to vary little which supports the averaging assuming. Secondly, the frictional pressure losses in the PMIP channel were characterized in 200 °C and 400 °C sodium. Lastly, the dry-pump input power was measured and analytic theory was found to predict the input power closely.

Next, analytic PMIP theory accounting for the finite channel width and finite magnet width was validated with experimental measurements. Despite its simplicity, the analytic theory was found to reasonable predict the pressure-flowrate and efficiency performance. Moreover, the theory suggests that the finite dimensions of the channel and magnets have a significant impact on the total performance of a PMIP. Overall, this work produced several key experimental characterization of the experimental PMIP. Additionally, the analytic PMIP theory was validated and found to model the pump with reasonable accuracy.

While overall the results were successful, several paths have been identified for future work on the finite width effect of PMIPs. Firstly, literature showed that the finite conductivity channel walls will have an important part in determining the PMIP current distributions. While an analytic solution may be difficult,

a numerical Finite Element Analysis (FEA) model will provide additional insight to the finite width effect. Moreover, a FEA model could even obtain some fluid dynamic effects which were ignored in the analytic theory. In total, this may produce even more accurate predictions of PMIP performance characteristics than the simple analytical calculations. Secondly, with consideration of the channel walls there is an opportunity to optimize the 12-Pole Double-Array Disc-Type PMIP. For example, while small channel walls will minimize their resistive heating losses, a wide channel side-wall with narrow magnets may produce a more optimized pump with respect to efficiency.

#### 5. SUMMARY OF CONCLUSIONS AND RECCOMENDED FUTURE WORK

## 5.1 SUMMARY OF ALIP CONCLUSIONS AND FUTUE WORK

In total, this work characterized several ALIP parameters. Firstly, the frictional losses in the ALIP channel were characterized using water. Water was used due to limitations of installing the ALIP into a secondary sodium system. Additionally, the losses were only measured at a single water temperature and pressure due to the limitations of the water test system. Nevertheless, these results were used with an annular channel pressure loss correlation to define an effective ALIP channel length. This effective length was used in the same annular channel pressure loss correlation evaluated with sodium properties. While less than ideal, this provided an estimate to the expected pressure losses in the pump channel.

Secondly, dry-pump power was measured to estimate the resistive heating losses in the channel walls. Theoretical predictions were found to be in agreeance with the experimental results. However, it was recognized that the theory produces artificially lower estimates since it neglects the pump cores, resistive heating losses in the coils, as well as others. These factors would tend to increase the analytically calculated losses.

Thirdly, the axial distribution of the magnetic field's radial component was characterized in air for all pump configurations. These results showed that the coil shifting and coil grading configurations produce similar tapered magnetic field profiles near the inlet and outlet of the pump. Additionally, these results show that the applied field is highly non-uniform which suggested that the finite dimensions of the ferromagnetic core and coils may need to be considered in theoretical ALIP analysis.

Next, the standard configuration ALIP pressure-flowrate and efficiency performance was measured in sodium at 200 °C and 400 °C under applied voltages of 50  $V_{rms}$ , 75  $V_{rms}$ , 100  $V_{rms}$ , and 150  $V_{rms}$  and a frequency of 120 Hz. These measurements were compared to the analytical predictions evaluated under the

same conditions. This comparison showed that the finite length has a significant impact on the performance of an ALIP. However, it is important to recognize that the fundamental ALIP theory neglects aspects of real ALIPs such as finite dimensional and permeability ferromagnetic cores and finite width electric coils. Therefore, this suggested that the ALIP theory would provide little insight to the effects of coil grading and coil shifting. Nevertheless, the ALIP theory in this form predicts the experimental pump performance characteristics with some great degree of accuracy given its simplicity and demonstrates the significant impact the finite length has on ALIP performance.

Then the pressure-flowrate and efficiency performances of two coil shifting and two coil grading configurations were measured in sodium at 200 °C and under applied voltages of 50 V<sub>rms</sub>, 75 V<sub>rms</sub>, 100 V<sub>rms</sub>, and 150 V<sub>rms</sub> and a frequency of 120 Hz. These measurements were compared to the baseline performance measurements of the standard configuration pump evaluated under the same conditions. This comparison showed that all four configurations had either an insignificant impact on the total performance of the ALIP or marginally reduced the total efficiency. This observation is likely caused by the high operating frequency and synchronous velocity of the pump relative to the fluid velocity.

From the unsuccessful results of coil shifting and coil grading, several paths were identified for future work on the finite length effects of ALIPs. Firstly, it is clear that a detailed model must be constructed which accounts for effects like the finite dimensions of the stator core and coils as well as the finite ferromagnetic core permeability. This will allow for direct comparisons between the coil shifting and coil grading results to theory. Additionally, the model may provide improved performance predictions over the fundamental theory discussed in this work. Secondly, a larger capacity ALIP may be needed in order to measure a significant change in efficiency for the coil shifting and coil grading configurations. This could be validated with the improved ALIP model discussed earlier.

#### 5.2 SUMMARY OF PMIP CONCLUSIONS AND FUTURE WORK

In total, this work characterized several PMIP parameters. Firstly, the frictional losses in the PMIP channel were characterized in 200 °C and 400 °C sodium. These losses were found to be small relative to the total pump output pressure and a single curve was used for both temperatures. These data were used to convert the experimentally measured differential pressures to maximum developed pressure.

Secondly, dry-pump power was measured to estimate the resistive heating losses in the channel walls. Theoretical predictions were found to be in agreeance with the experimental results. However, recognize that the theory produces artificially lower estimates since it neglects the channel sidewalls, frictional losses, windage losses from the rotating magnet arrays, pullies, and belt, as well as other losses. These factors would tend to increase the analytically calculated losses.

Thirdly, the PMIP magnetic field was characterized across the channel width at three different heights. These results showed that the centerline magnetic field approximately follows a cosine across the channel width. Empirical shape factors were extracted from the experimental data. Moreover, at small channel heights the magnetic field was observed to vary little which supports the averaging assumption.

Next, the pressure-flowrate and efficiency performance of a 12-pole Double-Array Disc-Type PMIP was characterized in sodium at 200 °C and 400 °C under 30 Hz, 60 Hz, 75 Hz, and 90 Hz. Pump curves with respect to flowrate and slip were presented for the pressure and efficiency data. Moreover, it is important to note that few works have characterized the pressure-flowrate and efficiency performance of a disc-type PMIP configuration.

Then, these data were compared to analytic PMIP theory which accounts for the finite channel width and finite magnet width. Despite its simplicity, the analytic theory was found to reasonably predict the pressure-

flowrate and efficiency performance. In addition, the correction factor accounting for the finite channel and magnet width was validated. From these results, the theory suggests that the finite dimensions of the channel and magnets have a significant impact on the total performance of a PMIP.

While overall the results were successful, several paths have been identified for future work on the Finite Width Effect of PMIPs. Firstly, literature showed that the finite conductivity channel walls will have an important part in determining the PMIP current distributions. While an analytic solution may be difficult, a numerical Finite Element Analysis (FEA) model will provide additional insights to the Finite Width Effect. In total, this may produce even more accurate predictions of PMIP performance characteristics than the simple analytical calculations. Secondly, with consideration of the channel walls there is an opportunity to optimize the 12-Pole Double-Array Disc-Type PMIP with respect to efficiency.

# 5.3 SIGNIFICANCE AND CONCLUDING REMARKS

Liquid metals are seeing renewed interest as an efficient energy carrier in applications ranging from concentrated solar to nuclear fission. Under the nuclear sector there is significant interest in using elemental sodium metal as a reactor coolant. Over half a century ago, development of liquid sodium as a coolant began with the USS Seawolf and continues today with innovative reactor designs such at GE-Hitachi's PRISM and TerraPower's TWR.

With that being said, there is a need for improved thermal hydraulic components such as pumps. Typically, mechanical pumps like centrifugal pumps have filled this role for liquid metal systems. However, there are challenges in their application to chemically reactive fluids like sodium including material compatibility issues with seals and excessive wear with bearings. These challenges bring up concerns in the nuclear industry where safety is a driving factor.

As an alternative, liquid metals can be pumped using traveling magnetic fields with the Electromagnetic Induction Pump (EMIP). Compared to conventional mechanical pumps, EMIPs simplify design by avoiding direct contact of pump components with the metal and by eliminating high speed impellers, seals, and bearings. They also simplify plant design and safety by using unobstructed, low pressure drop, hermetically sealed flow conduits made of compatible materials. Therefore, EMIPs are a significant technological development for the nuclear industry.

However, typical EMIP efficiencies are low, ranging up to 45% in the case of the Annular Linear Induction Pump (ALIP). Some of these inefficiencies are due to the fundamental physics of EMIPs like Joule losses in the pump conduit and fluid. But other inefficiencies arise from finite dimensional edge effects like the Finite Length Effect in ALIPs and the Finite Width Effect in PMIPs. Before these pumps are deployed to large scale nuclear systems, the impact of edge effects on ALIP and PMIP must be understood to a greater degree.

While both of the finite dimensional effects have seen some work in literature, several knowledge gaps have been identified. Under the Finite Length Effect, only a single pair of papers have experimentally tested the method of coil grading to suppress the impact of the Finite Length Effect. Additionally, little work exists which investigates other methods of shaping the applied magnetic field its effect on pump performance. Under the Finite Width Effect, little experimental work has been done to validate a finite width coefficient accounting for the channel and magnet dimensions. Additionally, very few works characterized the pressure-flowrate and efficiency performance of new PMIP designs.

This work produced several results which are significant in both addressing the knowledge gaps and enhancing the developed EMIPs. Under ALIPs, this work characterized the pressure and efficiency performance of several pump configurations in 200 °C and 400 °C sodium. These baseline performance

parameters were compared to fundamental analytic theory which was found to have significant limitations. Moreover, the first-of-its-kind method of Coil Shifting was tested and compared to baseline performance measurements. Both the method of Coil Shifting and Coil Grading were found to have has marginal impact on the performance characteristics of a small ALIPs operating at high frequencies. Consequently, future works on the Finite Length Effect in small ALIPs at high frequency should focus on other methods of suppression such as the method of compensating currents. Furthermore, future works on the method of Coil Grading should focus on larger pumps which operate at lower frequencies.

Under PMIPs, this work characterized the pressure and efficiency performance of a 12-pole Double-Array Disc-Type PMIP in 200 °C and 400 °C sodium. These results are significant as the efficiency measurements represented a first-of-their-kind characterization for a Disc-Type PMIP. These baseline performance measurements were compared to fundamental theory which was shown to be in good agreeance. The comparison to theory showed that the Finite Width Effect has a significant impact on performance of a PMIP. Moreover, the finite magnet width correction factor  $K_{at,2}$  was validated and was shown to also severely impact PMIP performance. This result is significant in that most PMIP performance calculations neglect the finite magnet width.

In conclusion, EMIPs have numerous advantages over mechanical pumps for liquid metal systems which include simplicity and enhanced safety. Consequently, these pumps are a significant technological development for nuclear fission where cost reduction and safety are driving factors. However, a challenge with EMIPs are reduced pressure and efficiency performance cause by finite dimensional effects. This work has contributed to the depth of knowledge of EMIPs through first-of-their-kind performance measurements of a Coil Shifted ALIP and first-of-their-kind efficiency measurements of a 12-pole Double-Array Disc-Type PMIP. Moreover, a PMIP finite channel and magnet width correction factor was validated. Future works have been identified such a studying the impact of Coil Shifting and Coil Grading on a larger and

low frequency ALIP as well as the development of a PMIP model which accounts for the finite conductivity and dimensions of the channel sidewalls. In total, the author believes that this work has contributed toward the engineering knowledge of EMIPs with finite dimensional edge effects in their application to the nuclear industry.

#### 6. REFERENCES

- [1] M. El-Wakil, Nuclear Energy Conversion, Scranton: Intext Education Publishers, 1971.
- [2] J. Fink, "A consistent assessment of the thermophysical properties of sidum," *High Temperature Materials Science*, vol. 36, pp. 65-104, 1996.
- [3] G. Nellis and S. Klein, Heat Transfer, New York: Cambridge Univsersity Press, 2009.
- [4] R. Atz and R. Baker, "Pumps," in *Sodium-NaK Engineering Handbook*, vol. 4, O. Foust, Ed., New York, Gordon and Breach Science Publishers Inc., 1972.
- [5] D. Nixon, "Survey of Sodium Pump Technology," 1963.
- [6] J. Balkwill and J. Brindley, "Bearings and Seals," in *Sodium-NaK Engineering Handbook*, vol. 4, O. Foust, Ed., New York, Gordon and Breach Science Publishers Inc., 1972.
- [7] W. Li, L. Yu, J. Hao and M. Li, "Experimental and CFD Investigation on Flow Beahviors of a NPP Pump under Natural Circulation," *Science and Technology of Nuclear Installations*, 2019.
- [8] R. Ashley, R. Beeley, F. Fillmore, W. Hallet, B. Hayward, T. Gershun and J. Lundholm, "SRE Fuel Element Damage," Atomics International, 1959.
- [9] L. Blake, "Electromagnetic Pumps for Liquid Metals," *Journal of Nuclear Energy, Part B: Reactor Technology*, vol. 1, pp. 65-76, 1959.
- [10] R. E. Schwirian, "Analysis of Linear Induction or Traveling Wave Electromagnetic Pump of Annular Design," 1965.
- [11] J. Verkamp and R. Rhudy, "Electromagnetic Alkali Metal Pump Research Program," 1966.
- [12] E. P. Loewen, "Next-Generation Electromagnetic Pump Analysis Tools.," GE-Hitachi, 2015.
- [13] I. Bucenieks, "Perspectives of Using Rotating Permanent Magnets in the Design of Electromagnetic Induction Pumps," *Magnetohydrodynamics*, vol. 36, no. 2, pp. 181-187, 2000.
- [14] I. Bucenieks, "High Pressure and High Flowrate Induction Pumps with Permanent Magnets," *Magnetohydrodynamics*, vol. 39, no. 4, pp. 411-417, 2003.
- [15] I. Bucenieks, K. Kravalis and R. Krishbergs, "Pressure-Flow Rate Characteristics of the Pumps with Permanent Magnets," *Magnetohydrodynamics*, vol. 47, no. 1, pp. 97-104, 2011.
- [16] M. Hvasta, W. Nollet and M. Anderson, "Designing moving magnet pumps for high-temperature, liquid-metal systems," *Nuclear Engineering and Design*, no. 327, pp. 228-237, 2018.
- [17] E. Laithwaite and S. Nasar, "Linear-Motion Electrical Machines," *Proceedings of the IEEE*, vol. 58, no. 4, pp. 531-540, 1970.
- [18] J. Valdmanis, "On theory of longitudinal finite length effect in linear induction magnetohydrodynamic machine," *Magnetohydrodynamics*, pp. 101-106, 1966.
- [19] I. Kirillov, "Longitudinal End Effect in Cylindrical Induction MHD Machines," *Magnetohydrodynamics*, no. 2, pp. 109-116, 1972.
- [20] H. Araseki, I. R. Kirillov, G. V. Preslitsky and A. P. Ogorodnikov, "Double-supply-frequency pressure pulsation in annular linear induction pump Part I: Measurement and numerical analysis," *Nuclear Engineering and Design*, vol. 195, pp. 85-100, 2000.
- [21] J. Gieras, G. Dawson and A. Eastham, "A New Longitudinal End Effect Factor For Linear Induction Motors," *IEEE Transactions on Energy Conversion*, Vols. EC-2, no. 1, pp. 152-169, 1987.

- [22] H. Araseki, I. R. Kirillov, G. V. Preslitsky and A. P. Ogorodnikov, "Double-supply-frequency pressure pulsation in annular linear induction pump Part II: Reduction of pulsation by linear winding grading at both stator ends," *Nuclear Engineering and Design*, vol. 200, pp. 397-406, 2000.
- [23] M. Drits, "End Effect in MHD-Type Linear Induction Machine with Finite-Length Induction: Mathemathical Model," *Magnetohydrodynamics*, vol. 4, pp. 19-95, 1983.
- [24] L. Lazarenko, "Analysis of Longitudinal Fringe Effects in Linear Induction MHD Machines," *Magnetohydrodynamics*, no. 1, pp. 91-98, 1971.
- [25] L. Vasil'yev and A. Kozhainov, "Magnetohydrodynamics in marines engineering," 1967.
- [26] H. Bolton, "Transverse edge effect in sheet-rotor induction motors," *Proceedings of IEEE*, vol. 116, no. 5, pp. 725-731, 1969.
- [27] E. Pierson, R. Hanitsch, T. Huehns and H. Mosebach, "Predicted and Measured Finite-Width Effects in Linear Induction Machines," *IEE Transactions on Power Apparatus and Systems,* Vols. PAS-96, no. 4, pp. 1081-1086, 1977.
- [28] M. G. Hvasta, W. K. Nollet and M. H. Anderson, "Designing moving magnet pumps for high-temperature, liquid-metal systems," *Nuclear Engineering and Design*, vol. 327, pp. 228-237, 2018.
- [29] B. R. Munson, T. H. Okiishi, W. W. Huebsch and A. P. Rothmayer, Fundamentals of Fluid Mechanics, Seventh ed., Wiley, 2013.
- [30] E. S. Pierson and W. D. Jackson, "The MHD Induction Machine," 1966.
- [31] C. Borghi, A. Cristofolini and W. Fabbri, "Study of the Design Model of a Liquid Metal Induction Pump," *IEEE Transactions on Magnetics*, vol. 34, no. 5, pp. 2956-2959, 1998.
- [32] L. Goldsteins, "Experimental and numerical analysis of behavior of electromagnetic annular linear induction pump," 2015.
- [33] H. R. Kim, "The theoretical approach for viscous and end effects on an MHD pump for sodium circulation," *Annals of Nuclear Energy*, vol. 62, pp. 103-108, 2013.
- [34] H. Ota, K. Katsuki, M. Funato, J. Taguchi, A. W. Fanning, Y. Doi, N. Nibe, M. Ueta and T. Inagaki, "Development of 160 m3/min Large Capacity Sodium-Immersed Self-Cooled Electromagnetic Pump," *Journal of Nuclear Science and Technology*, vol. 41, no. 4, pp. 511-523, 2004.
- [35] C. Roman, "Studies of the Annular Linear Induction Pumps for Sodium Circuits Use in Nuclear Plants," *IEEE*, pp. 1-10, 2013.
- [36] E. S. Pierson and W. D. Jackson, "The MHD Induction Machine," Cambridge, 1966.
- [37] S. Nasar, Handbook of Electric Machines, McGraw-Hill, 1987.
- [38] I. Kirillov and D. Obukhov, "Completely Two-Dimensional Model for Examining the Characteristics of a Linear Cylindrical Induction Pum," *Technical Physics*, vol. 5, pp. 999-1005, 2005.
- [39] L. R. Blake, "Conduction and Induction Pumps for Liquid Metals," in *British Nuclear Energy Conference*, 1957.
- [40] S. Nasar, Handbook of Electric Machines, McGraw-Hill, 1987.
- [41] I. Bucenieks, "Perspectives of Increasing Efficiency and Productivity of Electromagnetic Induction Pumps for Mercury Basing on Permanent Magnets," in *International Conference on Nuclear Engineering*, 2006.

- [42] I. Lavrentyev, S. Sidorenko and A. Shisko, "Effect of the conductivity of the walls on the characteristics of an MHD channel with finite Rm.," *Magnetohydrodynamics*, vol. 19, no. 4, pp. 456-464, 1983.
- [43] I. Bucenieks and K. Kravalis, "Efficiency of EM Induction Pumps with Permanent Magnets," *Magnetohydrodynamics*, vol. 47, no. 1, pp. 89-96, 2011.
- [44] J. Hunt, "Magnetohydrodynamic flow in rectangular ducts," *Journal of Fluid Mechanics*, vol. 4, no. 21, pp. 577-590, 1965.
- [45] S. Tado and S.-i. Kamiyama, "Analysis of Transverse Edge Effect of Linear Induction Pump with Electrically Conducting Side Walls," *Nuclear Science and Technology*, vol. 20, no. 5, pp. 379-388, 1983.
- [46] I. E. Bucenieks, "Perspectives of Using Rotating Permanent Magnets in the Design of Electromagnetic Induction Pumps," *Magnetohydrodynamics*, vol. 36, no. 2, pp. 151-156, 2000.
- [47] R. Campana, E. Diehl and R. Faught, "Components," in *Liquid Metal Handbook*, H. Grantz, Ed., The Atomic Energy Commission, 1955.
- [48] H. Elrod and R. Fouse, "An investigation of electromagnet flowmeters," *Transactions of the American Society of Mechanical Engineers*, vol. 74, 1952.
- [49] W. Gray, "Magnetic Flowmeter Calibration Results (KAPL-613)," 1951.
- [50] J. Shercliff, The Theory of Electromagnetic Flow-Measurement, Cambridge University Press, 1962.
- [51] W. C. Gray and E. Astley, "Liquid metal magnetic flowmeters," *Journal of the Instrument Society of America*, vol. 1, pp. 15-23, 1954.
- [52] J. Mausteller, F. Tepper and S. Rodgers, Alkali Metal Handling and Systems Operating Techniques, Gordon and Breach, 1968.
- [53] U. A. E. Commission, "Permanent Magnet Flowmeter for Liquid Metal Piping Systems (Technical Report RDT C 4-5T)," 1971.
- [54] L. G. Vasil'yev and A. I. Kozhainov, "Magnetohydrodynamics in Marine Engineering," 1967.
- [55] S. Kim and C. Doose, "Temperature compensation of NdFeB permanent magnets," 1998.
- [56] P. Kirillov, V. Kolesnikov, V. Kuznetsov and N. Turchin, "Insturments for Measuring the Pressure, Flow, and Level of Fuzed Alkali Metals," *Atomic Energy (USSR)*, vol. 9, no. 3, pp. 173-181, 1960.
- [57] JCGM100:2009, Evaluation of measurement data Guide to the expression of uncertainty in measurement, 1 ed., 2010.
- [58] A. E. Knowlton, Electric Power Metering, McGraw-Hill, 1934.
- [59] I. Lavrent'ev and A. Shishko, "Electrodynamic Processes in MHD Channels with High Magnetic Reynolds Number," *Magnetohydrodynamics*, vol. 3, pp. 81-106, 1980.
- [60] O. Danielsson and M. Leigon, "Flux Distribution in Linear Permanent-Magnet Synchronous machines Including Longitudinal End Effects," *IEEE Transactions on Magnetics*, vol. 43, no. 7, pp. 3197-3201, 2007.
- [61] J. Balkwill and J. Brindley, "Bearings and Seals," in *Sodium-NaK Engineering Handbook*, vol. 4, O. Foust, Ed., New York, New York: Gordon and Breach Science Publishers Inc., 1972.